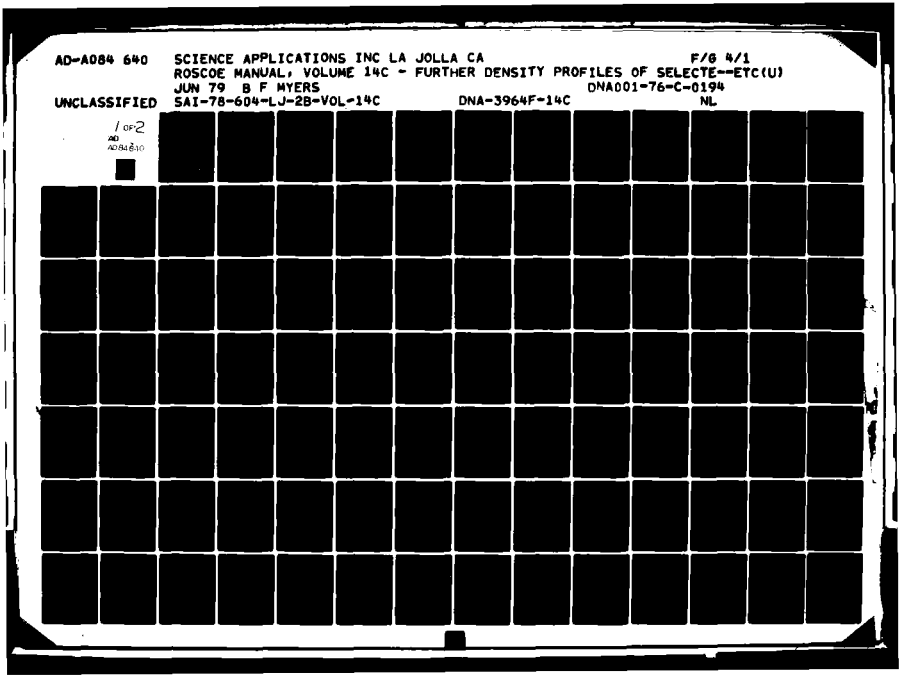
AD-A084 640
SCIENCE APPLICATIONS INC LA JOLLA CA
F/G 4/1
ROSCOE MANUAL, VOLUME 14C - FURTHER DENSITY PROFILES OF SELECTE--ETC(U)
JUN 79 B F MYERS
DNA001-76-C-0194
UNCLASSIFIED
SAI-78-604-LJ-2B-VOL-14C
DNA-3964F-14C
NL
1 OF 2
AD
AD84640

DNA 3964F-14C

THE ROSCOE MANUAL

Volume 14C-Further Density Profiles of Selected Atmospheric Species

Science Applications, Inc.
P.O. Box 2351
La Jolla, California 92038

30 June 1979

Final Report for Period 1 January 1976—30 June 1979

CONTRACT No. DNA 001-76-C-0194

APPROVED FOR PUBLIC RELEASE;
DISTRIBUTION UNLIMITED.

THIS WORK SPONSORED BY THE DEFENSE NUCLEAR AGENCY UNDER RDT&E RMSS CODES B322076464 S99QAXHC06237 H2590D, B32207T464 S99QAXHC06237 H2590D, B322077464 S99QAXHI00426 H2590D, B322078464 S99QAXHI00426 H2590D, AND B322079464 S99QAXHI00426 H2590D.

Prepared for
Director
DEFENSE NUCLEAR AGENCY
Washington, D. C. 20305

Destroy this report when it is no longer needed. *Do not return to sender.*

PLEASE NOTIFY THE DEFENSE NUCLEAR AGENCY, ATTN: STTI, WASHINGTON, D.C. 20305, IF YOUR ADDRESS IS INCORRECT, IF YOU WISH TO BE DELETED FROM THE DISTRIBUTION LIST, OR IF THE ADDRESSEE IS NO LONGER EMPLOYED BY YOUR ORGANIZATION.

UNCLASSIFIED

SECURITY CLASSIFICATION OF THIS PAGE *(When Data Entered)*

REPORT DOCUMENTATION PAGE	READ INSTRUCTIONS BEFORE COMPLETING FORM
1. REPORT NUMBER: DNA 3964F-14C ✓	2. GOVT ACCESSION NO.: AD-A084640
3. RECIPIENT'S CATALOG NUMBER	
4. TITLE *(and Subtitle)*: THE ROSCOE MANUAL Volume 14C—Further Density Profiles of Selected Atmospheric Species	5. TYPE OF REPORT & PERIOD COVERED: Final Report for Period 1 Jan 76—30 Jun 79
	6. PERFORMING ORG. REPORT NUMBER: SAI-78-604-LJ-2b ✓
7. AUTHOR(s): Benjamin F. Myers	8. CONTRACT OR GRANT NUMBER(s): DNA 001-76-C-0194 ✓
9. PERFORMING ORGANIZATION NAME AND ADDRESS: Science Applications, Inc. ✓ P.O. Box 2351 La Jolla, California 92038	10. PROGRAM ELEMENT, PROJECT, TASK AREA & WORK UNIT NUMBERS: Subtask S99QAXHC062-37 Subtask S99QAXHI004-26
11. CONTROLLING OFFICE NAME AND ADDRESS: Director Defense Nuclear Agency Washington, D.C. 20305	12. REPORT DATE: 30 June 1979
	13. NUMBER OF PAGES: 120
14. MONITORING AGENCY NAME & ADDRESS *(if different from Controlling Office)*	15. SECURITY CLASS *(of this report)*: UNCLASSIFIED
	15a. DECLASSIFICATION/DOWNGRADING SCHEDULE

16. DISTRIBUTION STATEMENT *(of this Report)*

Approved for public release; distribution unlimited.

17. DISTRIBUTION STATEMENT *(of the abstract entered in Block 20, if different from Report)*

18. SUPPLEMENTARY NOTES

This work sponsored by the Defense Nuclear Agency under RDT&E RMSS Codes B322076464 S99QAXHC06237 H2590D, B322077464 S99QAXHC06237 H2590D, B322078464 S99QAXHI00426 H2590D, B322079464 S99QAXHI00426 H2590D, and B322079464 S99QAXHI00426 H2590D.

19. KEY WORDS *(Continue on reverse side if necessary and identify by block number)*

Atmospheric Species: H_2O, O_3, CH_4, CO, OH, HO_2, H, N_2O, NO, N, $N(^2D)$, $O(^1D)$.

Atmospheric Models and Profiles

20. ABSTRACT *(Continue on reverse side if necessary and identify by block number)*

Profiles and models of ambient atmospheric species are presented for water, ozone, methane, carbon monoxide, hydroxyl and hydroperoxyl radicals, hydrogen atoms, nitrous and nitric oxides, nitrogen atoms (N and $N(^2D)$), and excited atomic oxygen ($O(^1D)$). This report greatly extends and partly revises Volume 14b which pertained only to midlatitude density profiles of H_2O, O_3, CO_2, NO_2, NO, N, O, and $O_2(a^1\Delta_g)$.

DD FORM 1 JAN 73 1473 EDITION OF 1 NOV 65 IS OBSOLETE

UNCLASSIFIED

SECURITY CLASSIFICATION OF THIS PAGE *(When Data Entered)*

Conversion factors for U.S. customary to metric (SI) units of measurement.

To Convert From	To	Multiply By
angstrom	meters (m)	1.000 000 X E -10
atmosphere (normal)	kilo pascal (kPa)	1.013 25 X E +2
bar	kilo pascal (kPa)	1.000 000 X E +2
barn	meter^2 (m^2)	1.000 000 X E -28
British thermal unit (thermochemical)	joule (J)	1.054 350 X E +3
calorie (thermochemical)	joule (J)	4.184 000
cal (thermochemical)/cm^2	mega joule/m^2 (MJ/m^2)	4.184 000 X E -2
curie	*giga becquerel (GBq)	3.700 000 X E +1
degree (angle)	radian (rad)	1.745 329 X E -2
degree Fahrenheit	degree kelvin (K)	$t_K = (t°f + 459.67)/1.8$
electron volt	joule (J)	1.602 19 X E -19
erg	joule (J)	1.000 000 X E -7
erg/second	watt (W)	1.000 000 X E -7
foot	meter (m)	3.048 000 X E -1
foot-pound-force	joule (J)	1.355 818
gallon (U.S. liquid)	meter^3 (m^3)	3.785 412 X E -3
inch	meter (m)	2.540 000 X E -2
jerk	joule (J)	1.000 000 X E +9
joule/kilogram (J/kg) (radiation dose absorbed)	Gray (Gy)	1.000 000
kilotons	terajoules	4.183
kip (1000 lbf)	newton (N)	4.448 222 X E +3
kip/inch^2 (ksi)	kilo pascal (kPa)	6.894 757 X E +3
ktap	newton-second/m^2 (N-s/m^2)	1.000 000 X E +2
micron	meter (m)	1 000 000 X E -6
mil	meter (m)	2.540 000 X E -5
mile (international)	meter (m)	1.609 344 X E +3
ounce	kilogram (kg)	2.834 952 X E -2
pound-force (lbs avoirdupois)	newton (N)	4.448 222
pound-force inch	newton-meter (N·m)	1.129 848 X E -1
pound-force/inch	newton/meter (N/m)	1.751 268 X E +2
pound-force/foot^2	kilo pascal (kPa)	4.788 026 X E -2
pound-force/inch^2 (psi)	kilo pascal (kPa)	6.894 757
pound-mass (lbm avoirdupois)	kilogram (kg)	4.535 924 X E -1
pound-mass-foot^2 (moment of inertia)	kilogram-meter^2 (kg·m^2)	4.214 011 X E -2
pound-mass/foot^3	kilogram/meter^3 (kg/m^3)	1.601 846 X E +1
rad (radiation dose absorbed)	**Gray (Gy)	1.000 000 X E -2
roentgen	coulomb/kilogram (C/kg)	2.579 760 X E -4
shake	second (s)	1.000 000 X E -8
slug	kilogram (kg)	1.459 390 X E +1
torr (mm Hg, 0° C)	kilo pascal (kPa)	1.333 22 X E -1

*The becquerel (Bq) is the SI unit of radioactivity; 1 Bq = 1 event/s.
**The Gray (Gy) is the SI unit of absorbed radiation.

A more complete listing of conversions may be found in "Metric Practice Guide E 380-74," American Society for Testing and Materials.

TABLE OF CONTENTS

TABLE OF CONTENTS (Continued)

LIST OF ILLUSTRATIONS

LIST OF ILLUSTRATIONS (Continued)

LIST OF TABLES

LIST OF TABLES (Continued)

SECTION 1

INTRODUCTION

This report is a major extension and a partial revision of Volume 14b [My-75] which pertained only to the midlatitude density profiles of selected atmospheric species. The current report removes (where feasible) the midlatitude restriction and includes density profiles for additional species relevant directly or indirectly to ROSCOE-IR. Table 1-1 provides a guide to the species for which density profiles are provided in Volumes 14b and 14c.

In the current volume, profiles for selected atmospheric species have been constructed on the basis of observed and calculated ambient densities from ground level to several hundred kilometers altitude. The goal in developing these profiles was to provide values of the densities sufficiently accurate for use in infrared transmission calculations as well as for chemical calculations requiring ambient densities.

For some of the species (especially water and ozone and, to a lesser extent, nitric oxide and nitrogen atoms) the profiles are quite complex and may have dependencies on (in addition to altitude) geographic position, latitude, local apparent time, fraction of season-year, and solar decimetric flux. These more complex profiles are sometimes referred to as models.

The models and profiles are derived independently for the various species and thus consistency cannot be assured. This problem is quite complex and is definitely outside the scope of this report.

The units of measure employed in the models and profiles described below reflect the units generally found in the literature for individual species. No attempt has been made to use a consistent set of units throughout this report. Conversion to consistent units is performed in the computer-coded version of these profiles and is documented in Volume 14a-1 [HS-78].

Table 1-1. Guide to species profiles in Volumes 14b and 14c.[a]

Species	Profile in Indicated Section of Vol. 14b	Vol. 14c	Comment
O	2		Generalization of overall atmospheric model below 120-km altitude has led to a slightly revised O profile.
$O(^1D)$		9	
$O_2(a^1\Delta_g)$	3		
O_3	4	3	Latitudinal and seasonal dependence now included for $z < 55$ km. For $z > 55$ km, diurnal dependence from Vol. 14b obtains.
N	6	12	Revised and extended.
$N(^2D)$		13	
NO	5	11	Revised and extended.
NO_2	7		
N_2O		10	
CO_2	8		
CO		5	
CH_4		4	
H_2O	9	2	Geographical and seasonal dependence now included for $z < 5$ km; other revisions for $z < 70$ km. For $z > 70$ km, data from Vol. 14b obtains.
OH		6	
HO_2		7	
H		8	

[a] For He and $N(^2P)$ see Sections 2 and 4, respectively, of Volume 14a-1.

SECTION 2

A MODEL FOR WATER PROFILES

2-1 INTRODUCTION

For ROSCOE-IR a more accurate and therefore detailed model of the atmospheric H_2O content is required than is present in ROSCOE-Radar [My-75, HS-75]. Greater accuracy is required for IR transmission calculations and models involving water vapor condensation phenomena. Thus, a careful modeling of the H_2O content at altitudes below 50 km is required. Also, the calculations of the H_2O chemistry at these altitudes benefit from the improved model. Thus, it becomes necessary to account for the geographical and seasonal variations in H_2O content at altitudes below about 30 km. These variations can be large; in the model presented below, they amount to factors as large as 30 and 10, respectively.

The model presented here yields H_2O profiles as a function of altitude and of time of year for each of variously selected geographical areas near the earth's surface treated as quasi-homogeneous moisture regions. The influence of the tropical troposphere on the lower stratosphere is modeled. The data base for the model consists of (a) NASA data [Jo-75c, SG-71, SF-72b] for altitudes up to 5 km, (b) data from the review by Harries [Ha-76e] for altitudes between 14 and 45 km, and (c) data from the review by Myers [My-75] for altitudes above 70 km. Data for altitudes between 5 and 14 km and between 45 and 70 km were obtained by interpolation using the data base and features of the model.

2-2 GENERAL DESCRIPTION OF THE MODEL

The model is formulated in terms of modules which are characterized (a) near the earth's surface by ranges of latitude and longitude and quasi-homogeneous moisture regions within the ranges and (b) at higher altitudes by spherical shells representing transition altitudes of the model. The latitude ranges (in degrees) are 0 to 30,

30^+ to 60, and 60^+ to 90; the quasi-homogeneous moisture regions are described as dry, intermediate, or wet. The moisture regions apply to the corresponding ranges of latitude in both the northern and southern hemispheres according to the prescription developed below when the appropriate seasonal dependence is taken into account. The spherical shells extend from the earth's surface to 5 km, 5^+ to 14 km, and above 14 km. Use of the shells permits a description of the H_2O altitude profiles based on the available data and model profiles.

The NASA data [Jo-75c] represent the results of measurements only up to 5 km; between 5 and 25 km, extrapolations of the data are made [SG-71, SF-72b] which, however, are not used in the present model. The NASA data provide a seasonal variation in the H_2O densities. In addition, the NASA data are subdivided [SF-72b] into 45 homogeneous moisture regions to account for geographical variations. In the present model, this number of regions is reduced to six (quasi-homogeneous regions) by averaging over subsets of similar moisture regions. The errors introduced by the averaging are generally less than 50 percent (see Section 2-3). The NASA data are available only in tabulated form [Jo-75c], but with the treatment of the data in the present model, all the data of the six moisture regions have been represented surprisingly accurately by a simple transcendental function. This formulation accounts for the altitude, seasonal, and geographical dependence of the selected H_2O density data with an average error of less than six percent.

Between 5 and 14 km, there are insufficient data and in the model the necessary data are generated by logarithmic interpolation of the values of the mass-mixing ratios at 5 and 14 km.

Between 14 and 45 km, the mean altitude profile of the H_2O mass-mixing ratio is based on a smoothed-curve representation of the mean, midlatitude vertical distribution derived by Harries [Ha-76e] and on a latitude dependence which is constant between about 30 and 90 degrees latitude but rises in the 0-to about 30-degree latitude band to account for the influence of the high tropopause in the tropical latitudes.

The seasonal dependence in the model extends from ground level to 20 km; the amplitude of the dependence declines montonically to a negligible value at 20 km. The modeling of the seasonal dependence is in accord with the NASA data [Jo-75c] between 0 and 5 km and

in accord with the data of Mastenbrook [Ma-71c] between 14 and 20 km. An altitude-dependent phase shift in the seasonal variation of the water vapor mixing ratio is incorporated in the model; this phase shift becomes significant at altitudes above approximately 14 km. The phase shift is assumed to be linearly dependent on latitude (in the absence of relevant data). For the lower stratosphere, the seasonal dependence and its phase shift may be viewed [Ha-76e] as the result of control of water admission to the lower stratosphere by the tropical tropopause [also see Ne-77].

Between 45 and 70 km, the mixing ratio data are generated by interpolation based on the altitude profiles ending at 45 km and beginning at 70 km.

Above 70 km, the mixing ratios are taken from a review by Myers [My-75]; these ratios are based on calculations according to various models [Hu-73a, TB-72, GZ-72a, HS-74a] between 70 and 120 km and on an assumed exponential decrease at altitudes above 120 km.

2-3 WATER DENSITIES UP TO 5 KM

The water densities up to 5 km for six moisture regions were derived from NASA data [Jo-75c] and are presented in Tables 2-1, 2-2, and 2-3. The moisture regions are characterized as wet, dry, or intermediate. The latitude and longitude bounds for the moisture regions are depicted in Figure 2-1. In Table 2-4, the identification numbers of the 45 homogeneous moisture regions used in obtaining the data of Tables 2-1, 2-2, and 2-3 are listed together with the average maximum errors resulting from the averaging procedure.

The data of Tables 2-1, 2-2, and 2-3 were fit with the following function:

$$\begin{aligned} \ell n[H_2O] &= A(\alpha,z)\sin(360f - 120) + B(\alpha) \\ &\quad - (0.4845 + 2.33 \times 10^{-4} L)z \\ &\quad - (0.117 + 5.91 \times 10^{-3} L)e^{-z} \delta_{\alpha,\alpha_{dry}} \end{aligned} \tag{1}$$

Table 2-1a. Water mass-density (g/m^3) profile data (monthly mean) for 0° to 30° north latitude range.

	Wet Region (α = 1)						Dry Region (α = 2)					
Month	z = 0	1	2	3	4	5	z = 0	1	2	3	4	5
1	14.8	9.3	5.4	3.1	1.7	1.2	6.8	5.3	3.0	1.9	1.1	0.69
2	14.7	9.1	5.5	3.2	2.0	1.2	6.9	5.3	3.0	1.9	1.1	0.67
3	15.3	9.5	5.8	3.4	2.1	1.3	7.6	5.6	3.3	2.1	1.3	0.80
4	16.3	10.3	6.5	3.9	2.5	1.5	8.7	6.5	4.0	2.5	1.6	0.98
5	17.9	11.2	7.3	4.5	2.8	1.8	9.8	7.3	4.6	2.8	1.8	1.1
6	18.9	12.3	7.9	4.9	3.2	2.1	12.3	9.1	5.7	3.5	2.3	1.5
7	19.5	12.9	8.3	5.2	3.4	2.2	13.7	10.0	6.5	4.1	2.8	1.9
8	19.8	13.2	8.5	5.3	3.5	2.3	13.7	10.2	6.7	4.4	2.9	1.9
9	19.6	13.0	8.3	4.6	3.4	2.2	13.1	9.7	6.1	3.9	2.5	1.6
10	18.3	11.9	7.6	4.7	3.0	1.9	10.9	8.1	5.0	3.1	1.9	1.2
11	16.9	10.7	6.5	3.8	2.4	1.6	9.6	7.2	4.3	2.7	1.6	1.0
12	15.8	10.0	6.0	3.6	2.3	1.4	9.1	6.8	4.1	2.5	1.5	0.90

Table 2-1b. Geographic regions for 0° to 30° latitude range.[a]

Region	Latitude Bounds	Longitude Bounds
Northern tropical, wet	$0 \leq L < 10$ N	Unrestricted
Northern tropical, wet	$10\ N \leq L \leq 30$ N	$50\ E < \phi < 350E$
Northern tropical, dry	$10\ N \leq L \leq 30$ N	$350\ E \leq \phi \leq 50$ E
Southern tropical, wet	$0 \leq L < 15$ S	Unrestricted
Southern tropical, wet	$15\ S \leq L \leq 30$ S	$150\ E < \phi < 120$ E
Southern tropical, dry	$15\ S \leq L \leq 30$ S	$120\ E \leq \phi \leq 150$ E

[a] L = latitude and ϕ = east longitude, in degrees.

Table 2-2a. Water mass-density (g/m^3) profile data (monthly mean) for 30° to 60° north latitude range.

	Wet Region (α = 3)						Intermediate Region (α = 4)					
Month	z = 0	1	2	3	4	5	z = 0	1	2	3	4	5
1	8.86	6.16	3.17	1.85	1.14	0.71	5.07	3.23	1.88	1.06	0.64	0.37
2	8.76	6.08	3.14	1.80	1.11	0.69	4.99	3.18	1.90	1.09	0.64	0.36
3	8.91	6.34	3.23	1.84	1.14	0.73	5.44	3.46	2.10	1.20	0.72	0.42
4	10.14	7.09	3.82	2.20	1.37	0.88	6.32	4.10	2.54	1.49	0.90	0.53
5	12.00	8.33	4.63	2.70	1.68	1.08	7.66	5.09	3.22	1.93	1.17	0.69
6	13.93	9.86	5.67	3.29	2.11	1.38	9.27	6.39	4.10	2.52	1.54	0.92
7	15.73	10.28	6.39	3.84	2.90	1.51	10.96	7.53	4.87	3.09	1.90	1.15
8	16.04	10.46	6.50	3.89	2.44	1.51	11.22	7.56	4.82	2.94	1.85	1.13
9	14.66	9.68	5.85	3.46	2.18	1.37	9.72	6.42	4.09	2.45	1.52	0.92
10	12.36	7.88	4.75	2.76	1.73	1.08	8.07	5.06	3.11	1.77	1.09	0.65
11	10.21	6.48	3.87	2.25	1.40	0.86	6.35	4.06	2.49	1.44	1.18	0.50
12	8.69	5.56	3.36	1.98	1.22	0.74	5.44	3.46	2.10	1.21	0.72	0.41

	Dry Region (α = 5)					
Month	z = 0	1	2	3	4	5
1	1.44	1.30	0.96	0.72	.44	0.26
2	1.58	1.38	1.03	0.74	0.45	0.26
3	2.24	1.77	1.27	0.83	0.50	0.29
4	3.85	2.83	1.90	1.18	0.71	0.41
5	5.76	4.35	2.92	1.86	1.12	0.65
6	8.45	6.55	4.35	2.77	1.68	0.97
7	10.72	8.20	5.49	3.47	2.13	1.27
8	10.29	7.73	5.08	3.18	1.95	1.15
9	7.76	5.58	3.71	2.34	1.44	0.86
10	5.29	3.71	2.50	1.58	0.98	0.59
11	3.17	2.35	1.61	1.08	0.66	0.39
12	1.77	1.55	1.12	0.82	0.50	0.29

Table 2-2b. Geographic regions for 30° to 60° latitude range.

Region	Latitude Bounds	Longitude Bounds
Northern temperate, dry	50 N < L ≤ 60 N	30 E < ϕ ≤ 110 E, 247 E ≤ ϕ ≤ 255 E
Northern temperate, dry	40 N < L ≤ 60 N	110 E ≤ ϕ ≤ 135 E
Northern temperate, dry	45 N < L ≤ 60 N	255 E ≤ ϕ ≤ 303 E
Northern temperate, inter.	45 N < L ≤ 50 N	247 E ≤ ϕ ≤ 255 E
Northern temperate, inter.	40 N < L ≤ 45 N	255 E ≤ ϕ ≤ 303 E
Northern temperate, inter.	40 N < L ≤ 60 N	303 E < ϕ ≤ 30 E, 135 E < ϕ ≤ 230 E
Northern temperate, inter.	40 N < L ≤ 50 N	30 E < ϕ < 110 E, 230 E < ϕ ≤ 235 E
Northern temperate, inter.	35 N < L ≤ 50 N	235 E < ϕ ≤ 240 E
Northern temperate, wet	30 N < L ≤ 40 N	255 E < ϕ ≤ 235 E
Northern temperate, wet	30 N < L ≤ 35 N	235 E < ϕ ≤ 240 E
Northern temperate, wet	50 N < L ≤ 60 N	230 E < ϕ ≤ 240 E
Northern temperate, wet	30 N < L ≤ 60 N	240 E < ϕ < 247 E
Northern temperate, wet	30 N < L ≤ 45 N	247 E ≤ ϕ < 255 E
Southern temperate, inter.	35 S < L ≤ 60 S	Unrestricted
Southern temperate, wet	30 S < L ≤ 35 S	Unrestricted

Table 2-3a. Water mass-density (g/m^3) profile data (monthly mean) for 60° to 90° north latitude range.

	Dry Region (α = 6)					
Month	z = 0	1	2	3	4	5
1	0.77	0.71	0.51	0.42	0.25	0.16
2	0.73	0.70	0.51	0.42	0.25	0.16
3	0.89	0.86	0.60	0.44	0.26	0.15
4	1.52	1.32	0.92	0.61	0.36	0.21
5	3.01	2.32	1.60	1.01	0.59	0.33
6	5.00	3.97	2.71	1.70	1.00	0.57
7	6.40	5.30	3.59	2.29	1.38	0.81
8	6.21	4.98	3.28	2.06	1.23	0.72
9	4.50	3.39	2.22	1.36	0.80	0.46
10	2.66	1.96	1.31	0.83	0.48	0.27
11	1.43	1.12	0.77	0.56	0.33	0.19
12	0.91	0.81	0.56	0.45	0.27	0.15

Table 2-3b. Geographic regions for 60° to 90° latitude range.

Region	Latitude Bounds	Longitude Bounds
Arctic	60 N < L $\leq$ 90 N	Unrestricted
Antarctic	60 S < L $\leq$ 90 S	Unrestricted

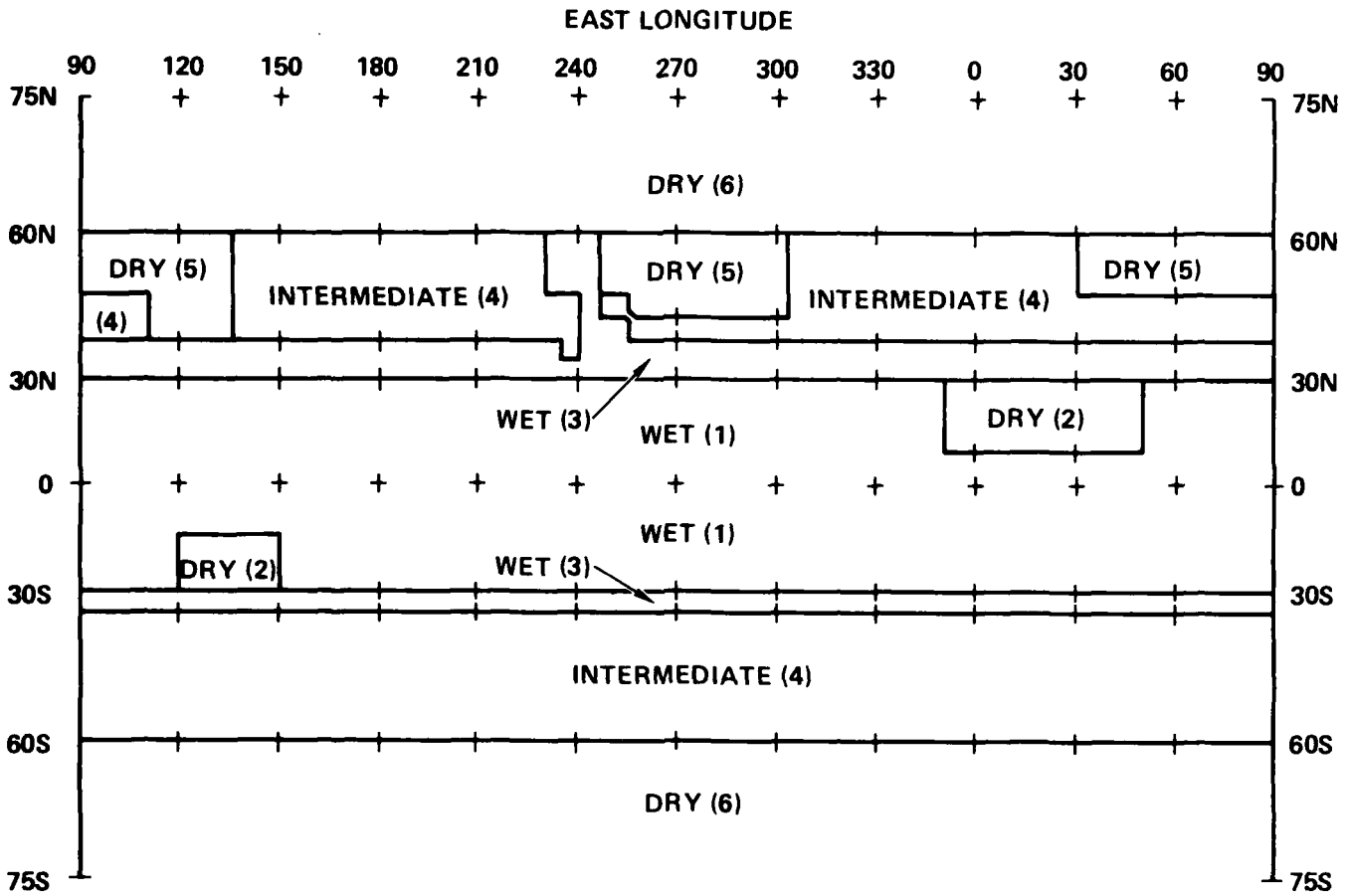

Figure 2-1. Geographic locations of 0- to 5-km altitude moisture regions in water profile model.

Table 2-4. Data on reduction of number of moisture regions.

Our Model Moisture Regions			NASA Moisture Regions[a]	Average Max. Error
α Number	Latitude Range	Moisture Region		
1	0°-30°	Wet	16-22, 35, 36	30%
2	0°-30°	Dry	23, 26, 27, 30-33, 42, 45	40%
3	30°-60°	Wet	10-15, 27	30%
4	30°-60°	Inter.	6-9	30%
5	30°-60°	Dry	4, 5	15%
6	60°-90°	Dry	2	-

[a] The NASA moisture regions are numbered according to SF-72b.

where $[H_2O]$ is the water mass density (g/m^3); $A(\alpha,z)$, the amplitude, which is dependent on the moisture region (α) and the altitude z(km), is given by

$$A(\alpha,z) = a_1(\alpha) + a_2(\alpha)z + a_3(\alpha)z^2 \quad ; \tag{2}$$

f is the fraction of the year, being 0 on January 1 and 1.0 on December 31 (in northern hemisphere); $B(\alpha)$ is a coefficient for the mean value of $\ell n[H_2O]$; L is the latitude in degrees; $\delta_{\alpha,\alpha_{dry}} = 1$ when $\alpha = \alpha_{dry}$ (where $\alpha_{dry} = 2$, 5, or 6 for the dry regions) and zero otherwise.* The values of the coefficients a_1, a_2, a_3, and $B(\alpha)$ are listed in Table 2-5. With the data of Table 2-5 and Equation (1), the data in Tables 2-1, 2-2, and 2-3 can be represented with an average error of less than 6 percent and a maximum error of less than 26 percent.

2-4 WATER DENSITIES BETWEEN 5 AND 14 KM

Water density data between 5 and 14 km are determined by interpolation based on the mass-mixing ratios (m_R, expressed in parts per million by mass, ppmm) at 5 and 14 km according to the equation:

$$\ell n[m_R(z,\alpha,f,L)] = \frac{14 - z}{9} \ell n\left[\frac{m_R(5,\alpha,f,L)}{m_R(14,f,L)}\right] + \ell n[m_R(14,f,L)], \quad 5 < z(km) < 14. \tag{3a}$$

Here, $m_R(z,\alpha,f,L)$ is the mass-mixing ratio at altitude z and latitude L in moisture region α at fractional time of year f. The mass-mixing ratio and water mass density are related by the equation

$$m_R(z,\alpha,f,L) = [H_2O(z,\alpha,f,L)]/\rho(z), \text{ ppmm} \tag{3b}$$

---

*In the formulative stage of Equation (1), the coefficients of z and e^{-z} were found to be smooth functions of the mean latitude for each range. This dependence was generalized to that of Equation (1); thus the homogeneous moisture regions became quasi-homogeneous moisture regions.

Table 2-5. Parameters for fit of water data between 0 and 5 km (per Equations (1) and (2)).

Our Model Moisture Regions			Coefficients for A(α,z)			
α Number	Latitude Range	Moisture Region	a_1	a_2	a_3	B(α)
1	0°-30°	Wet	0.1485	0.0372	0.0	2.854
2		Dry	0.3253	0.0069	0.0052	2.537
3	30°-60°	Wet	0.3107	0.0253	0.0	2.467
4		Inter.	0.4080	0.0337	0.0	2.024
5		Dry	1.0	0.1002	0.0120	1.852
6	60°-90°	Dry	1.139	0.1062	0.0086	1.289

where $\rho(z)$ is the mass density (in g/cm^3) of dry air at z km. (Note that we follow literature usage by expressing water vapor density units of g/m^3; however, we follow our general code usage by expressing air density in units of g/cm^3.) With the use of Equation (1) to determine $[H_2O(5,\alpha,f,L)]$, $m_R(5,\alpha,f,L)$ is determined from Equation (3b); with the use of Equation (3a) to determine $m_R(z,\alpha,f,L)$, $[H_2O(z,\alpha,f,L)]$ is determined from Equation (3b) for the range $5 < z(km) < 14$. The determination of $m_R(14,f,L)$ in Equation (3a) is described below.

2-5 WATER DENSITIES AT 14 KM AND ABOVE

Consider first the mean mass-mixing ratio (in ppmm) from 14 to 45 km. The mixing ratio data have been reviewed by Harries [Ha-76e] who recommends a mean, midlatitude vertical distribution between about 14 and 50 km. In applying this distribution to the present model, we smooth the distribution and terminate it at 45 km; above 45 km, the distribution of Harries [Ha-76e] appears to decline more rapidly than indicated by calculations (see below). This distribution is then applied over the latitude range between 0° and 90° by (a) assuming no latitude dependence between about 33° and 90°, (b) increasing the mass-mixing ratio by a factor of four in the latitude range from 0° to about 23° to account for the high tropical tropopause, and (c) providing a transition range between about 23° to about 33°. The mean vertical distribution can be represented by

$$\ln[m_R(z,L)] = 0.0619\, z^{-0.0226\, z} + \frac{30.9\, e^{-0.221\, z}}{1 + e^{0.44(L-28)}}, \qquad (4)$$

where L is the latitude. Equation (4) applies from 14 to 45 km and, for midlatitudes, represents the mean values of Harries [Ha-76e] with an error that is negligible compared with the uncertainties of the observational data.

To account for the seasonal dependence up to 20 km, the mean value is augmented by a seasonally-dependent quantity; the mass-mixing ratio is thus given by

$$\ell n[m_R(z,f,L)] = \left\{1 + 323e^{-0.448z} \sin\left[360f - \frac{6.92L}{1 + e^{-0.805(z-18)}} - 105\right]\right\}$$

$$\times \left\{0.0619ze^{-0.0226z} + \frac{30.9e^{-0.221z}}{1 + e^{0.44(L-28)}}\right\},$$

$$14 \leq z(km) \leq 45 \quad . \tag{5}$$

Equation (5) incorporates the phase shift in seasonal dependence and the decline in amplitude to negligible values at 20 km; these aspects are illustrated in Figure 2-2 for L = 39°. The arrows along the f-axis indicate the time of the maxima derived from observations [Ma-71c] and the amplitudes are indicated on the right-hand side of the figure.

It is to be understood that Equations (1) and (5) strictly apply only to the northern hemisphere. However, we will apply Equations (1) and (5) to the southern hemisphere by making the simplifying assumption of season reversal. Thus, if L < 0, we set

$$f'_{new} = f_{old} + 0.5 \; ; \tag{6a}$$

then, if $f'_{new} > 1.0$, set

$$f_{new} = f'_{new} - 1.0 \quad . \tag{6b}$$

Use only |L| in Equations (1) and (5).

Above 50 km, reliance has to be placed on water mixing ratios derived from calculations. These calculations have been previously reviewed [My-75] and a profile selected. To obtain a smooth transition between the latter and the profile presented above, values of the mass-mixing ratio between 45 and 70 km are selected by interpolation, shown in Figure 2-3; the data are given in Table 2-6. In Figure 2-3, the spread in the profiles between 20 and 30 km corresponds to the transition to increased mass-mixing ratios in the tropical

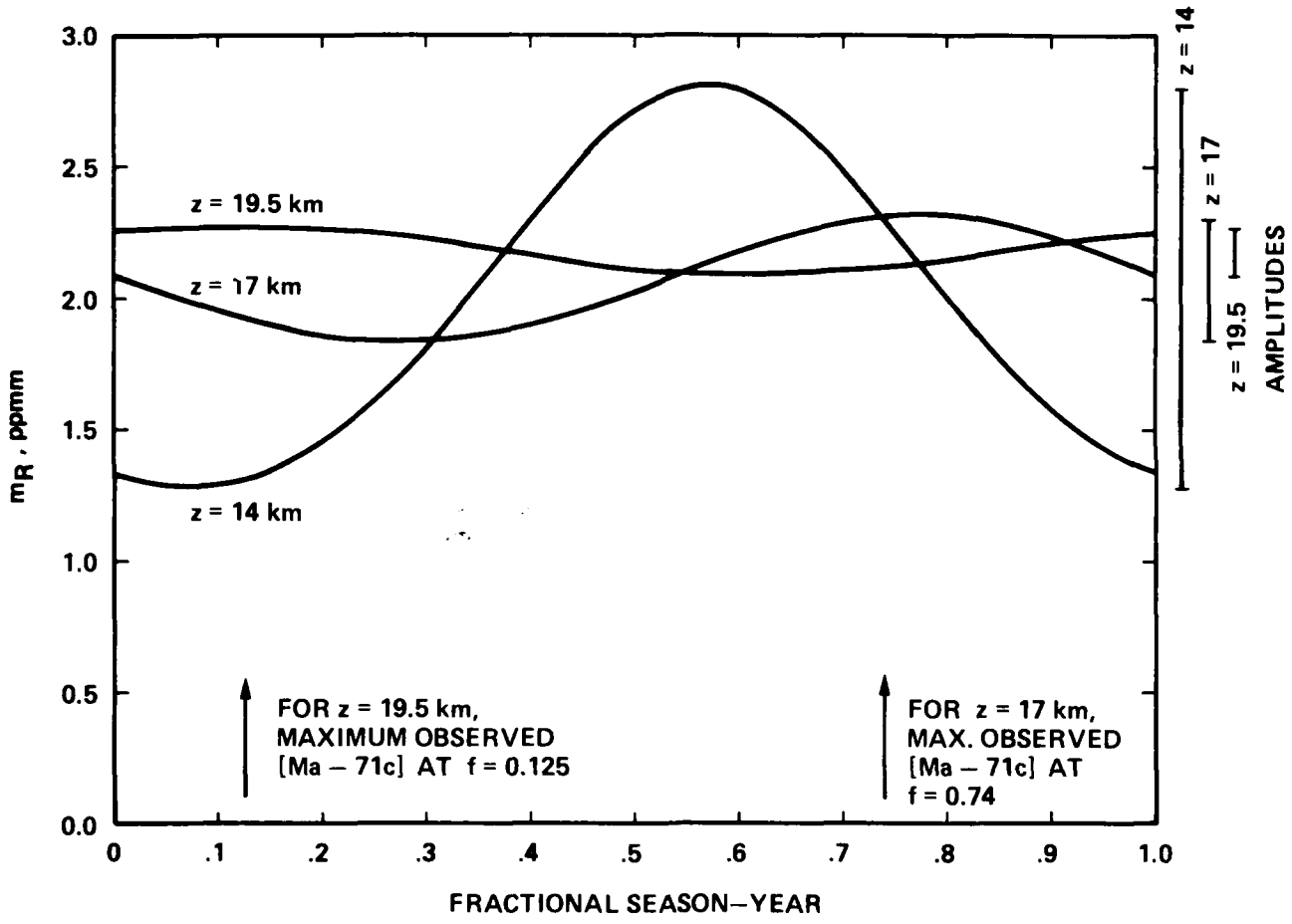

Figure 2-2. Altitude and seasonal dependence of the water vapor mass-mixing ratio between 14 and 20 km at latitude 39°, as predicted by Equation (5) of model.

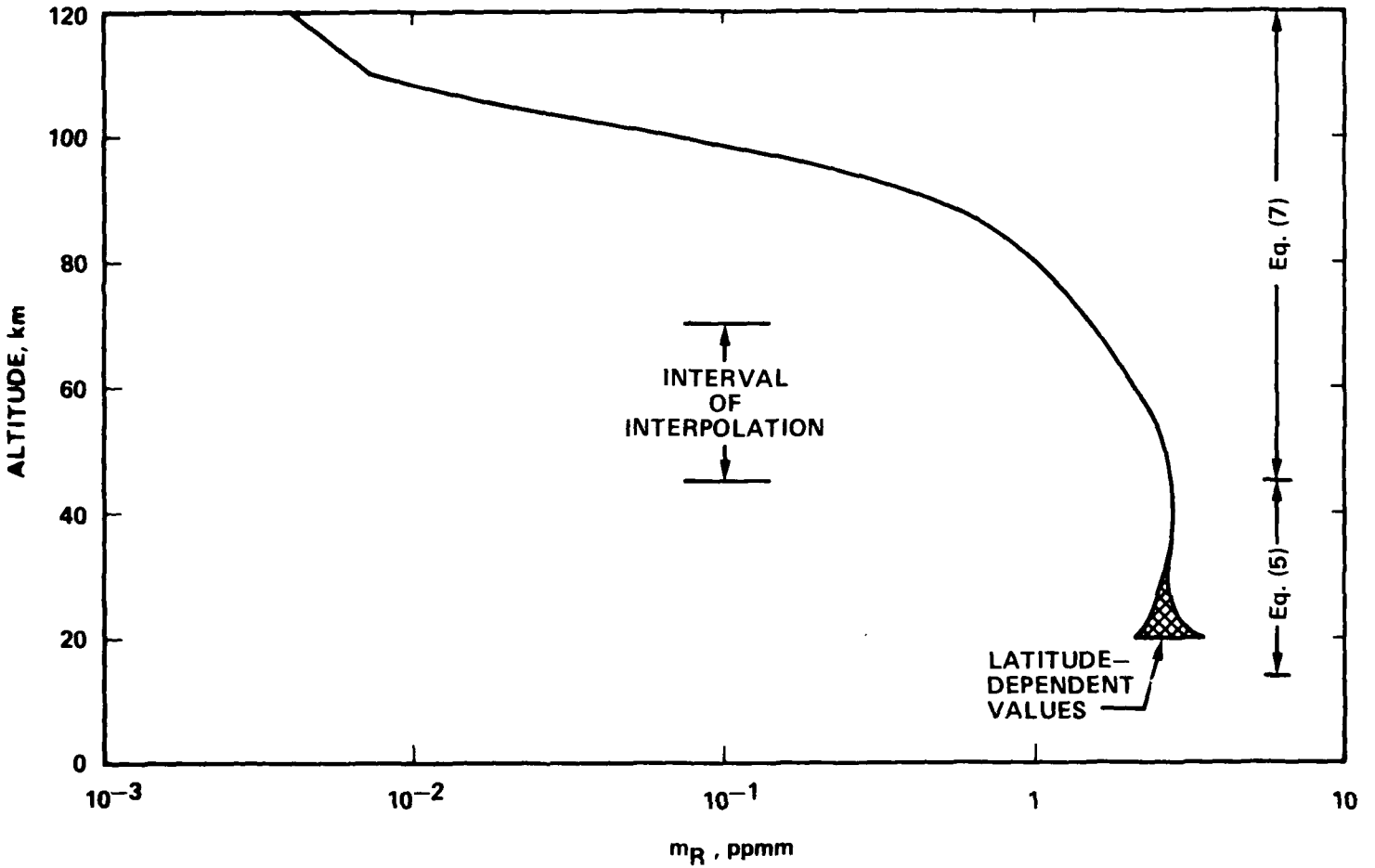

Figure 2-3. Altitude dependence of the water vapor mass-mixing ratio between 20 and 120 km. (Profile is seasonal dependent between 14 and 20 km and thus is not shown. Results of evaluating Equation (7) at 5-km intervals are joined by straight-line segments.)

Table 2-6. Selected values of water mass-mixing ratio for altitudes $z \geq 20$ km.

z(km)	ppmm	Ref.	Comment	z(km)	ppmm	Ref.	Comment
20	2.2	Ha-76e	a	75	1.25	My-75	c
25	2.39			80	0.98		
30	2.5			85	0.76		
35	2.67			90	0.46		
40	2.74			95	0.21		
45	2.71			100	0.066		
50	2.6		b	105	0.018		
55	2.36			110	0.0075		
60	2.1			115	0.0053		b
65	1.8			120	0.0040	My-75	c
70	1.51	My-75	c	>120			d

[a] Values in the 20- to 40-km range are retained for the possible benefit of the user who wants to exercise an optional input.

[b] Interpolation.

[c] Densities from My-75 were converted to ppmm by using mass densities of air taken from US-66.

[d] $m_R = m_R(120) \exp[-0.0575(z-120)]$, $z > 120$ km.

regions ($L \lesssim 23°$) as discussed above. Table 2-6 gives the mass-mixing ratios up to 120 km and provides a formula for calculating the mixing ratios above 120-km altitude. Between 45 and 120 km, the mass-mixing ratios are represented within 4.5 percent by the formula

$$\ell n[m_R(z)] = \sum_{i=1}^{13} b_i z^{i-1} \qquad (7)$$

where the coefficients b_i are given in Table 2-7. (Note that, in practice, coefficients with the full CDC-machine accuracy must be used in Equation (7); see Volume 14a-1.)

Table 2-7. Coefficients for least-squares polynomial fit of mass-mixing ratios between 45 and 120 km (per Equation (7)).

i	b_i	i	b_i	i	b_i
1	-1.1133052(1)	6	5.6976779(-6)	11	1.4175461(-16)
2	2.4232553(0)	7	-5.7316192(-8)	12	5.7833135(-20)
3	-2.1276475(-1)	8	1.4622167(-10)	13	-1.0792550(-21)
4	1.0471519(-2)	9	3.3455169(-12)		
5	-3.1267414(-4)	10	-3.8722824(-14)		

2-6 LATE REPORTS FOR MEASUREMENTS OF WATER CONTENT

Measurements of the water content between 49 and 70 km have been made at 65°N by using a rocketborne, cryogenic spectrometer [RS-77]. The average water content was (3.5 ± 2.2) ppmv in this altitude range. The average water content deduced from the above model is 3.3 ppmv.

By contrast, much higher water mixing ratios were obtained at 42°N between 50 and 80 km from ground-based microwave observations [RL-77]. Here, a maximum of 15 ppmv was deduced for 60 km and values ranged between 3 and 15 ppmv between 50 and 80 km. The error in these measurements could be as high as ±40 percent and time-dependent

variations may be important in resolving the difference between these measurements and expectations based on model calculations [Cr-74a]; the latter predict a maximum of 6 ppmv in the altitude range from 50 to 80 km. Also, no latitude dependence has been established for these altitudes so that a potential discrepancy between these two recent works [RL-77, RS-77] exists.

SECTION 3

A MODEL FOR OZONE PROFILES

3-1 INTRODUCTION

As for water, a more accurate and therefore detailed model of atmospheric ozone is required in ROSCOE-IR than is present in ROSCOE-Radar. This requirement demands a careful modeling of the ozone content at altitudes below 50 km where the bulk of the ozone is found.

The model presented below yields ozone profiles as a function of altitude, latitude, and season; the longitudinal dependence is relatively small and was neglected. Other effects not included in the model are day-to-day fluctuations and very long-term trends [DT-75 (p. 3-28), RC-75b, RF-76]. The data base of the model consists of (a) the midlatitude ozone model for the 1976 U.S. Standard Atmosphere [KM-76a, US-76], (b) data on seasonal, latitudinal, and longitudinal variations [Du-70a, Du-71, Du-74, DT-75] at altitudes below 55 km, and (c) data from a review by Myers [My-75] at altitudes above 55 km.

3-2 GENERAL DESCRIPTION OF THE MODEL

The earth's atmosphere is divided into two shells separated by a boundary at 55 km for describing the ozone content based on available data. At altitudes below 55 km, the model accounts for the variation of ozone with altitude, latitude, and time of year. The dependence on latitude is continuous and not in terms of latitude regions as in the model for water. The variation of ozone with latitude becomes negligible as the altitude approaches 55 km. The seasonal variation has a maximum in the altitude range between 15 and 35 km, depending on latitude, and declines on either side of the maximum such that the altitude range at half maximum is approximately 10 km. The seasonal maximum also varies with the time of the year, shifting from late December to April in the northern hemisphere as the altitude decreases from about 30 to 10 km.

Above 55-km altitude, the model is the same as previously presented [My-75]. A diurnal variation in ozone content is included but no seasonal or geographical effects are treated. Note that the nighttime ozone density only varies significantly from the daytime ozone density at altitudes above about 55 km according to theoretical expectations [Ca-74] and according to observations [CH-66a, Re-68c, Hi-71a, CH-72].

The basic description of the ozone content of the atmosphere is given in terms of the mass-mixing ratio. The model predictions are presented below for selected calculations in terms of the mass-mixing ratio and also in terms of the partial pressure of ozone to provide the option of comparing model predictions with literature data.

3-3 OZONE PROFILE UP TO 55 KM

The model for altitudes up to 55 km is presented in two parts: (a) the mean, seasonal values of the mass-mixing ratio and partial pressure are formulated as a function of latitude and altitude, and (b) the seasonal dependence is formulated.

3-3.1 Annual-Mean Ozone Profile ($0 \leq z(km) \leq 55$)

The data on which fits for the annual-mean ozone profile were based are (a) the 1976 U.S. Standard Atmosphere midlatitude data [KM-76a, US-76] and (b) data covering a range of latitudes as presented by Dütsch [Du-74]. The latter data (for the northern hemisphere) are given for spring (March/April) and fall (October/November); in using these data to derive annual-mean values, their averages were used. The averages from the data of Dütsch [Du-74] for 47^{o}N latitude are in good agreement with the midlatitude data of the 1976 U.S. Standard Amosphere ozone model [US-76], as shown in Table 3-1. The data employed in arriving at the annual-mean values are listed in Table 3-2. These data are fit with the following function for the annual-mean mass-mixing ratio, $\bar{m}_R$(kg/kg):

Table 3-1. Comparison of ozone mass-mixing ratio (kg/kg) data from US-76 and from Du-74.

z, km	US-76 Midlatitude	Du-74 45°[c]	z, km	US-76 Midlatitude	Du-74 45°[c]
≈0	5.15(-8)[a]	5.15(-8)	20	4.27(-6)	4.00(-6)
5	6.20(-8)[b]	6.40(-8)	25	8.58(-6)[b]	8.00(-6)
10	2.18(-7)	1.35(-7)	30	1.09(-5)	1.05(-5)
15	1.12(-6)[b]	9.05(-6)	35	1.31(-5)[b]	1.25(-5)

[a]Extrapolated value.

[b]Average of values listed [US-76] at z+1 and z-1.

[c]Graphical-interpolation values from data of Table 3-2.

Table 3-2. Ozone mass-mixing ratio data[a] as a function of altitude for selected latitudes.

	$\bar{m}_R$(kg/kg)						
z,km	L=9°	22°	35°	47°	59°	71°	85°
0	3.11(-8)	3.92(-8)	4.41(-8)	[5.30(-8)]	4.42(-8)	4.25(-8)	1.80(-8)
5	3.68(-8)	4.90(-8)	5.52(-8)	6.59(-8)	6.75(-8)	6.13(-8)	7.66(-8)
10	5.00(-8)	6.88(-8)	9.38(-8)	1.44(-7)	4.06(-7)	4.94(-7)	2.38(-7)
15	9.58(-8)	1.64(-7)	5.20(-7)	9.31(-7)	1.96(-6)	2.16(-6)	2.05(-6)
20	1.56(-6)	2.76(-6)	3.30(-6)	4.14(-6)	5.67(-6)	5.76(-6)	5.21(-6)
25	8.84(-6)	9.75(-6)	8.39(-6)	7.87(-6)	8.06(-6)	7.15(-6)	6.50(-6)
30	1.50(-5)	1.34(-5)	1.16(-5)	1.02(-5)	8.30(-6)	7.20(-6)	
35	1.64(-5)	1.55(-5)	1.55(-5)	[1.18(-5)]	7.50(-6)	4.90(-6)	

[a]Data based on Du-74, Figure 6.

$$\bar{m}_R(z,L) = \frac{\left[\frac{A(1+0.27z)}{1+e^{B(z-z_{01})}} + \frac{D}{1+e^{-E(z-z_{02})+F/(z^5+100)}}\right]}{1+e^{\alpha_t(z-z_{ot})}} \quad (1)$$

where

$$A = 2.66 \times 10^{-9}\,(105-L)e^{-\frac{105-L}{47}} \quad (2)$$

$$B = 0.988 + 0.0136L \quad (3)$$

$$D = (1.837 - 0.014L) \times 10^{-5} \quad (3)$$

$$E = \frac{0.5}{1+e^{0.077(L-44)}} + 6.0 \times 10^{-5}L^2 - 0.014 \quad (4)$$

$$F = \left[L - \frac{35}{1+e^{-0.243(L-80)}}\right]^2 \quad (6)$$

$$z = \text{altitude, km} \quad (7)$$

$$z_{01} = 12.54 - 0.093L + \frac{6}{1+e^{-0.318(L-85.5)}} \quad (8)$$

$$z_{02} = 29.2 - 0.153L - \frac{6}{1+e^{0.08(L-10)}} \quad (9)$$

$$L = \text{latitude, degrees} \quad 0 \leq L \leq 90 \quad (10)$$

$$\alpha_t = 0.20 - 6.78 \times 10^{-4}L \quad (11)$$

$$z_{ot} = 46.9 + 6.62 \times 10^{-3}L + 7.24 \times 10^{-4}L^2\ . \quad (12)$$

This mass-mixing ratio as a function of altitude for selected latitudes is shown in Figure 3-1. In Figure 3-2, profiles of the ozone partial pressure are shown for the same selected latitudes. The ozone partial pressure, in nanobars (nb), is calculated from the relationship

$$P_{03}(\text{nb}) = \frac{\bar{m}_R P_{air}(\text{mb})}{1.6571 \times 10^{-6}} \quad (13)$$

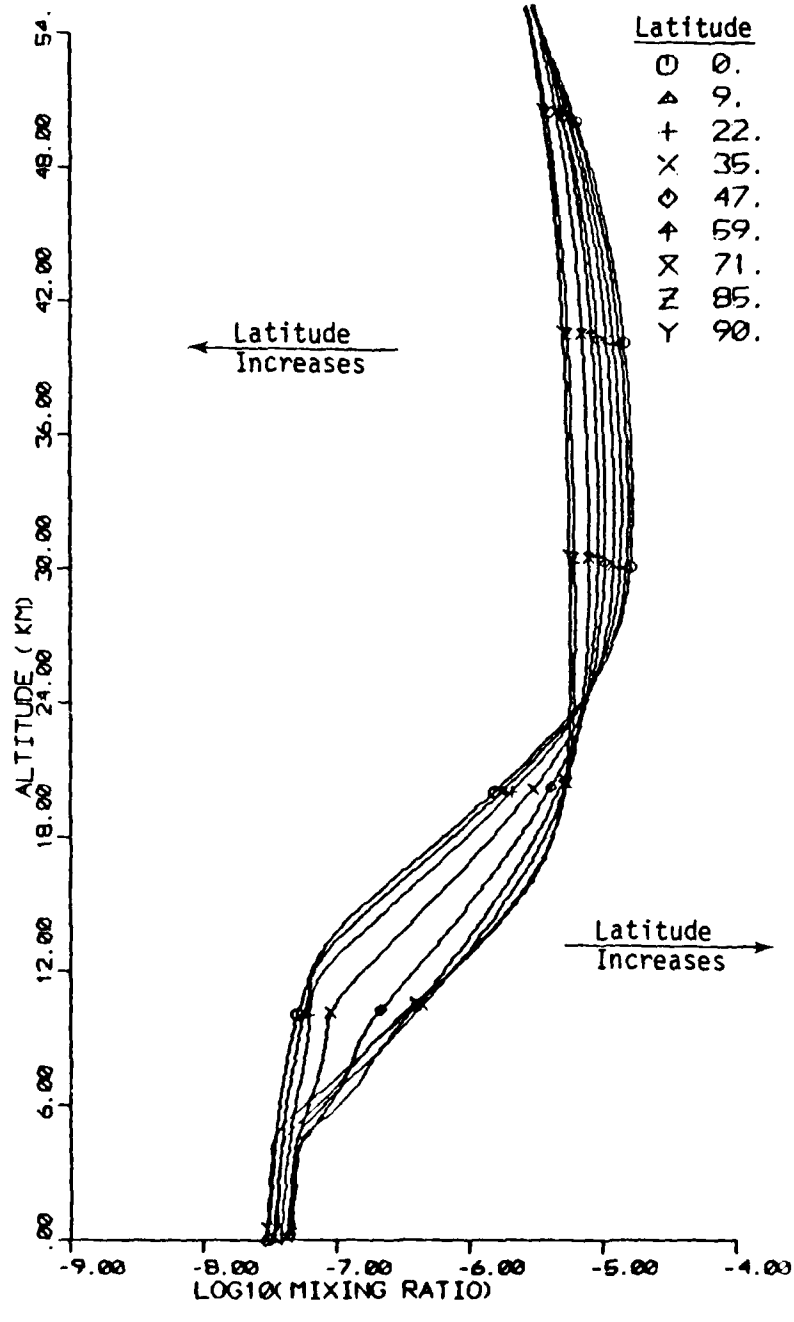

Figure 3-1. Annual-mean profiles of ozone mass-mixing ratio (kg/kg) at selected latitudes.

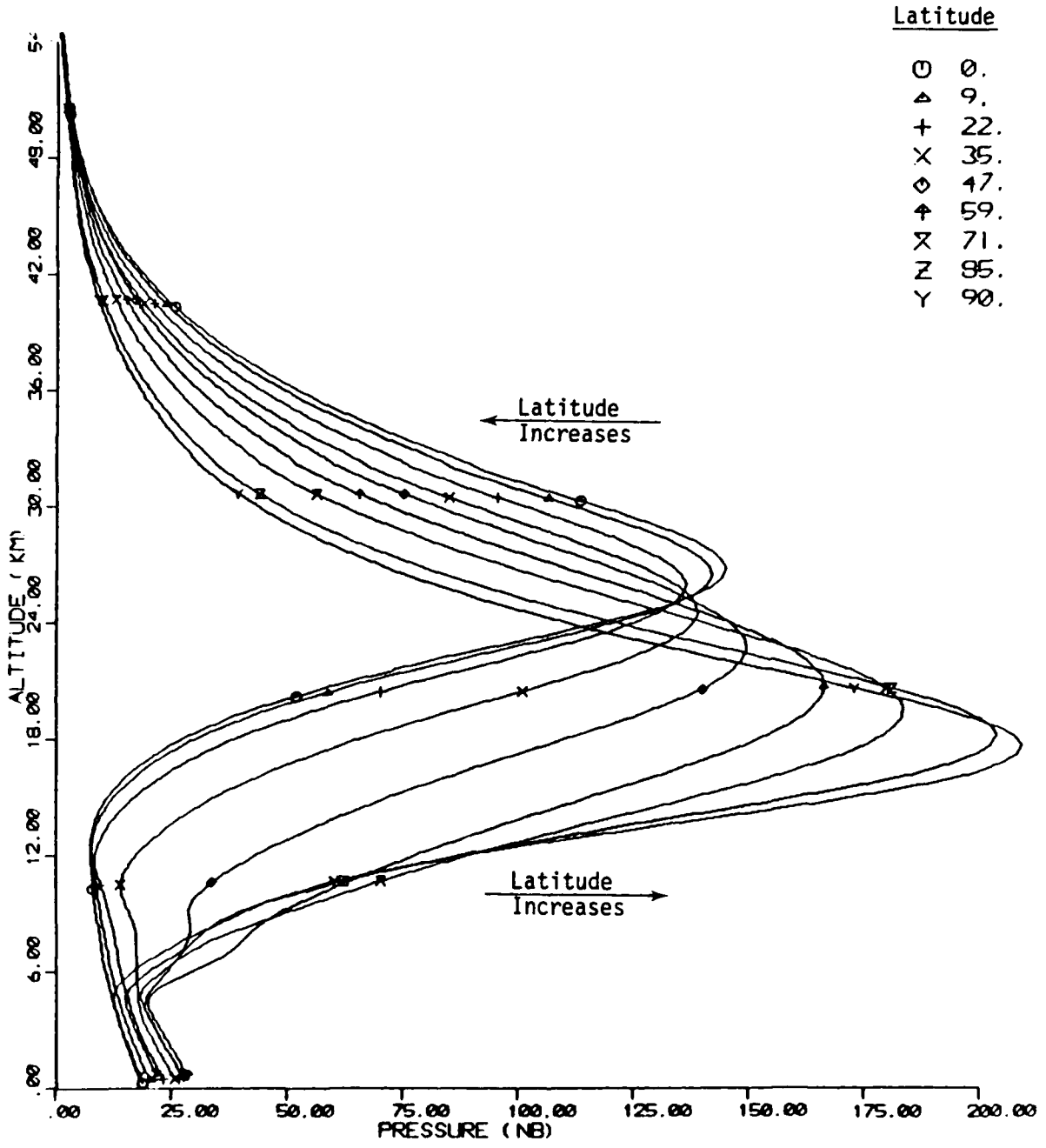

Figure 3-2. Annual-mean profiles of the ozone partial pressure at selected latitudes.

where P_{air}(mb) is the total air pressure in millibars (mb) which, for the purpose of illustrative calculations represented by Figure 3-2, was taken from US-76.

Qualitative features of the data reflected in the fit function, Equation (1), as shown in Figure 3-2, include (a) increase in the total ozone content of the atmosphere as latitude increases, (b) decrease in the ozone partial pressure above 24 km as latitude increases, and (c) a general increase in the maximum ozone partial pressure with increasing latitude with a concomitant decrease in the altitude at which the maximum occurs. Because of the lack of data on latitude dependence above 30 km, the fit function, Equation (1), was constructed to produce a decrease in the latitudinal variation of ozone content with increasing altitude; at 55 km, the ozone mass-mixing ratio (for the seasonally-dependent value) is fixed to be the same at all latitudes with a value of 3.1×10^{-6} kg/kg (see Section 3-3.2).

3-3.2 Seasonal Dependence of Ozone Profile ($0 \leq z(km) \leq 55$)

The seasonal dependence of the ozone mass-mixing ratio is included by adding a periodic function to Equation (1). The form and magnitude of this function are determined from the available data for a latitude of 47°N [Du-74, Figure 14]. These data, in units appropriate to this report, are presented in Table 3-3 in terms of $2\Delta m_R$, the seasonal range in the mass-mixing ratio and the month (or fractional month) at which the maximum value of the mass-mixing ratio occurs. To account for the shift in the maximum, a phase shift function, $\phi+\theta(z)$, is incorporated into the periodic function; ϕ is the reference phase angle and $\theta(z)$ accounts for the shift in phase angle with altitude, z. The variation in the seasonal amplitude in the mass-mixing ratio with latitude is estimated by using the data of Du-74, Figure 6; more extensive data apparently are not available. The seasonal amplitude of these data are listed in Table 3-4. The variation in the seasonal maximum is apparently weak (see Du-74, Figure 1), and is neglected in the present model.

The above treatment of the seasonal dependence of the mass-mixing ratio, m_R, leads to the following equation:

Table 3-3. Data on seasonal range[a] of the ozone mass-mixing ratio at 47°N.[b]

z km	$2\Delta m_R$ kg/kg	Month of Maximum[c]	z km	$2\Delta m_R$ kg/kg	Month of Maximum[c]
11.8	5.37(-7)	4	22.1	2.07(-6)	∿2
13.6	8.39(-7)	3.5	23.9	1.94(-6)	1
16.2	8.12(-7)	3.2	25.1	1.66(-6)	1
18.5	1.18(-6)	3.0	26.6	1.38(-6)	∿1
20.6	1.78(-6)	2.8			

[a] Range is twice the amplitude (Δm_R).

[b] Adapted from Du-74.

[c] January is 1, etc.

Table 3-4. Data on latitude dependence of the seasonal amplitude[a] of the ozone mass-mixing ratio, at selected altitudes.

z km	Δm_R, kg/kg						
	L = 9°	22°	35°	47°	59°	71°	85°
0	8.18(-9)	8.16(-9)	9.80(-9)	-	3.27(-9)	1.63(-9)	4.90(-9)
5	9.20(-9)	1.23(-8)	6.13(-9)	7.66(-9)	6.13(-9)	1.23(-8)	9.19(-9)
10	6.25(-9)	1.25(-8)	3.13(-8)	6.89(-8)	1.50(-7)	1.81(-7)	1.00(-7)
15	-	2.73(-8)	1.64(-7)	3.42(-7)	3.57(-7)	3.28(-7)	6.38(-7)
20	6.0 (-8)	3.0 (-8)	3.90(-7)	6.60(-7)	1.26(-6)	9.00(-7)	1.08(-6)
25	1.95(-7)	4.55(-7)	1.95(-7)	1.95(-7)	4.55(-7)	6.50(-7)	1.43(-6)
30	1.51(-6)	9.67(-7)	2.76(-7)	2.76(-7)	2.77(-7)	2.76(-7)	8.3 (-7)

[a] Amplitude is half the range.

$$m_R(z,f,L) = \frac{1.05 \times 10^{-6}}{\left[1 + e^{-\alpha(z-z_{01c})}\right]\left[1 + e^{\beta(z-z_{02c})}\right]}$$

$$\times \sin\left\{306f - 60.12\left[\frac{1}{1+e^{1.465(z-22.1)}} + \frac{0.665}{1+e^{0.7(z-13.2)}}\right]\right\}$$

$$+ \bar{m}_R(z,L), \quad \text{kg/kg} \tag{14}$$

where

$$\alpha = 0.235 + \frac{0.295}{1 + e^{-0.0982(L-37)}} \tag{15}$$

$$\beta = 0.55 + \frac{0.4}{1 + e^{0.094(L-38)}} \tag{16}$$

$$z_{01c} = 31.0 - 0.329L + \frac{11.6}{1 + e^{-0.112(L-74)}} \tag{17}$$

$$z_{02c} = 37.5 - 0.195L + \frac{9.49}{1 + e^{-0.195(L-75)}} \tag{18}$$

f = fractional part of year,

and $\bar{m}_R(z,L)$ is given by Equation (1).

To provide a common value of the mass-mixing ratio, m_R, at 55 km for latitudes and seasons as stipulated above, the calculation of m_R, in the altitude range $53.0 \leq z(\text{km}) \leq 55.0$, is made according to the prescription

$$m_R + (3.1 \times 10^{-6} - m_R)\delta_{ps}$$

where δ_{ps} is the Kroneker delta function, p represents a positive sign and s is the sign of the quantity $(3.1 \times 10^{-6} - m_R)$.

The seasonal dependence (in the northern hemisphere) is illustrated in Figures 3-3a through 3-3d and 3-4a through 3-4d where the ozone partial pressure is shown as a function of the fraction of year for (a) selected altitudes at latitudes of 9°, 35°, 59°, and 85° and (b) selected latitudes at altitudes of 5, 15, 25, and 35 km, respectively.

It is to be understood that Equations (14) through (19) strictly apply only to the northern hemisphere. However, we will apply these equations to the southern hemisphere by making the simplifying assumption of season reversal. Thus, if $L < 0$, we set

$$f'_{new} = f_{old} + 0.5 \quad ;$$

then, if $f'_{new} > 1.0$, set

$$f_{new} = f'_{new} - 1.0 \quad .$$

Use only $|L|$ in Equations (14) through (18).

3-3.3 Longitudinal Dependence of Ozone Profile

The ozone concentration varies longitudinally. The variation of the annual-mean ozone concentration and of the seasonal amplitude have been considered on the basis of data presented in the CIAP Monograph 1 [DT-75]. The maximum variation of the annual-mean concentration is ± 10 percent and that of the seasonal amplitude is ± 15 percent; these variations are regarded as negligible for the present model.

3-4 OZONE PROFILE ABOVE 55 KM

The ozone profiles for altitudes above 55 km have been presented previously [My-75]. These profiles account for diurnal variations in ozone but not for geographical variations. The mixing ratio data for altitudes of 55 km and above are listed in Table 3-5 and shown in Figure 3-5.

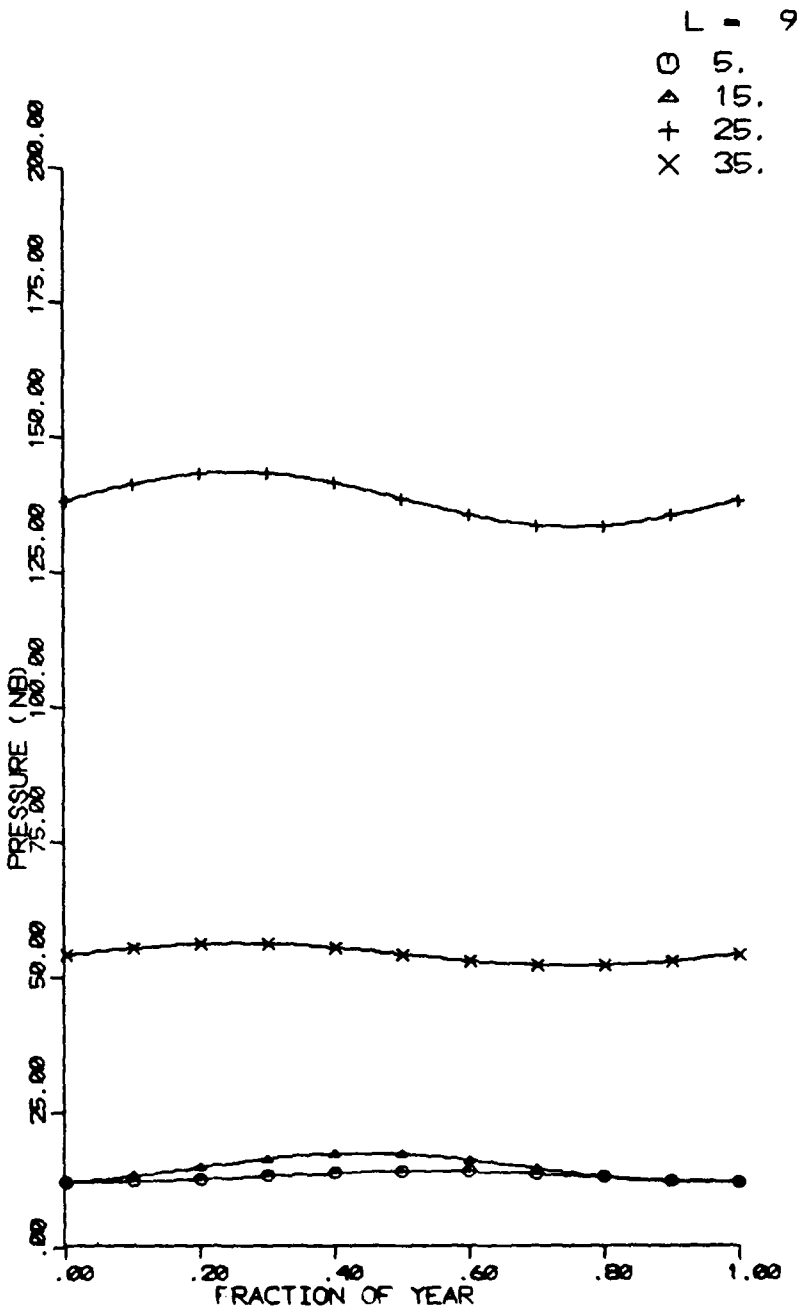

Figure 3-3a. Seasonal variation of ozone partial pressure at 9°-latitude, for selected altitudes.

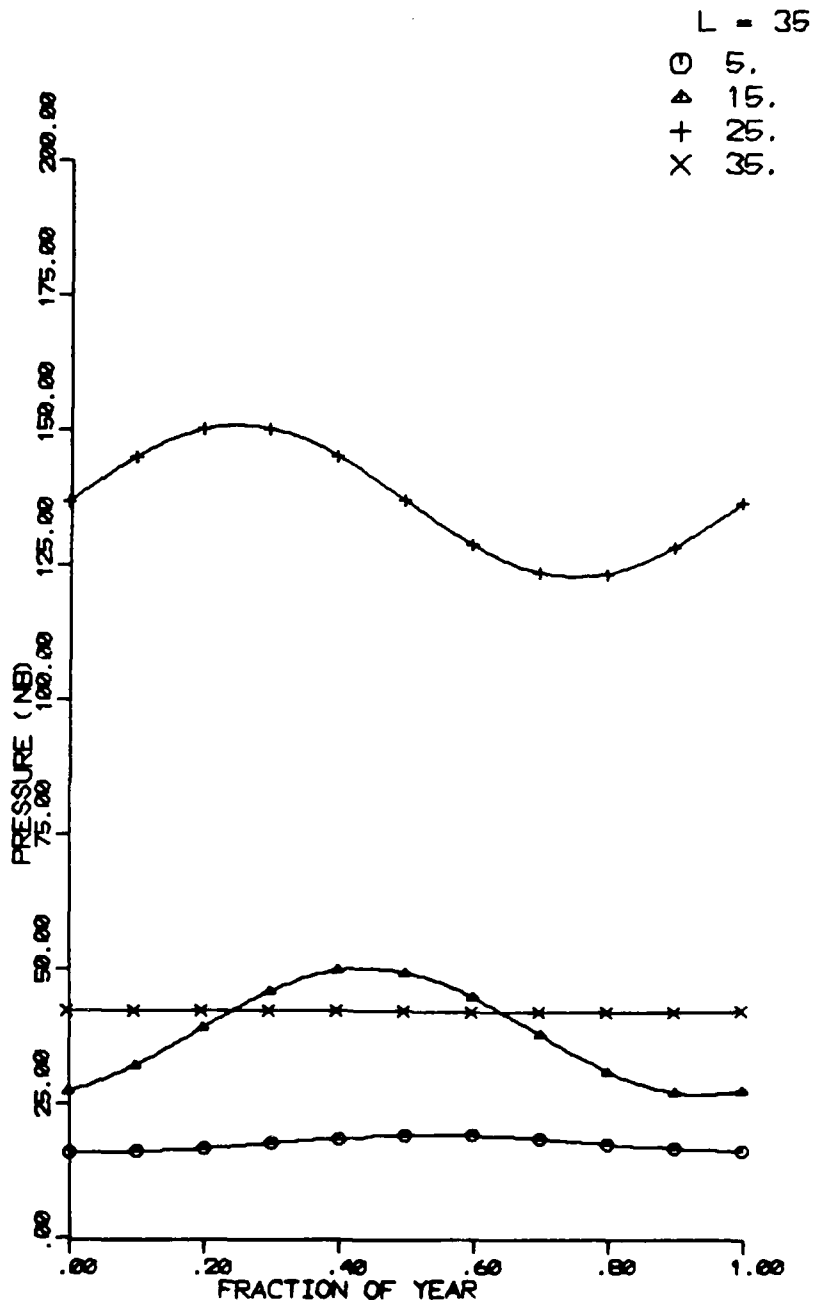

Figure 3-3b. Seasonal variation of ozone partial pressure at 35°-latitude, for selected altitudes.

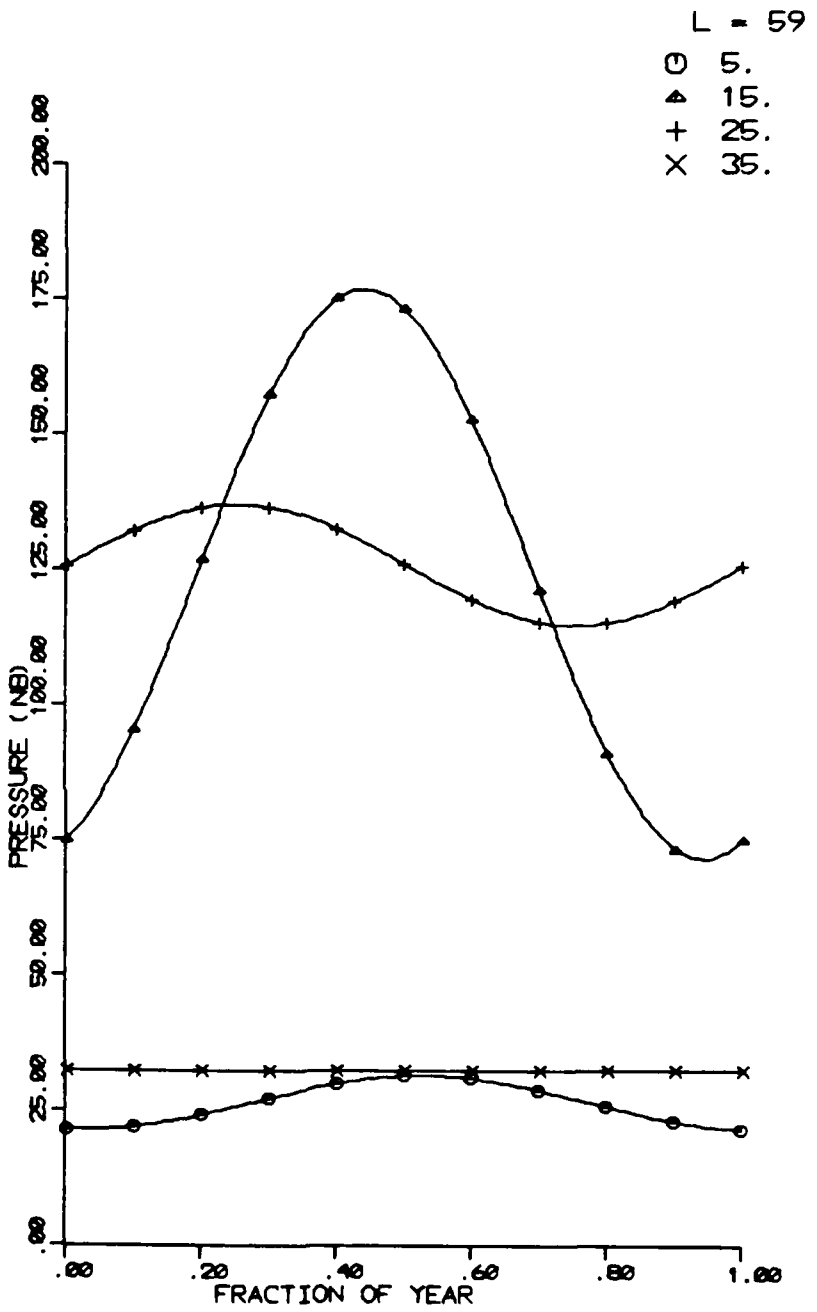

Figure 3-3c. Seasonal variation of ozone partial pressure at 59°-latitude, for selected altitudes.

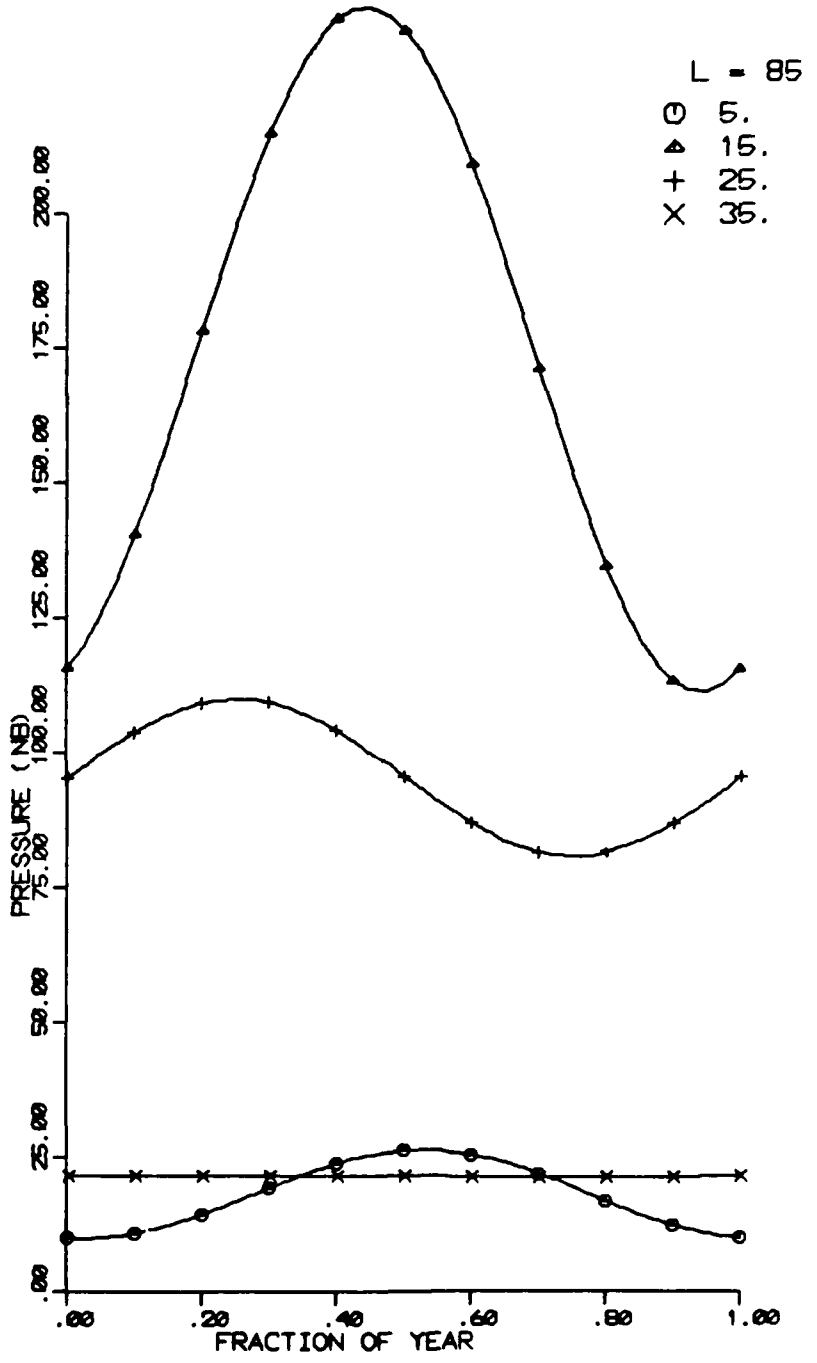

Figure 3-3d. Seasonal variation of ozone partial pressure at 85°-latitude, for selected altitudes.

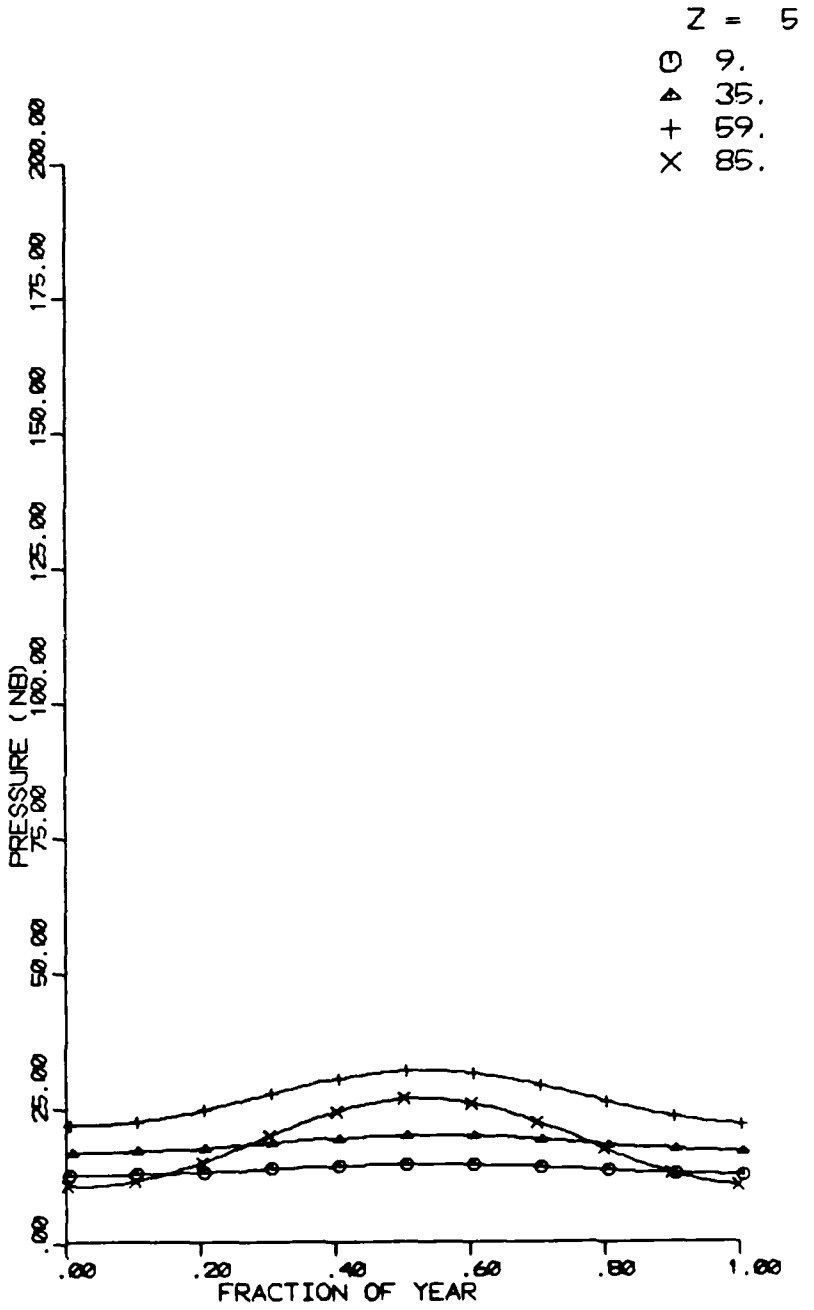

Figure 3-4a. Seasonal variation of ozone partial pressure at 5-km altitude, for selected latitudes.

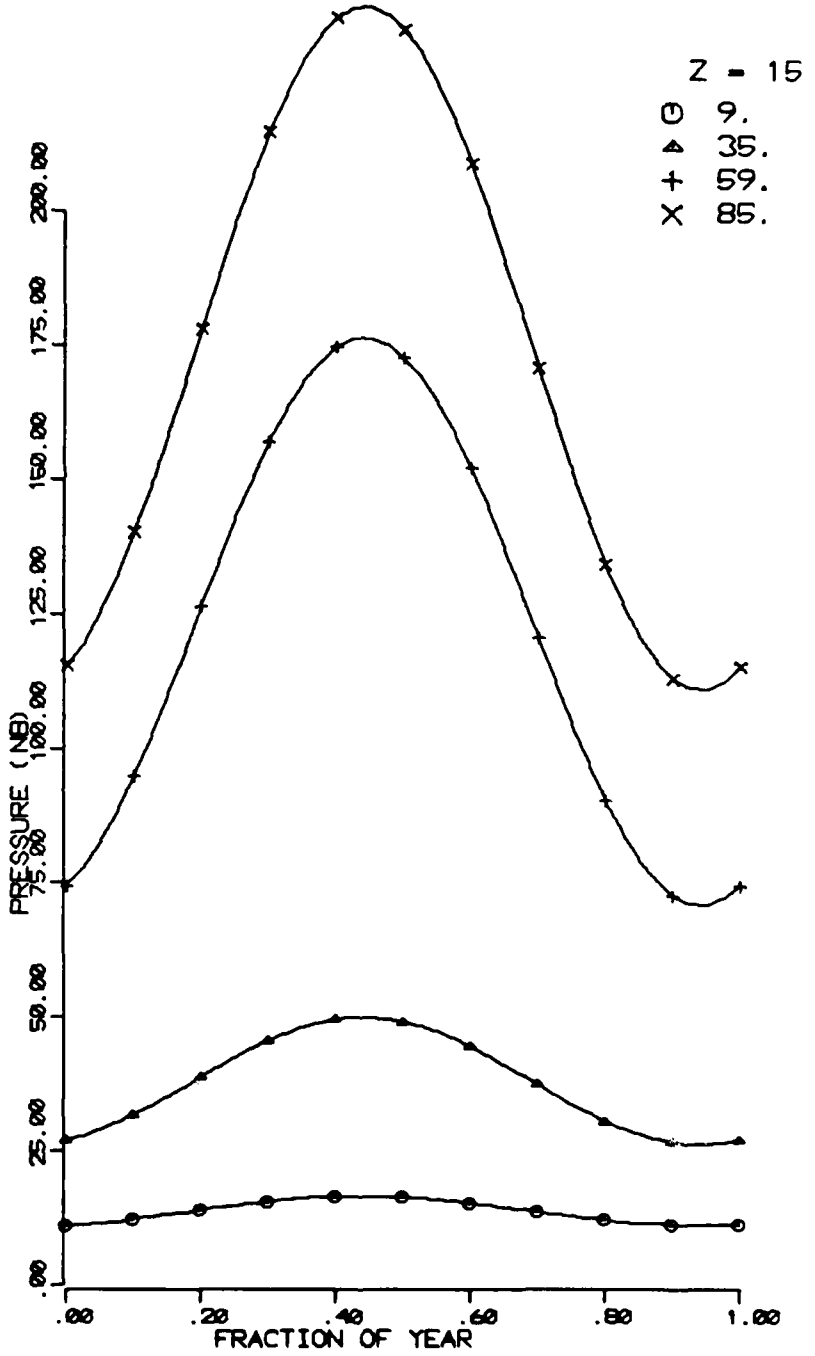

Figurd 3-4b. Seasonal variation of ozone partial pressure at 15-km altitude, for selected latitudes.

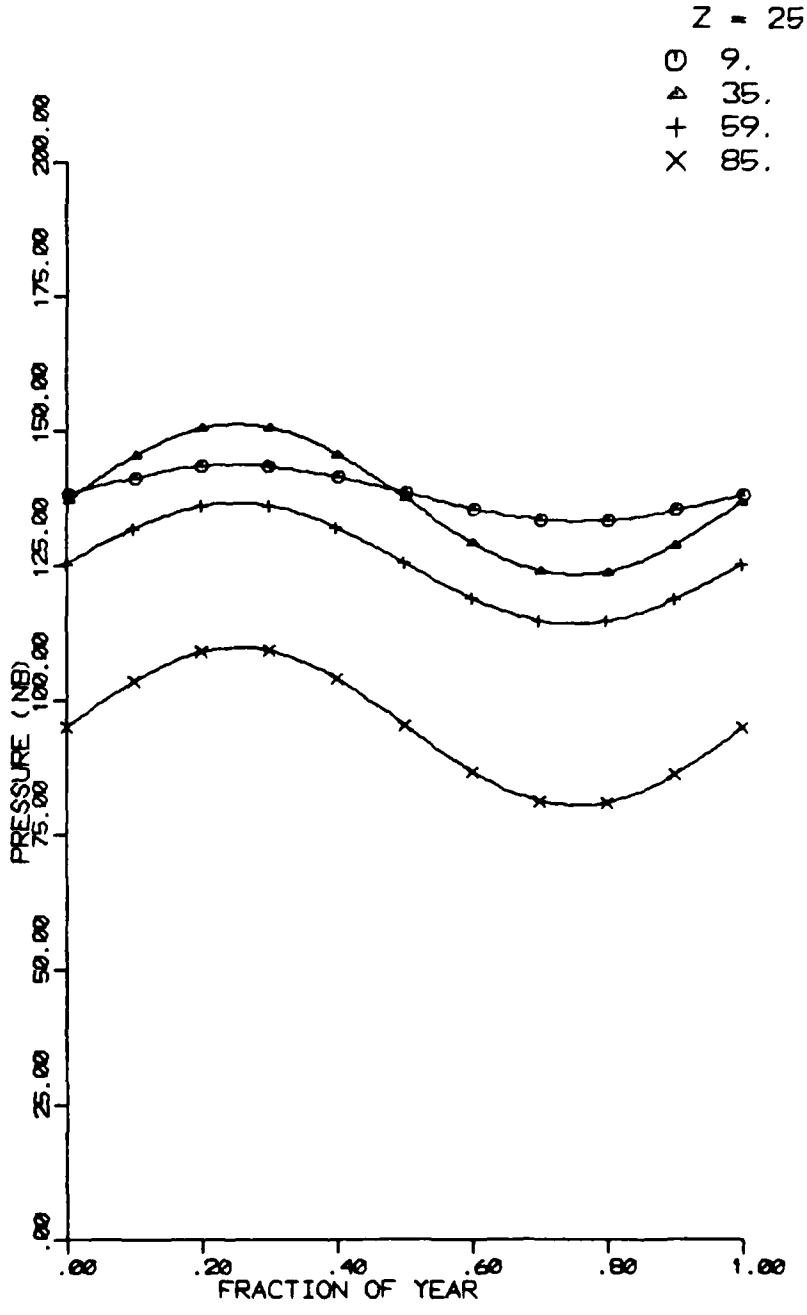

Figure 3-4c. Seasonal variation of ozone partial pressure at 25-km altitude, for selected latitudes.

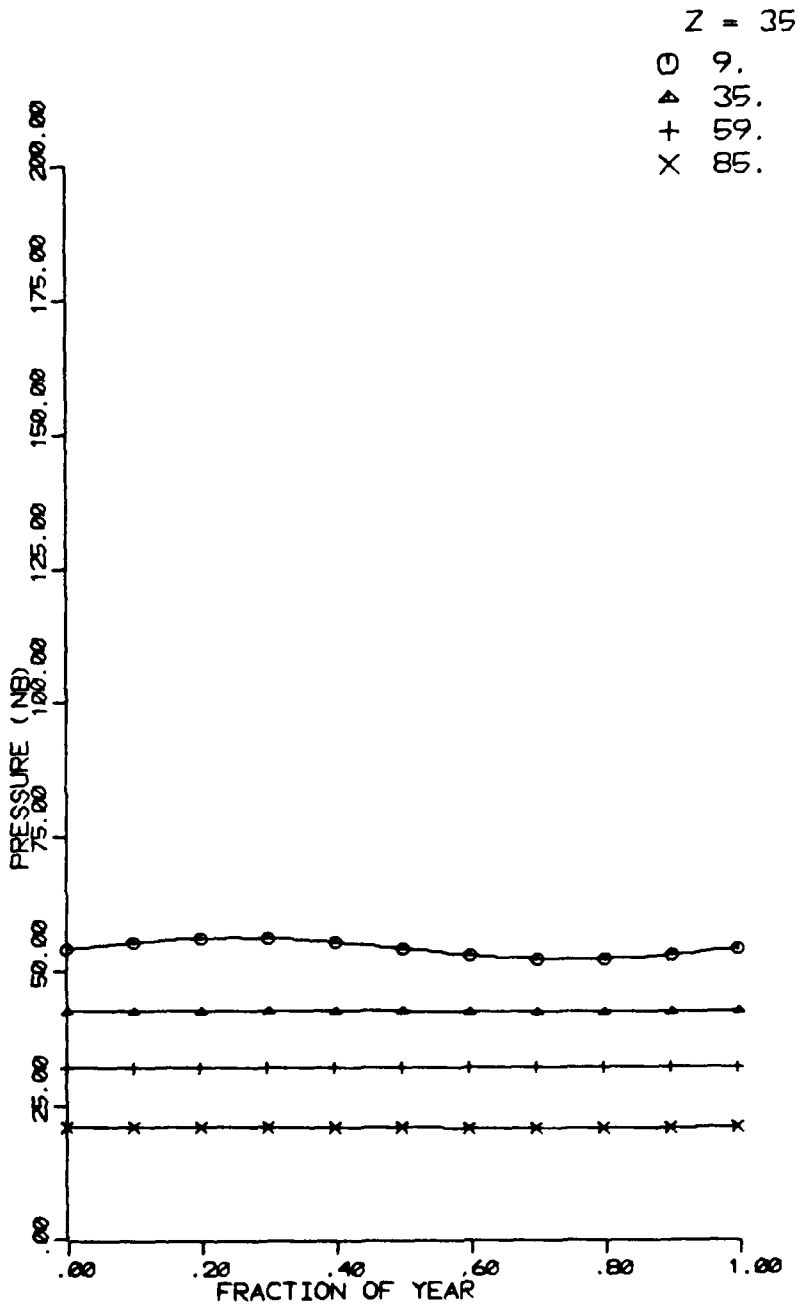

Figure 3-4d. Seasonal variation of ozone partial pressure at 35-km altitude, for selected latitudes.

Table 3-5. Data[a] on ozone mass-mixing ratio at 55-km and higher altitudes.

z km	m_R(kg/kg) Noon	m_R(kg/kg) Midnight	z km	m_R(kg/kg) Noon	m_R(kg/kg) Midnight
55	3.1(-6)	3.1(-6)	95	1.4(-7)	1.5(-6)
60	1.9(-6)	3.3(-6)	100	3.6(-8)	3.8(-7)
65	1.0(-6)	5.9(-6)	105	1.2(-8)	9.9(-8)
70	5.3(-7)	4.3(-6)	110	3.0(-9)	3.3(-8)
75	2.6(-7)	1.5(-6)	115	7.1(-10)	6.5(-9)
80	2.9(-7)	2.6(-7)	120	1.5(-10)	6.8(-10)
85	1.2(-6)	5.6(-6)	>120	b	c
90	7.0(-7)	4.0(-6)			

[a] Data from Table 4-2 of My-75 converted to units of mass-mixing ratio, with densities from US-76:

$$m_R(\text{kg/kg}) = [O_3(\text{cm}^{-3})]/[1.255 \times 10^{19}\ \rho_{air}(\text{kg/m}^3)].$$

At 55 km, the above values differ from those derived from My-75 to ensure continuity in m_R.

[b] $m_R(>120) = m_R(120)e^{-0.24(z-120)}$.

[c] $m_R(>120) = m_R(120)e^{-0.30(z-120)}$.

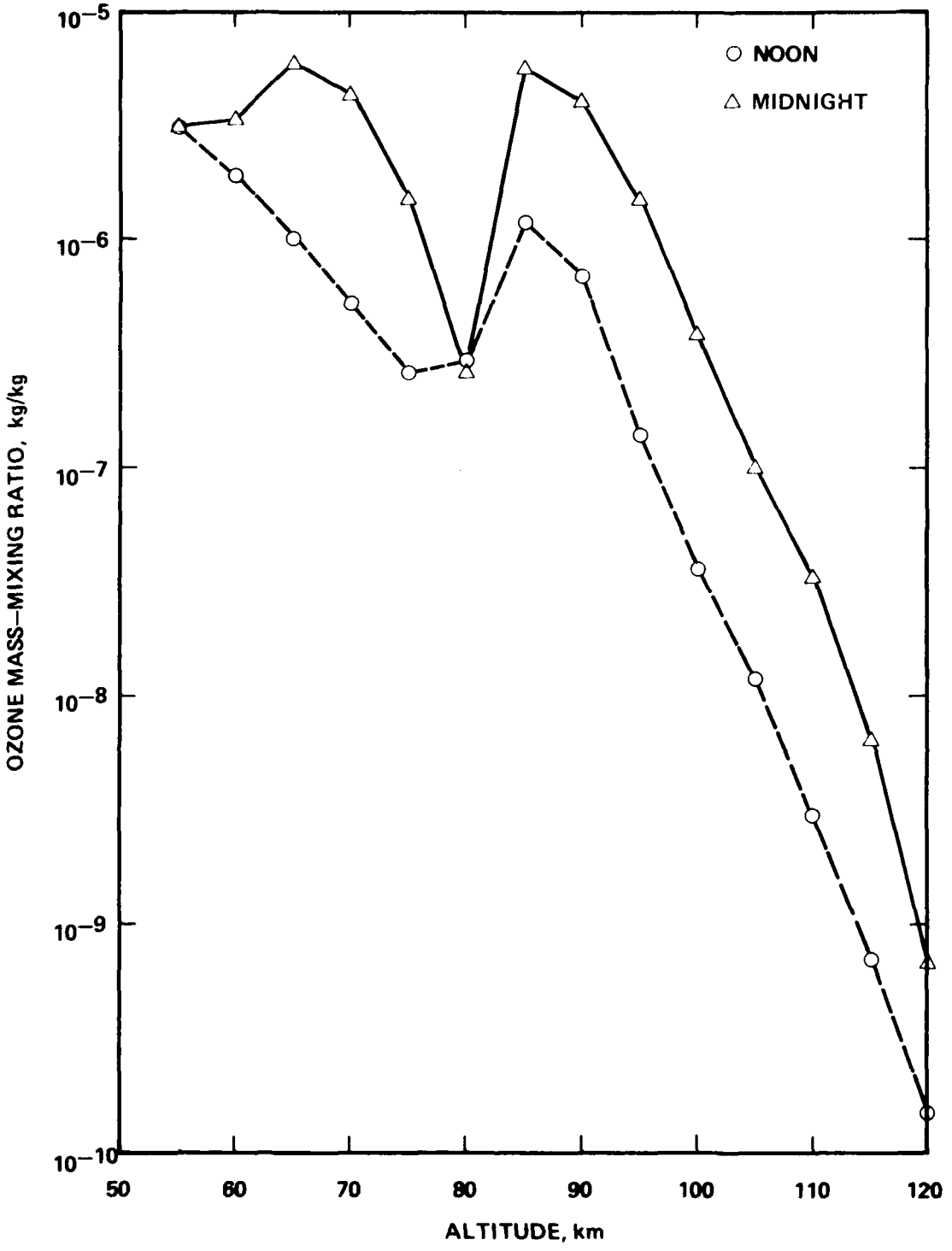

Figure 3-5. Dependence of ozone mass-mixing ratio between 55- and 120-km altitude, for noon and midnight conditions.

SECTION 4

A MASS-MIXING RATIO PROFILE FOR METHANE

4-1 INTRODUCTION

Measurements of the methane composition of the atmosphere as a function of altitude have been made from ground level to about 50 km [DT-75]. Above 50 km, reliance has to be placed on model calculations [Hu-73a].

Satellite measurements [PD-74] show that the global and seasonal variation of the total methane content is less than 25 percent of the mean value. However, in the stratosphere, there are indications [FR-74] of larger variations in the mixing ratio as a function of latitude. Thus, questions remain about the geographical and seasonal dependence of the methane content; consequently, the present model is presented as a mean-value model.

4-2 THE METHANE PROFILE

The data on which the profile for methane is based are given in Table 4-1. The reference data [DT-74, Hu-73a] are given either in ppmv (parts per million by volume) or in molecules/m^3 and are converted, as shown in Table 4-1, to ppmm (parts per million by mass). For the conversions from molecules/m^3 to ppmm, the atmospheric densities were those used in the references. For DT-75, a density function is provided and for Hu-73a, the CIRA-65 mean atmosphere [CI-65] was used. The data listed as being from DT-75 are based on an estimated mean of the data compiled in Figure 3.82 of that reference. The data of Table 4-1 are plotted in Figure 4-1. Above z = 120 km, an exponential decrease in the mixing ratio, as given by the formula at the bottom of Table 4-1, is assumed.

The data of Table 4-1 apply to all latitudes and longitudes and to all diurnal conditions.

Table 4-1. Composition data for methane at selected altitudes.

z km	m_R ppmv	m_R ppmm	Molecules per m^3	Ref.	z km	m_R ppmm	Molecules per m^3	Ref.
0	1.4	0.77		DT-75	65	1.34(-2)	8.29(13)	Hu-73a
5	1.4	0.77			70	8.36(-3)	2.59(13)	
10	1.4	0.77			75	4.80(-3)	7.20(12)	
15		0.66	4.84(18)		80	2.69(-3)	1.85(12)	
20		0.61	2.06(18)		85	1.84(-3)	5.18(11)	
25		0.53	8.20(17)		90	1.02(-3)	1.17(11)	
30		0.50	3.55(17)		95	8.77(-4)	3.98(10)	
35		0.38	1.26(16)		100	7.03(-4)	1.34(10)	
40		0.31	4.84(16)		105	5.70(-4)	4.67(9)	
45		0.24	1.69(16)		110	4.40(-4)	1.69(9)	
50		0.11	3.43(15)	DT-75	115	2.55(-4)	4.54(8)	
55		4.76(-2)		Interp.	120	1.06(-4)	1.00(8)	Hu-73a
60		2.12(-2)	2.52(14)	Hu-73a	120	a		

[a] $m_R = m_R(120)\ \exp[-0.176(z-120)]$, $z > 120$ km.

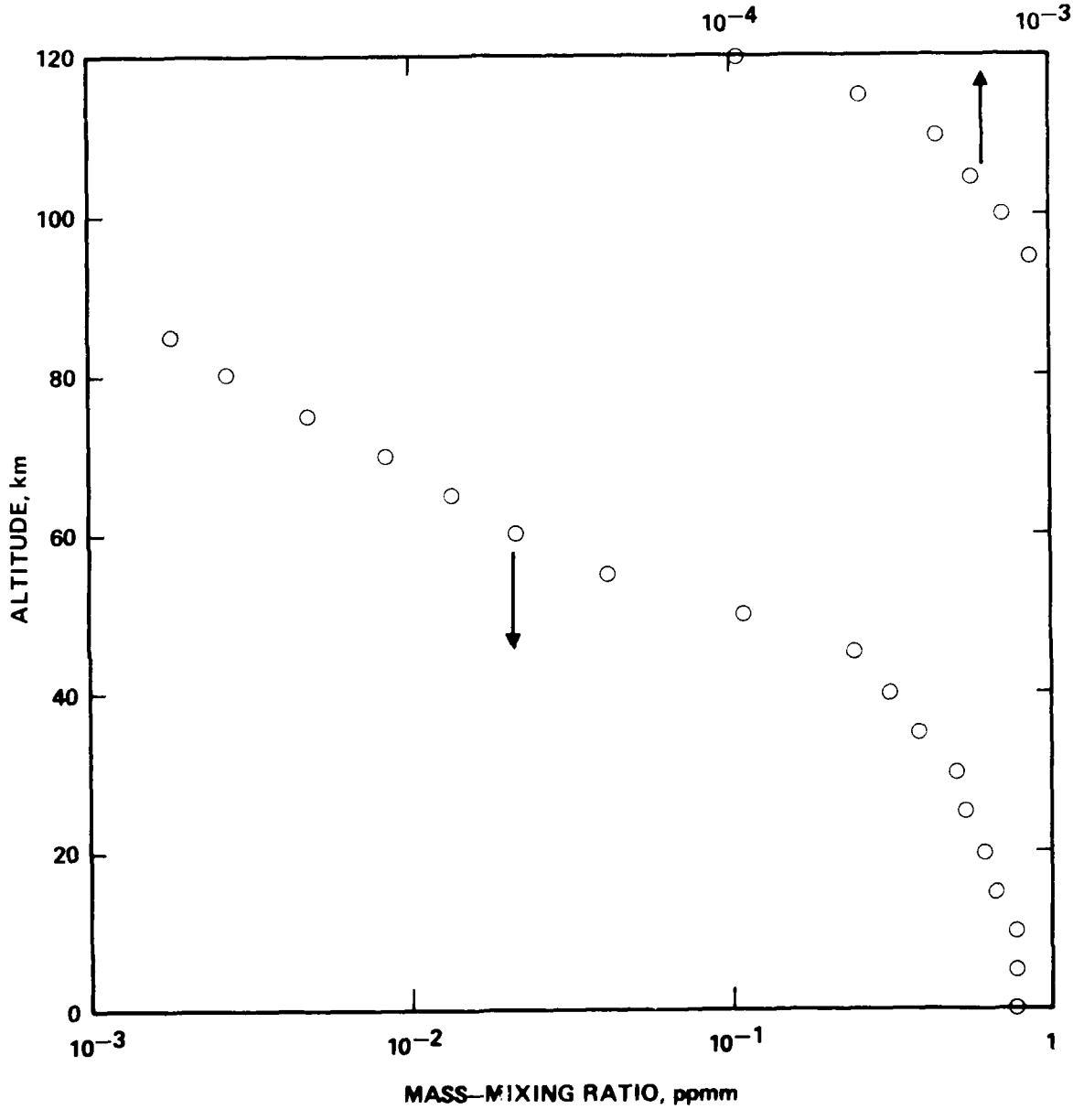

Figure 4-1. Vertical profile of the methane mass-mixing ratio.

SECTION 5

A MASS-MIXING RATIO PROFILE FOR CARBON MONOXIDE

5-1 INTRODUCTION

From measurements of the carbon monoxide mixing ratio of the atmosphere [SJ-70, EH-74, FR-74, EH-75, DT-75, WW-76], the mixing ratio profile can be deduced up to about 80 km. Above about 80 km, the profile deduced from the experimental observations [WW-76] is not unique but is in reasonable agreement with model calculations [HO-70, WM-72, Hu-73a] and, in the absence of the experimental data, can be justifiably used as the carbon monoxide profile.

In the stratosphere, there is evidence for variation of the mixing ratio with latitude [FR-74]; this variation is not incorporated into the present model as the supporting data are too limited.

5-2 THE CARBON MONOXIDE PROFILE

The data on carbon monoxide mass-mixing ratios are presented in Table 5-1 and shown in Figure 5-1.

In the troposphere, the volume-mixing ratio, ppmv, lies between 0.1 and 0.15 [SJ-70]. Near the earth's surface or over oceans the mixing ratio values may be significantly larger or smaller than the limits of the range given. For the present model, a mean value of the mixing ratio has been chosen.

In the stratosphere, the selected data of Table 5-1 are based on a collation [EH-74] plus later reports [FR-74, EH-75] from which an estimated profile of the mixing ratio between 8 and 45 km was chosen.

In the mesosphere, the data of Table 5-1 are from ground-based microwave measurements for the altitude range from 45 to 80 km.

Above 80 km, the experimental data do not lead to a unique mixing ratio profile [WW-76]. Comparison of the profile derived from the experimental data with model calculations [HO-70, WM-72, Hu-73a] shows (a) good agreement in the range from 120 to 150 km and (b) good

Table 5-1. Mass-mixing ratios of carbon monoxide.

z km	m_R ppmm	Ref.	z km	m_R ppmm	Ref.	z km	m_R ppmm	Ref.
0	0.12	SJ-70	55	0.127	WW-76	110	32.0	WW-76
5	0.12	SJ-70	60	0.254	↓	115	32.6	↓
10	0.11	EH-74[a]	65	0.442	↓	120	33.6	↓
15	0.072	↓	70	0.967	↓	125	34.4	↓
20	0.054	↓	75	2.21	↓	130	34.8	↓
25	0.048	↓	80	10.2	↓	135	34.8	↓
30	0.048	↓	85	18.5	↓	140	34.8	↓
35	0.048	↓	90	24.3	↓	145	34.5	↓
40	0.048	EH-74[a]	95	26.6	↓	150	34.1	WW-76
45	0.056	WW-76	100	29.2	↓	150	b	HO-70
50	0.070	WW-76	105	30.9	WW-76			

[a] The values listed here represent an estimated mean curve from the data collated in EH-74.

[b] $m_R = m_R(150)\ \exp[-0.0047(z-150)]$.
The calculations of HO-70 above 150 km were used to obtain the slope $\partial m_R/\partial z$ used in the equation.

agreement with one of the calculations [HO-70] in the range from 80 to 120 km. In the range from 80 to 150 km, the experimentally derived values of the mixing ratio are chosen, as these provide the smoothest transition of the mixing ratio profile between 80 and 120 km and are at least as likely to be as correct as any of the model calculations.

Above 150 km, an exponential decrease in the mass-mixing ratio is assumed, as shown at the bottom of Table 5-1.

The data of Table 5-1 apply at all latitudes and longitudes and for all diurnal conditions.

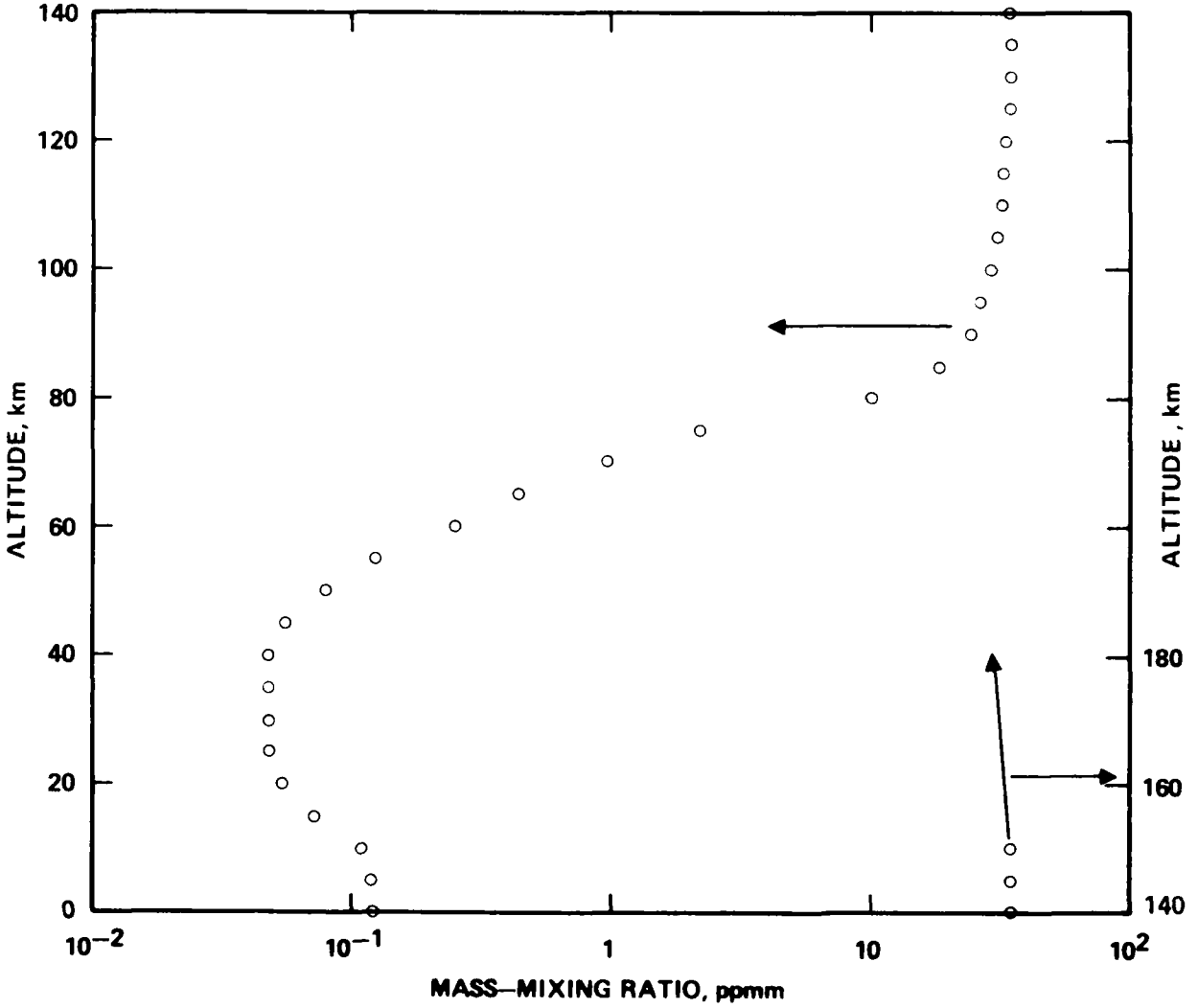

Figure 5-1. Vertical profile of the carbon monoxide mass-mixing ratio.

SECTION 6

A DENSITY PROFILE FOR HYDROXYL RADICAL

6-1 INTRODUCTION

Only a few measurements of the hydroxyl radical density have been made [DH-76, PE-76, WD-75, An-71d, An-76, Bu-76]. The measurements have been made between ground and 70 km so that, while few in number, they provide an important guide to density values in this range of altitudes.

The significance of measurements in the troposphere [DH-76, PE-76, WD-75] is not yet clear. It has been argued on the basis of (a) atmospheric halocarbon data [Si-77], (b) the latitudinal distribution of CO mixing ratios, and (c) the rate of nitrate precipitation in the northern hemisphere [Wa-74] that the number density of hydroxyl radicals in the troposphere is typically 5×10^5 cm^{-3} whereas measurements yield values roughly ten times larger. Two of the measurements [PE-76, WD-75] were ground based and are probably influenced by urban and industrial emissions [DH-76]; the other measurements [DH-76] were made at altitudes of 7 and 11.5 km but at the low latitudes of 21° and 32°N. Calculations which assume a high tropopause – 16 km, say, as found at lower latitudes – yield a significantly greater concentration of hydroxyl radicals at and near 10 km than do calculations which assume a tropopause at 10 km. Thus, both arguments and measurements could be correct if applied only over specific geographical locations.

There have been many calculations of the vertical profile of hydroxyl radical. Recent calculations have been summarized in DT-75 and SW-76; also see WT-74, TB-72, BT-73a, and Hu-73a. There is a considerable scatter in the predictions of the models, of the order of a factor of 10. The general trends of the model profiles are similar [DT-75]. Model calculations show a significant diurnal variation in hydroxyl radical density up to about 80 km [WT-74, Hu-73a, TB-72].

The profiles presented below include the diurnal variation in hydroxyl radical densities but not geographical variations; there are essentially no data indicating the latter variations but they are likely to be large.

6-2 THE HYDROXYL RADICAL PROFILE

The experimental data and the results of calculations for daytime are shown in Figure 6-1. The experimental data at ground level [PE-76] are shown only by an upper limit. The data at 7 and 11.5 km have been discussed above. The experimental data between 30 and 70 km lack consistency which makes the profile selection difficult. The calculated densities are not in agreement generally with the experimental data. Of the many model calculations, all but one fall in Region 1 as indicated in Figure 6-1; the exception determines the boundary of Region 2.

The estimated daytime profile data as shown in Table 6-1 and Figure 6-2 are an arbitrary compromise among the data shown in Figure 6-1. In the troposphere the estimate represents a compromise between the data shown in Figure 6-1 and the arguments for lower concentrations discussed above [Si-77, Wa-74].

To obtain a midnight hydroxyl radical profile, the daytime profile data given in Table 6-1 are divided by the ratio of the noon- to midnight-hydroxyl radical density; the latter are shown in Figure 6-3 and are based on calculations [WT-74, Hu-73a]. Since the hydroxyl radical densities have a large uncertainty, the second-order variations in the ratios, as indicated by the data plotted in Figure 6-3, are ignored and a smooth curve (dashed in Figure 6-3) is drawn through the data to obtain the ratios over the range of altitudes up to 100 km. The midnight densities, calculated according to the above procedure, are listed in Table 6-1 and plotted in Figure 6-2.

Above 100 km, both the noon and midnight hydroxyl radical density profiles are allowed to decrease exponentially to a constant value of 10 cm^{-3}, in rough accord with the calculations of Hunt [Hu-73a] at altitudes above 100 km.

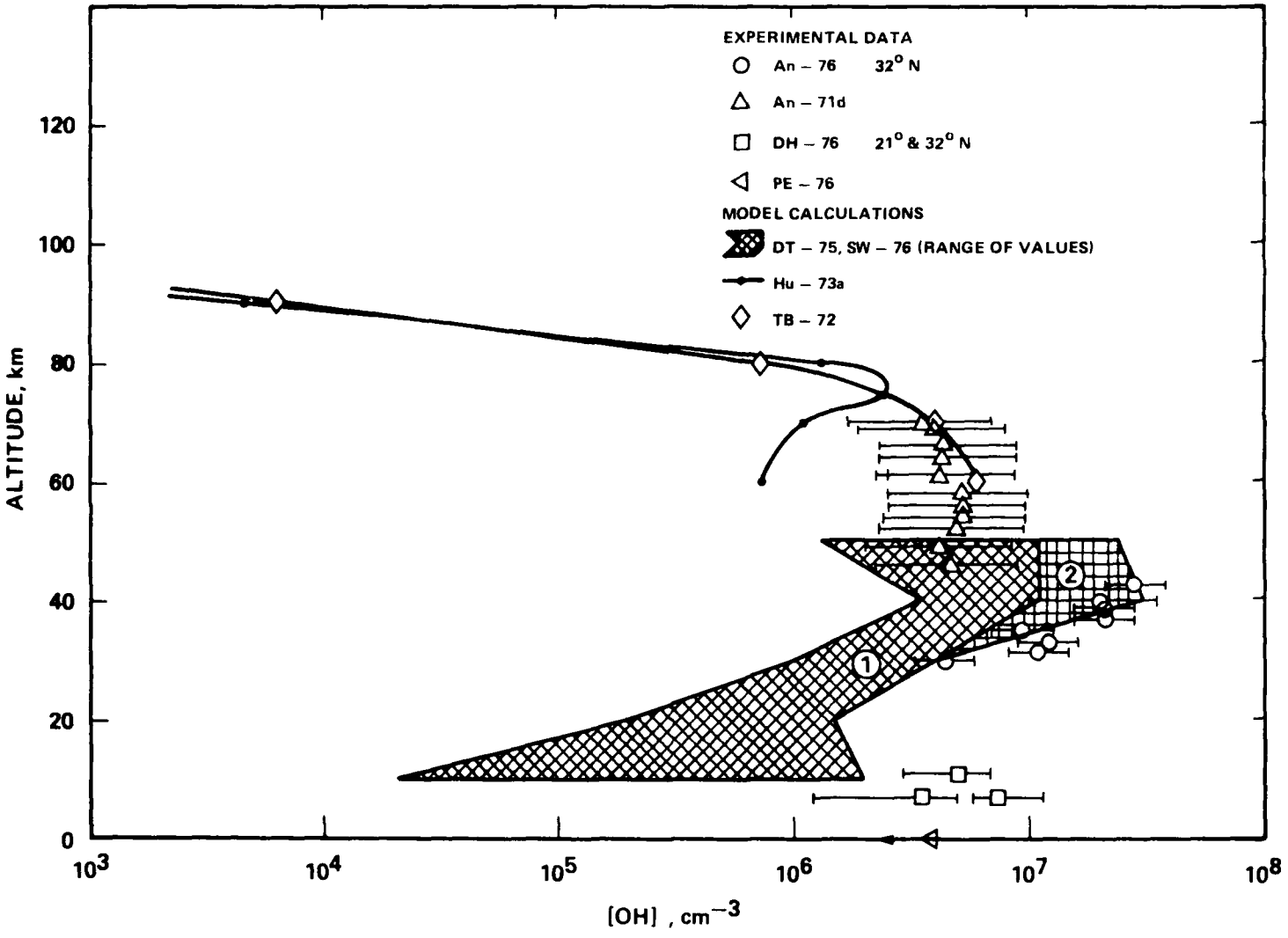

Figure 6-1. Measured and calculated daytime hydroxyl radical densities up to 90-km altitude.

Table 6-1. Hydroxyl radical densities for noon and midnight conditions.

z km	[OH], cm^{-3} Noon	[OH], cm^{-3} Midnight	z km	[OH], cm^{-3} Noon	[OH], cm^{-3} Midnight	z km	[OH], cm^{-3} Noon	[OH], cm^{-3} Midnight
0	1.0(6)	1.7(2)	40	1.05(7)	5.7(4)	80	7.0(5)	1.6(6)
5	1.0(6)	1.8(2)	45	1.1 (7)	2.9(5)	85	7.0(4)	1.7(5)
10	1.05(6)	2.1(2)	50	9.5 (6)	1.2(6)	90	6.3(3)	1.7(4)
15	1.15(6)	2.7(2)	55	7.2 (6)	4.4(6)	95	5.7(2)	1.7(3)
20	1.5 (6)	4.2(2)	60	5.3 (6)	6.5(6)	100	6.7(1)	2.2(2)
25	2.3 (6)	8.1(2)	65	3.7 (6)	5.9(6)	>100	a	a
30	4.0 (6)	2.0(3)	70	2.5 (6)	4.5(6)			
35	6.8 (6)	8.0(3)	75	1.6 (6)	3.2(6)			

[a] $[OH]_{z>100} = 10 + 2\{[OH]_{z=100} - 10\}/\{1 + \exp[0.46(z-100)]\}$.

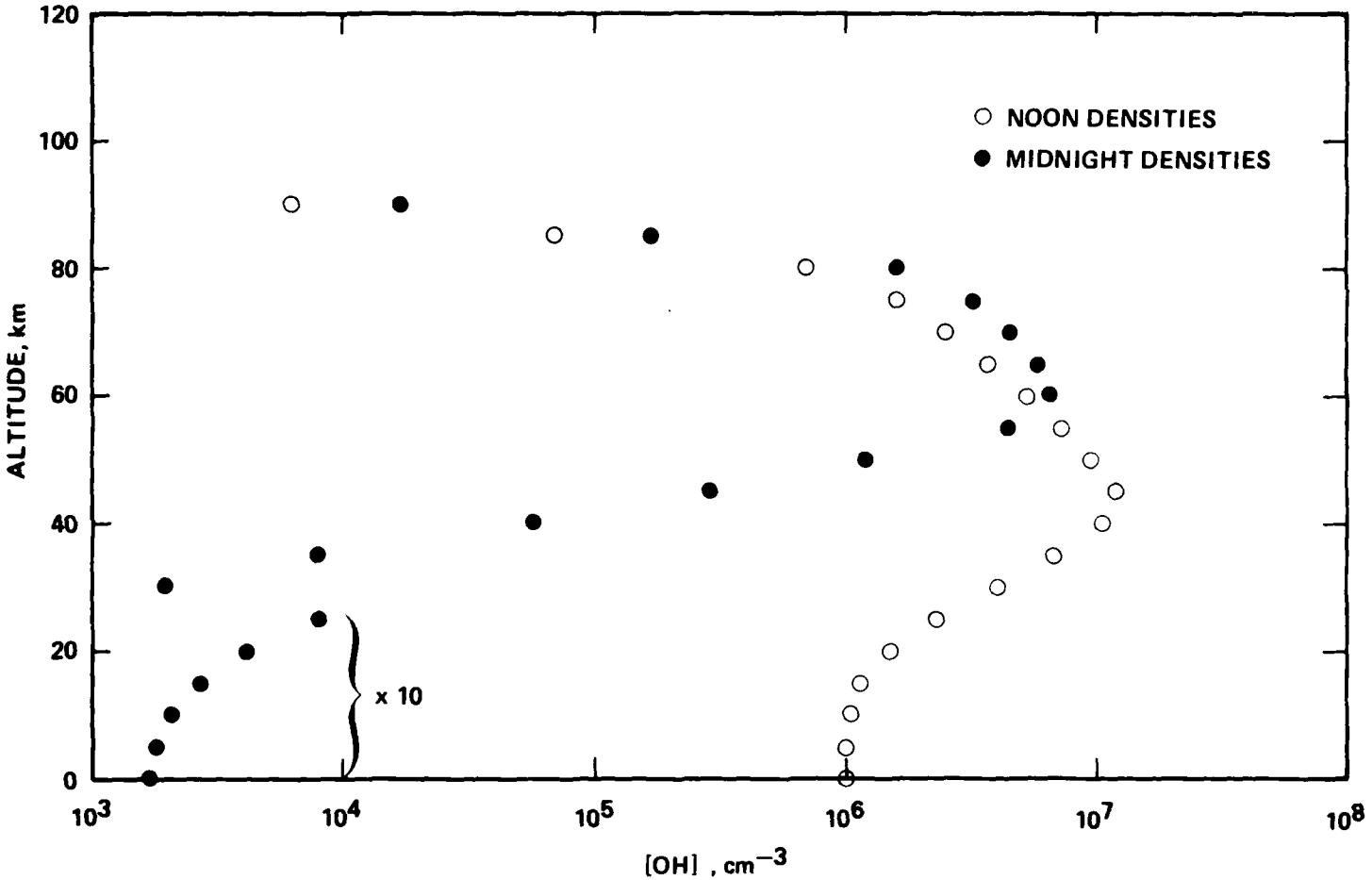

Figure 6-2. Selected hydroxyl radical densities up to 90-km altitude.

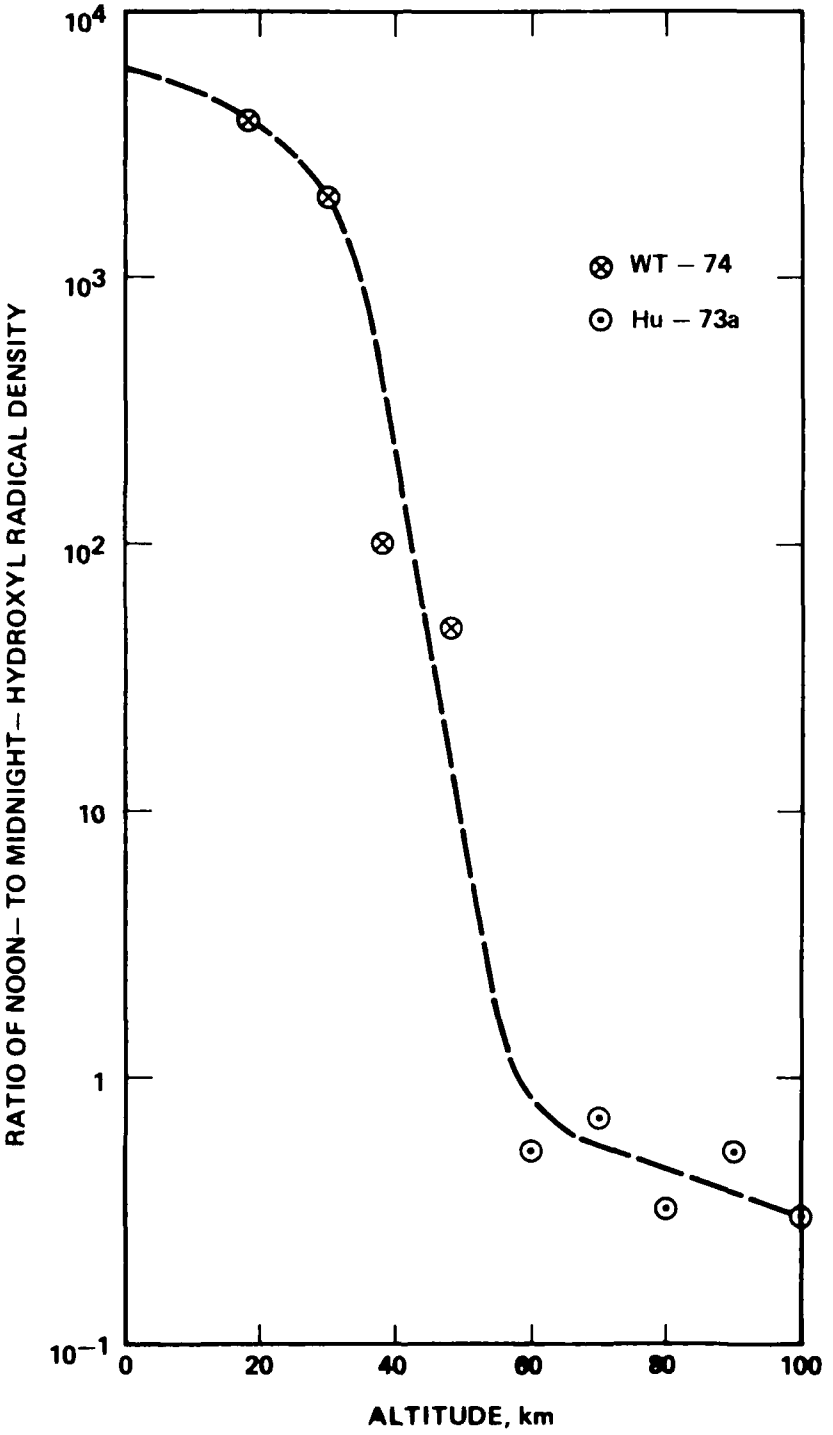

Figure 6-3. Ratio of noon- to midnight-hydroxyl radical density.

SECTION 7

A DENSITY PROFILE FOR HYDROPEROXYL RADICAL

7-1 INTRODUCTION

There are apparently no measurements of the hydroperoxyl radical density in the earth's atmosphere. Hence, the density profile selected below is based entirely on model calculations. The model calculations have been summarized in DT-75 and SW-76; also see WT-74 and Hu-73a.

7-2 THE HYDROPEROXYL RADICAL PROFILE

The data selected from the model calculations for noon conditions are listed in Table 7-1 and plotted in Figure 7-1. Between 0 and 10 km, the data are obtained by extrapolation of an estimated mean curve through the results of model calculations at higher altitudes. Between 10 and 50 km, the data represent an estimated mean of model calculations [DT-75, SW-76]. At 55 km, the datum is obtained by interpolation. For 60 km and above, the data are from a model calculation [Hu-73a].

A diurnal variation is found in the model calculations. To obtain a midnight hydroperoxyl radical profile, the noon profile given in Table 7-1 is divided by the ratio of the noon- to midnight-hydroperoxyl radical density; the latter are shown in Figure 7-2 and are taken from WT-74 and Hu-73a. Since the hydroperoxyl radical densities have a large uncertainty, the second-order variations in the ratios, as indicated by the data plotted in Figure 7-2, are ignored and a smooth curve (dashed in Figure 7-2) is drawn through the data to obtain the ratios over the range of altitudes up to 100 km. The midnight densities, calculated according to the above procedure, are listed in Table 7-1 and plotted in Figure 7-1.

Above 100 km, the hydroperoxyl radical densities are calculated as indicated in Table 7-1.

Table 7-1. Hydroperoxyl radical densities for noon and midnight conditions.

z km	$[HO_2]$, cm^{-3}		z km	$[HO_2]$, cm^{-3}		z km	$[HO_2]$, cm^{-3}	
	Noon	Midnight		Noon	Midnight		Noon	Midnight
0	1.0(5)	4.9(1)	40	1.2(7)	1.3(5)	80	9.2(6)	9.2(6)
5	7.5(5)	4.2(2)	45	9.1(6)	2.4(5)	85	5.7(4)	5.7(4)
10	2.4(6)	1.6(3)	50	6.6(6)	4.6(5)	90	5.7(3)	5.7(3)
15	6.9(6)	5.9(3)	55	4.2(6)	6.9(5)	95	4.9(2)	4.9(2)
20	1.15(7)	1.4(4)	60	2.2(6)	7.3(5)	100	7.4(1)	7.4(1)
25	1.5(7)	2.7(4)	65	7.9(5)	4.6(5)	>100	a	a
30	1.6(7)	4.7(4)	70	4.2(6)	3.5(6)			
35	1.5(7)	8.3(4)	75	1.2(7)	1.2(7)			

[a] $[HO_2]_{z>100} = [HO_2]_{100} \exp[-0.378(z-100)]$.

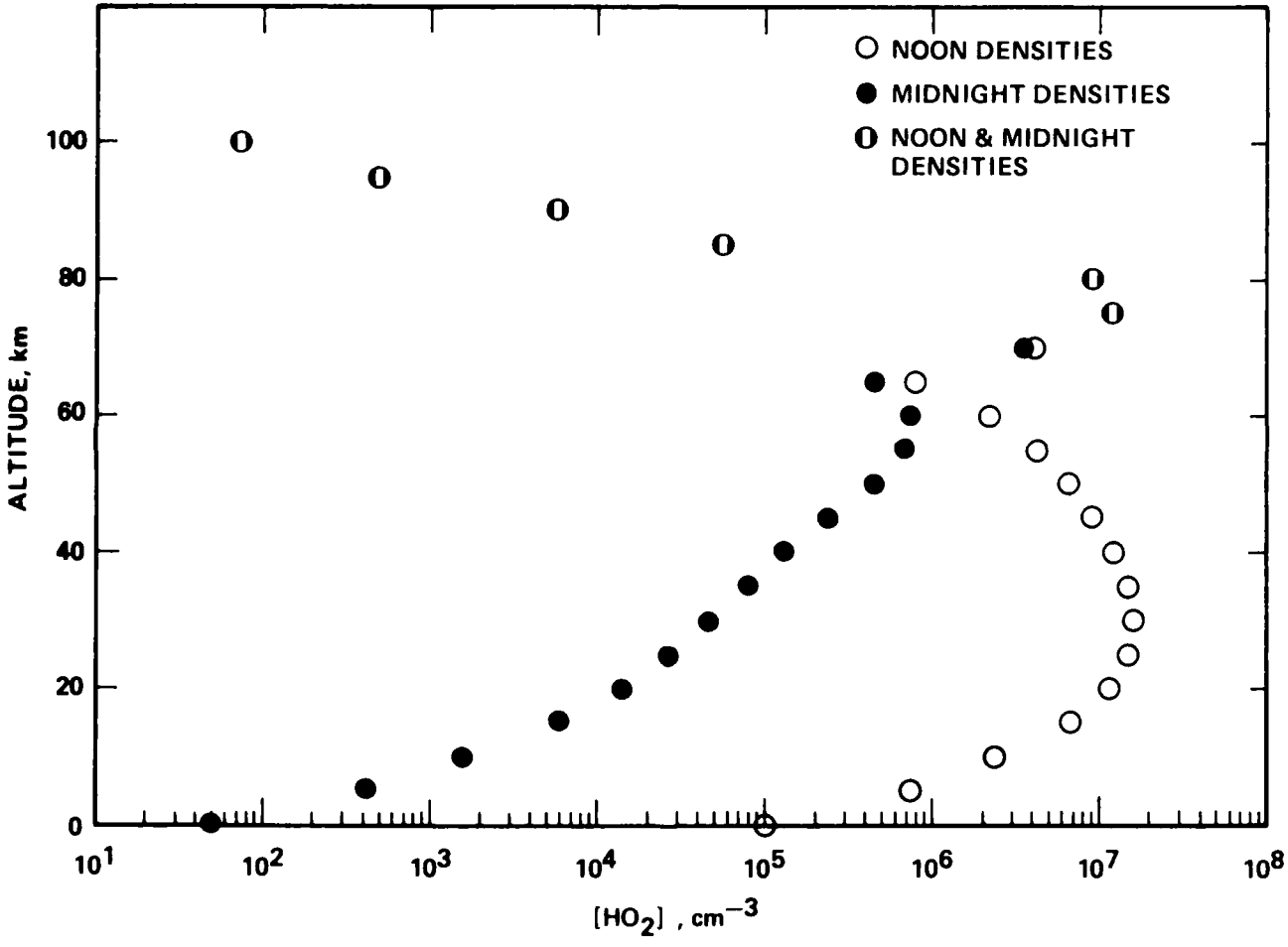

Figure 7-1. Selected hydroperoxyl radical densities up to 100-km altitude.

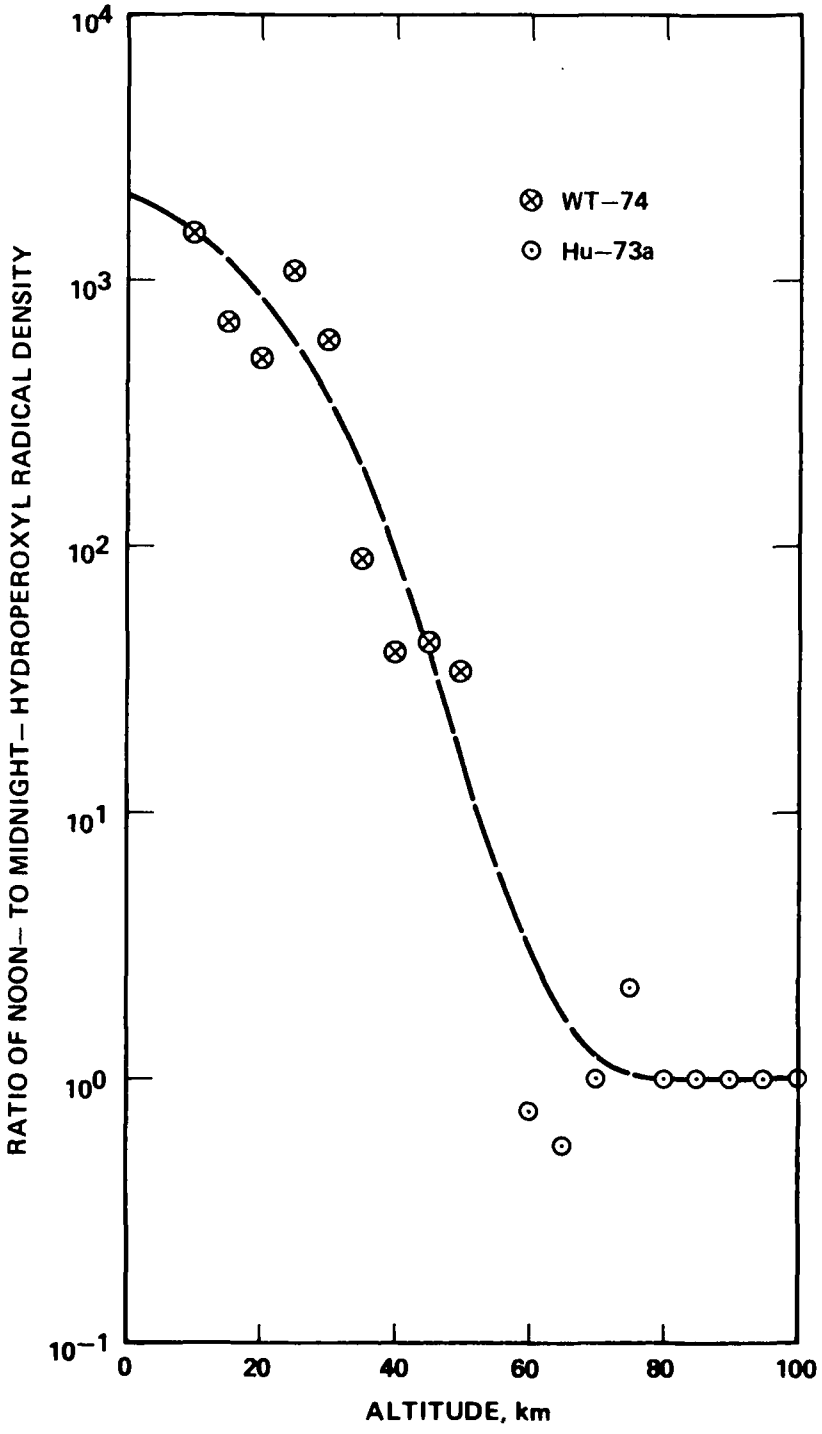

Figure 7-2. Ratio of noon- to midnight-hydroperoxyl radical density.

SECTION 8

A DENSITY PROFILE FOR HYDROGEN ATOMS

8-1 INTRODUCTION

A moderate number of indirect measurements of the hydrogen atom density above 100 km have been made; of particular use in the present effort are the densities deduced from satellite measurements [MM-73, MM-70c, MW-70b, Me-70a, Me-69a] of the Lyman-alpha airglow. Density profiles have been deduced with the aid of a combination of models of Kockarts and Nicolet and of Chamberlain, normalized to a specific density at 100 km so as to obtain agreement with the observations. The airglow measurements [MM-73] show a diurnal variation in hydrogen atom density above 100 km by a factor of about 1.7. However, in deriving a hydrogen atom profile for noon and midnight conditions in this report, we neglect this diurnal variation.

For altitudes below 100 km, there are several model calculations [SW-76, HS-74a, LD-74, LD-74a, LD-74b, Hu-73a, TB-72] and a profile of hydrogen atom densities based on observations [EL-73]. For those model calculations concerned with diurnal variations, a strong effect is found below about 85 km and this is included in the profiles derived here. Other model calculations [HS-74a, LD-74, LD-74a, LD-74b] focus on the flux of hydrogen atoms escaping from the earth's atmosphere and on the relation between the escape flux and the hydrogen mixing ratio in the stratosphere. Certain of the models [HS-74a, LD-74] require mixing ratio contributions from stratospheric water, the amounts of which are in good accord with the H_2O model presented in Section 2. In other model studies [LD-74a, LD-74b] the acceptance of generally discredited data on H_2O mixing ratios in the stratosphere forces a search for mechanisms of hydrogen atom escape other than the normal hydrogen atom upward flux.

The experimentally-based hydrogen atom profiles in the mesosphere [EL-73] are derived from simultaneous measurements of fluorescence from $O_2(^1\Delta_g)$ and vibrationally excited OH and the assumed

kinetics of O_3 photalysis, O_3 formation, the $H + O_3$ reaction, and quenching of some of the involved species. The expected quenching of OH by O was not accounted for in view of certain atmospheric observations [EL-73]; should this prove to be an incorrect procedure, the hydrogen profile would require revision.

8-2 THE HYDROGEN ATOM PROFILE

The densities derived from the model calculations and observations are shown in Figure 8-1. The model calculations are shown for altitudes only up to 100 km since, for higher altitudes, reliance is placed on the densities derived from observations.

The normalization of the hydrogen atom density to 3×10^7 cm^{-3} at 100 km is consistent with the observations [MM-70c]. A somewhat more refined normalization has been adopted in the independent observations of the solar Lyman-alpha airglow [VB-73]; this normalization ranges from 2.5×10^7 cm^{-3} at low solar activity to 4×10^7 cm^{-3} at high solar activity.

Between 40- and 100-km altitude, the selected hydrogen atom profile represents a compromise among the various model calculations and the experimentally-based data. Between 70 and 100 km, only the model calculations which are formulated with regard to agreement on the hydrogen atom escape flux have been considered in the profile selection.

The selected data for the hydrogen atom densities are listed in Table 8-1 and shown in Figure 8-2 for altitudes between 10 and 140 km and in Figure 8-3 for altitudes between 100 and 1000 km. Above 100-km altitude, the selected profile is represented by the analytical fit function presented in Table 8-1. This fit function applies to hydrogen atom densities which obtain for an exospheric temperature of 1100°C. A recent observation [LM-76] has led to a value of $[H] = 9.2 \times 10^4$ cm^{-3} at 650 km for an exospheric temperature of 950°K. This value would correspond to about 4.4×10^4 cm^{-3} for an exospheric temperature of 1100°K (based on the variation of hydrogen atom density with exospheric temperature shown in Figure 3 of Me-69a) compared with the value 3.9×10^4 cm^{-3} for the profile selected here.

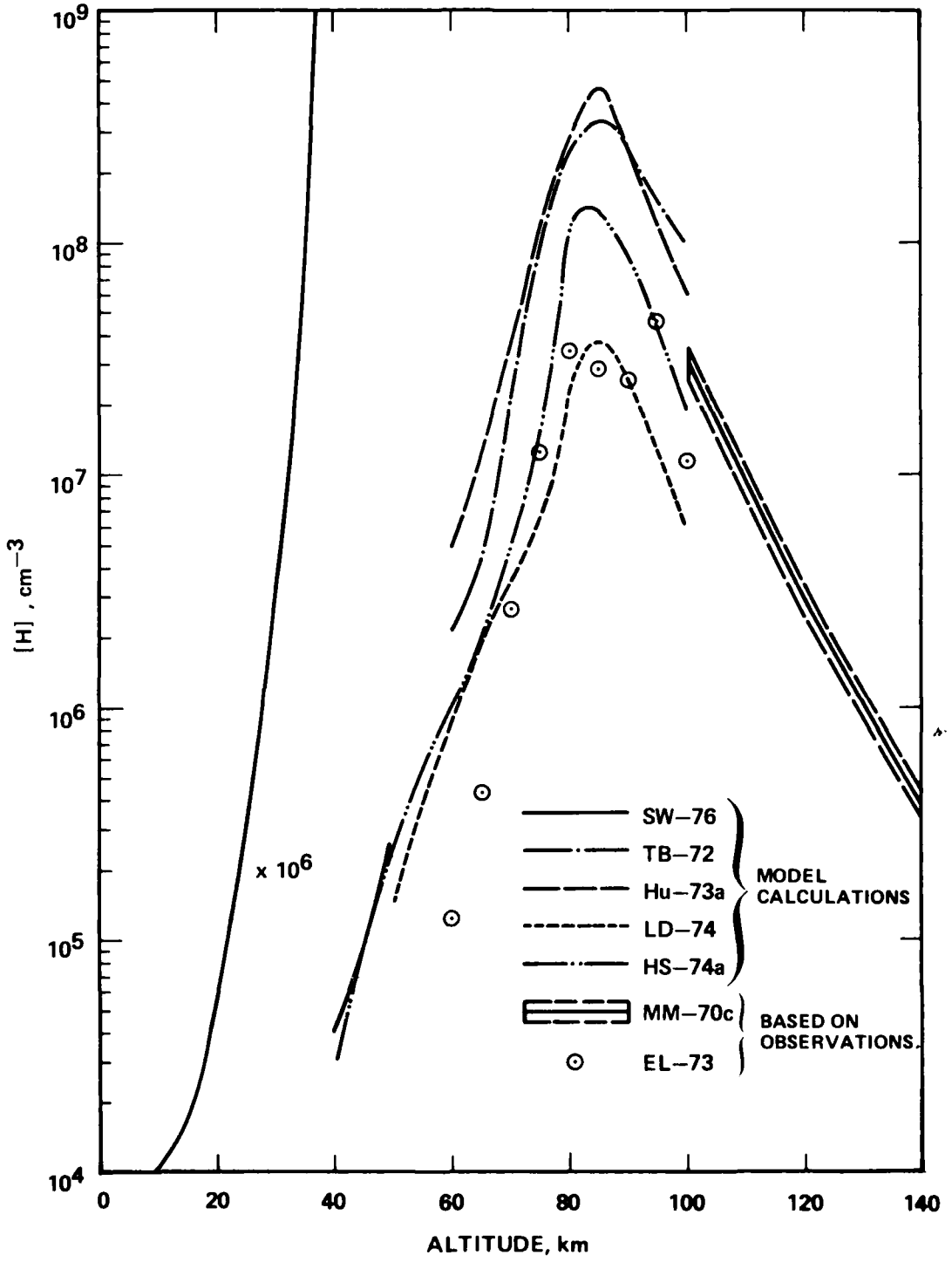

Figure 8-1. Measured and calculated hydrogen atom density between 10- and 140-km altitude.

Table 8-1. Hydrogen atom densities for noon and midnight conditions.

z km	[H], cm^{-3} Noon	Midnight	z km	[H], cm^{-3} Noon	Midnight	z km	[H], cm^{-3} Noon	Midnight
0	7.0(-3)	0	40	4.0(4)	0	80	3.5(7)	1.0(7)
5	7.6(-3)	↓	45	1.0(5)	↓	85	8.6(7)	8.6(7)
10	1.0(-2)	↓	50	2.4(5)	↓	90	7.4(7)	7.4(7)
15	1.6(-2)	↓	55	5.1(5)	↓	95	5.0(7)	5.0(7)
20	5.2(-2)	↓	60	1.0(6)	↓	100	3.0(7)	3.0(7)
25	3.2(-1)	↓	65	1.8(6)	↓	>100	a	a
30	2.9(0)	↓	70	4.9(6)	0			
35	1.0(2)	0	75	1.25(7)	5.0(2)			

[a] $[H] = 3.77 \times 10^{12} \exp(-0.1174z) + 4.07 \times 10^{6}/z^{0.7169}$, cm^{-3}.

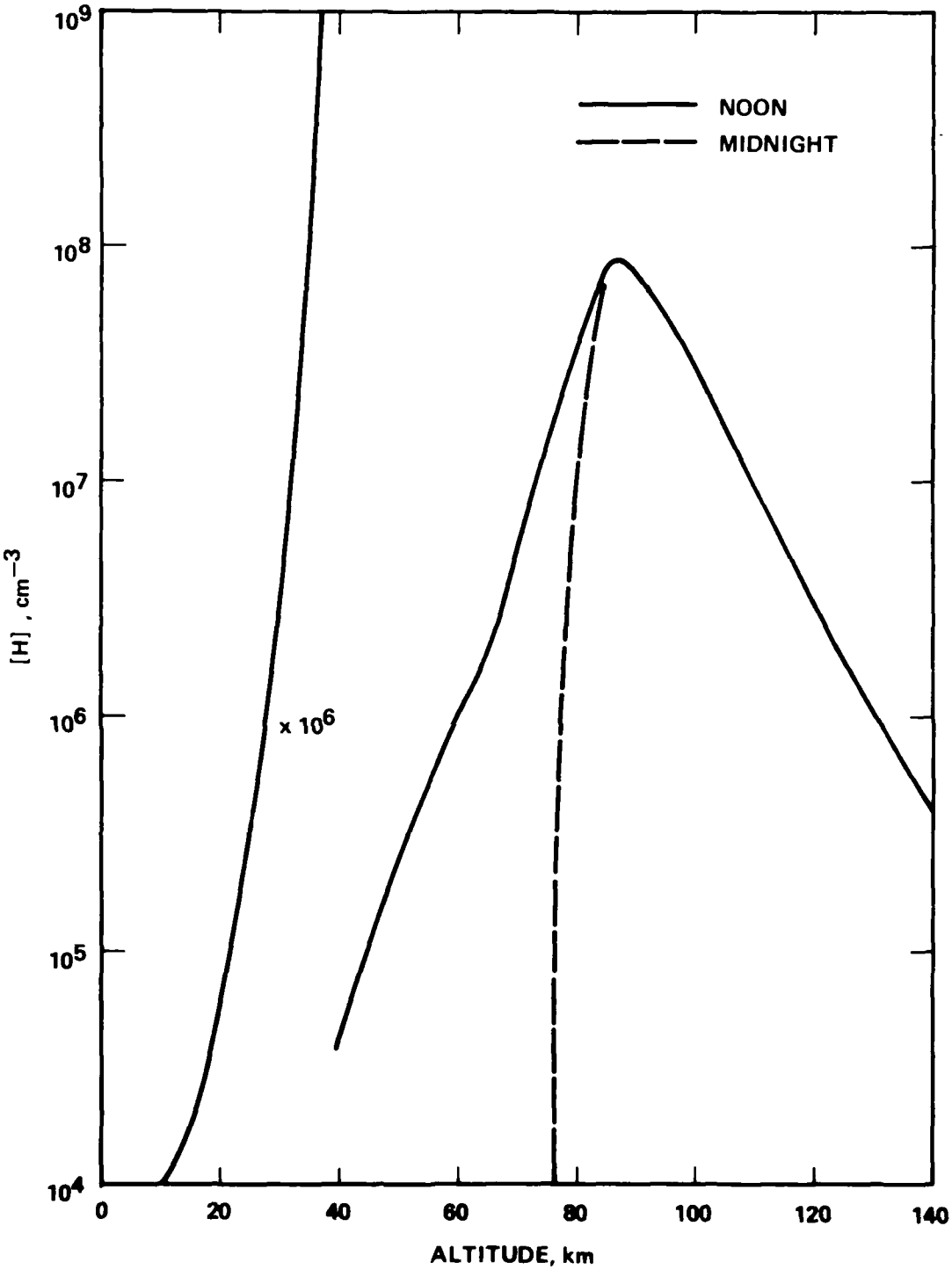

Figure 8-2. Selected hydrogen atom profile between 10- and 140-km altitude.

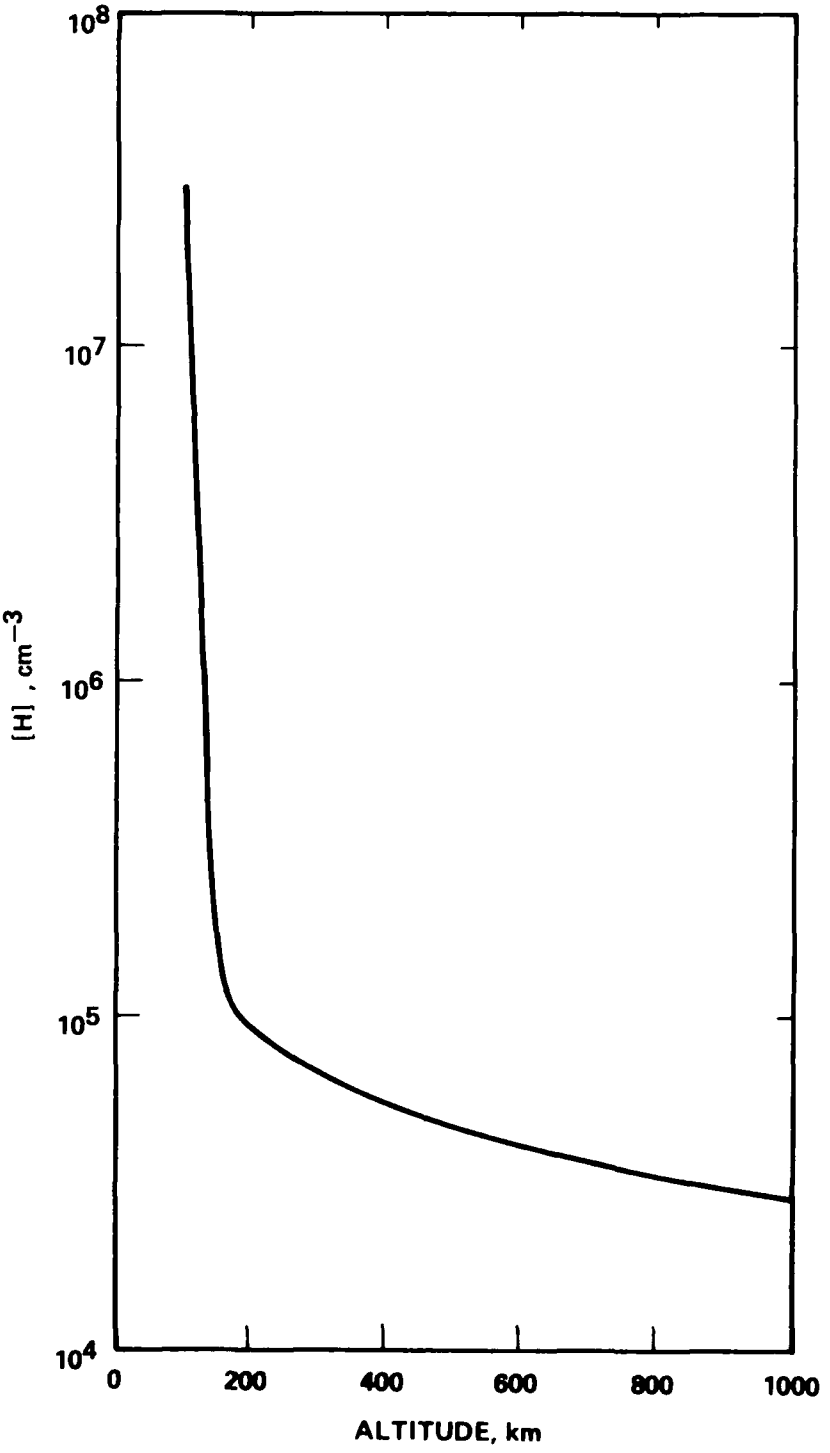

Figure 8-3. Selected hydrogen atom profile between 100- and 1000-km altitude.

SECTION 9

A DENSITY PROFILE FOR $O(^1D)$

There are apparently no measurements of $O(^1D)$ densities in the atmosphere. The profile derived here is based on model calculations. In the altitude range between 10 and 50 km, the various model calculations have been collated and compared [DT-75, SW-76]. From the available calculations, the one chosen here is the only one for an overhead sun [Ni-74]; this will represent the noon condition for the present profile. Between 60 and 160 km, the model calculations of Hunt [Hu-73a] are used. Above 160 km, the $O(^1D)$ density is assumed to decrease in proportion to the decrease of atomic oxygen [HS-78].

The data for the profile under noon conditions are listed in Table 9-1 and shown in Figure 9-1 for altitudes between 20 and 140 km. The $O(^1D)$ densities for midnight conditions are neglected [Hu-73a, SL-70a, SL-72].

Table 9-1. $O(^1D)$ densities for noon conditions.

z km	$[O(^1D)]$ cm^{-3}	Ref.	z km	$[O(^1D)]$ cm^{-3}	Ref.	z km	$[O(^1D)]$ cm^{-3}	Ref.
0	1.0(-2)		60	4.2(2)	b	120	6.4(3)	b
5	1.0(-2)		65	2.7(2)		125	6.4(3)	
10	1.0(-2)	a	70	4.6(1)		130	6.1(3)	
15	3.8(-1)		75	1.7(1)		135	5.8(3)	
20	2.4(0)		80	1.4(1)		140	5.5(3)	
25	1.1(1)		85	5.2(1)		145	5.5(3)	
30	3.9(1)		90	5.8(1)		150	5.3(3)	
35	1.4(2)		95	2.2(2)		155	5.2(3)	
40	3.5(2)		100	8.0(2)		160	5.1(3)	b
45	6.0(2)		105	2.0(3)		>160	c	
50	6.0(2)	a	110	3.9(3)				
55	5.0(2)		115	5.2(3)	b			

[a] DT-75, SW-76, and Ni-74 ($\chi = 0°$).

[b] Hu-73a.

[c] $[O(^1D)] = \{[O(^1D)]/[O]\}_{160}\ [O]_{z>160}$.

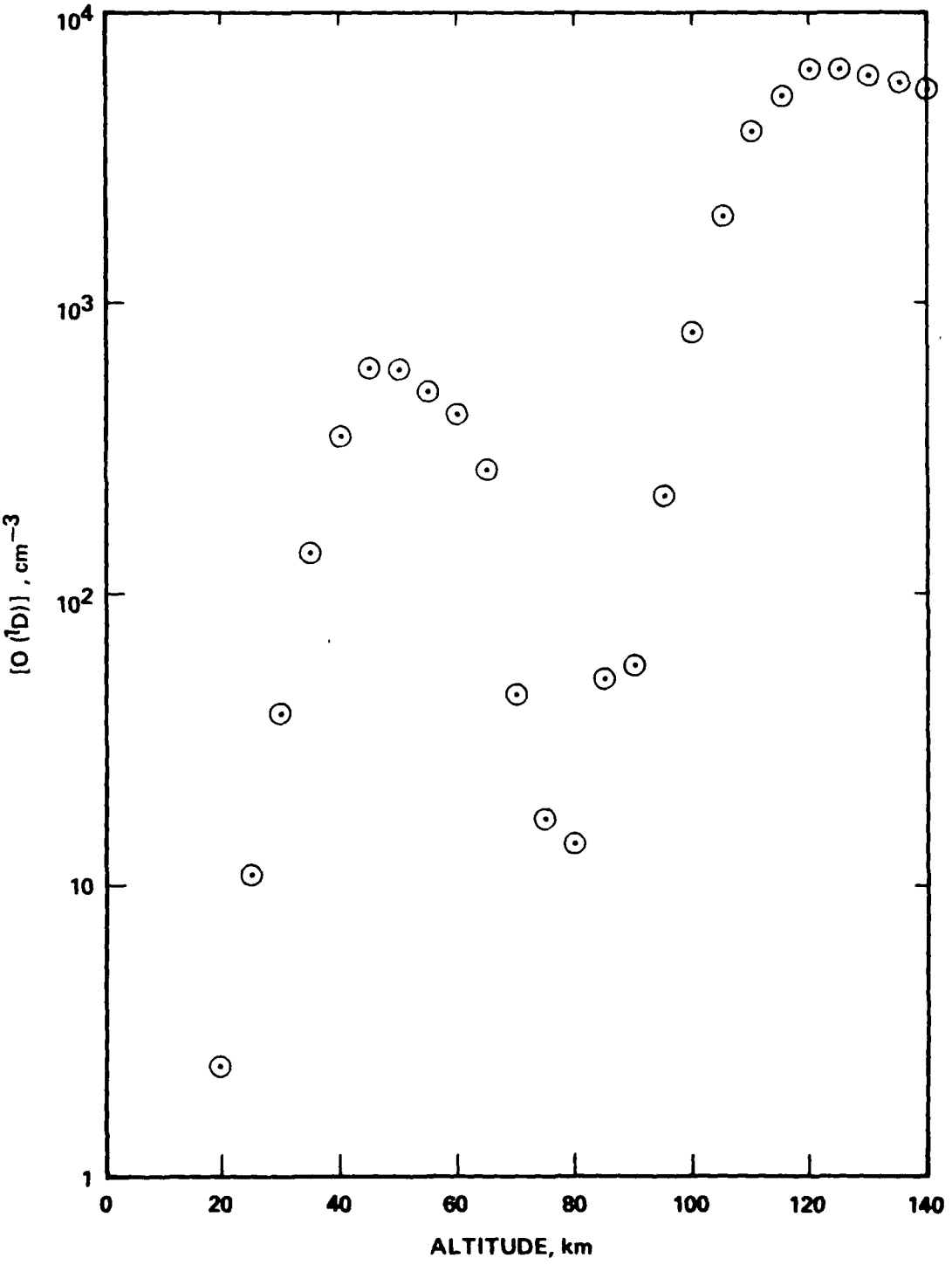

Figure 9-1. Selected O(^{1}D) profile between 20- and 140-km altitude.

SECTION 10

A VOLUME-MIXING RATIO PROFILE FOR NITROUS OXIDE

10-1 INTRODUCTION

A large number of measurements of nitrous oxide have been made up to about 30-km altitude [SA-77, FR-74, EH-75, EH-74, Go-69c, SJ-70a, HB-74a, MG-73b, RK-76] and a few up to about 60 km [EH-75]. These measurements are roughly in accord but indicate a latitudinal dependence. A few calculations have been made [SL-70a, SL-72, Cr-74a, Vu-75, ME-76] but mainly for stratospheric altitudes. The calculations indicate a latitudinal [Vu-75, ME-76] and seasonal [Vu-75] dependence.

A profile is obtained here based on the experimental data up to about 60 km and at higher altitudes it is based on the assumption of a constant mixing ratio. A latitudinal dependence is incorporated into the model profile.

10-2 THE NITROUS OXIDE PROFILE

Experimental data on the volume-mixing ratio, ppbv, are listed in Table 10-1 for altitudes up to 62 km. These data are plotted in Figure 10-1 except for that at latitudes of 9° and 51°N which are discussed below. The data at high altitudes ($z \gtrsim 40$ km) [EH-75] were obtained over a range of altitudes (see Table 10-1). These data are plotted in Figure 10-1 at an altitude at which the mean volume-mixing ratio would be found if the volume-mixing ratio were a function of altitude according to the expression

$$m_R(z) = m_o e^{-z/z_o} \qquad (1)$$

where $m_R(z)$ is the mixing ratio at altitude z. For these data [EH-75] the vertical bars in Figure 10-1 represent the range of altitudes for the measurements and the horizontal bars represent the uncertainties in the volume-mixing ratios.

Table 10-1. Data on the volume-mixing ratio of N_2O between 0 and 62 km.

z km	m_R ppbv[a]	z km	m_R ppbv	z km	m_R ppbv	z km	m_R ppbv	Latitude	Longitude	Ref.	Symbol
27.0	1.2(2)	20.7	1.9(2)	15.4	3.0(2)	27.1	1.0(2)	41°N	105°W	SA-77[c]	○
25.0	1.6(2)	16.6	3.2(2)	10.1	3.1(2)	26.4	1.6(2)				
21.4	2.2(2)	11.9	3.5(2)	21.9	1.4(2)	22.8	2.3(2)				
11.4	3.3(2)	24.6	1.3(2)	7.9	3.4(2)	17.7	3.0(2)				
24.3	1.4(2)	23.0	1.7(2)	17.2	2.5(2)						
23.2	1.5(2)	20.0	2.6(2)	15.8	2.7(2)						
36.4	3.0(1)	15.6	3.2(2)	24.5	1.2(2)			63°N	147°W	SA-77	△
22.3	3.6(1)	7.6	3.4(2)	20.0	2.1(2)						
30.8	8.0(1)	27.9	4.6(1)	10.0	3.5(2)						
32.1	2.0(2)	22.7	2.6(2)	17.1	3.4(2)			9°N	79°W	SA-77	(d)
27.8	2.3(2)	18.5	3.0(2)								
22.2	1.5(2)	16.8	3.0(2)					32°N	106°W	SA-77	□
25.6	3.5(1)	17.9	1.2(2)	10.0	2.8(2)			51°N	102°W	SA-77	(d)
22.0	6.2(1)	13.6	2.8(2)								
2.9	3.0(2)	2.0	3.0(2)	2.9	3.3(2)	1.8	3.3(2)	40°N	105°W	SA-77	x
25.4	6.8(1)	24.5	9.0(1)	23.0	1.2(2)	14.4	2.8(2)	78°S	167°E	SA-77	◇
25.3	7.5(1)	24.3	9.4(1)	20.2	1.6(2)						
25.0	7.9(1)	23.3	1.1(2)	17.9	2.1(2)						
11-16	3.3(2) -3.6(2)							30°-76°N	-	FR-74	▯
40.8-50.6	3.0(0)	43.6-62.3	3.0(-1)					32°N	106°W	EH-75	○
31.3	7.4(1)	20.0	2.5(2)	10.7	2.6(2)	4.0	2.8(2)	31.5°N	95°W	EH-74[c]	○
29.5	1.4(2)	18.0	2.9(2)	8.9	2.4(2)	2.7	3.0(2)				
27.4	2.3(2)	16.9	3.2(2)	6.6	2.4(2)	1.5	3.3(2)				
26.2	2.3(2)	13.1	3.0(2)	5.7	2.4(2)	0.73	3.4(2)				
22.7	2.3(2)	11.9	3.0(2)	4.6	2.7(2)						

(Continued)

Table 10-1. (Cont'd)

z km	m_R ppbv	z km	m_R ppbv	z km	m_R ppbv	z km	m_R ppbv	Latitude	Longitude	Ref.	Symbol
7.8	2.8(2) -4.0(2)							42°N	71°W	Go-69c	
0.12	2.8(2)							50°N	8°E	SJ-70a[c]	
1.2	2.7(2)							48°N	7.5°E		
0.73	2.5(2)	1.78	2.4(2)	2.94	2.4(2)			47°N	11°E		
0.06	3.0(2)	2.36	3.0(2)	2.5	2.6(2)			28°N	16°W		
3.6	2.5(2)	9.8	2.5(2)	10.8	2.5(2)			26°S	28°E		
17.3	2.3(2)							52°N	7°E		
18.0	2.0(2)	23.0	1.0(2)					47°N	9°E		
10.0- 10.7	3.2(2)	12.1- 13.5	3.1(2)	15.0- 16.5	2.7(2)			65°-70°N	-	HB-74a[c]	
10.7- 12.1	3.1(2)	13.5- 15.0	2.9(2)								

[a] ppbv = parts per billion by volume.

[b] Symbol appears on Figure 10-1.

[c] Data listed for this reference were read from graphs.

[d] See text for discussion.

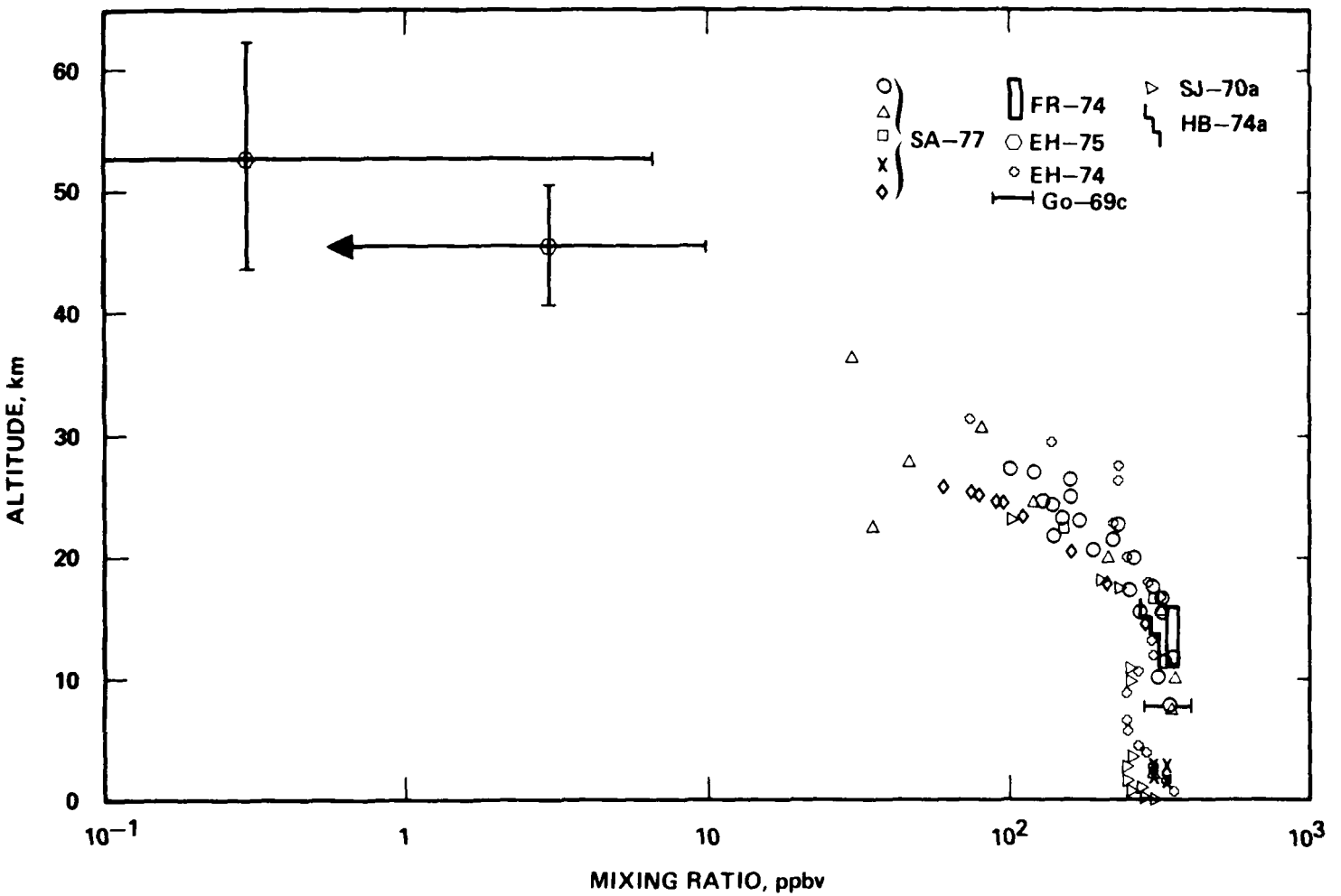

Figure 10-1. Data for N_2O volume-mixing ratio between 0 and 62 km.

From the data plotted in Figure 10-1, an estimated mean curve has been selected and this is shown in Figure 10-2 by the solid curve between 0- and 55-km altitude. The corresponding data are listed in Table 10-2 at 5-km intervals. The three additional sets of data also shown in Figure 10-2 are now discussed.

Table 10-2. Selected values of N_2O volume-mixing ratio.

z km	m_R ppbv	z km	m_R ppbv	z km	m_R ppbv	z km	m_R ppbv
0	3.1(2)	20	2.1(2)	40	9.4(0)	>55	1.3(-1)
5	2.6(2)	25	1.2(2)	45	2.9(0)		
10	2.8(2)	30	6.0(1)	50	7.8(-1)		
15	2.9(2)	35	2.5(1)	55	1.3(-1)		

Data obtained at low latitudes, L = 9°N [SA-77], yield larger mixing ratios than those found at higher latitudes as represented by the solid curve of Figure 10-2. Further examination of all the data (Figures 10-1 and 10-2) between 25 and 35 km indicates a general increase in mixing ratio with decrease in latitude. This general trend is supported by calculations and analyses [ME-76]. The following expression can be used to account for the increase in volume-mixing ratio with decrease in latitude:

$$m_R = m_R^\circ \left\{ 1 + \frac{2.92}{1 + \cosh[0.26(z-30)]} \frac{1}{1 + \exp[0.17(L-23)]} \right\} \qquad (2)$$

where m_R° is the mixing ratio given by the solid curve of Figure 10-2 and the data of Table 10-2, z is the altitude (km), and L is the latitude (degrees), north or south. Figure 10-3 shows the volume-mixing ratio as a function of latitude at selected altitudes according to Equation (2). The volume-mixing ratios for L = 0° are shown in Figure 10-2 by the dashed curve. Thus, the two curves in Figure 10-2 bracket the range of mixing ratio values generated by varying the value of latitude at each altitude.

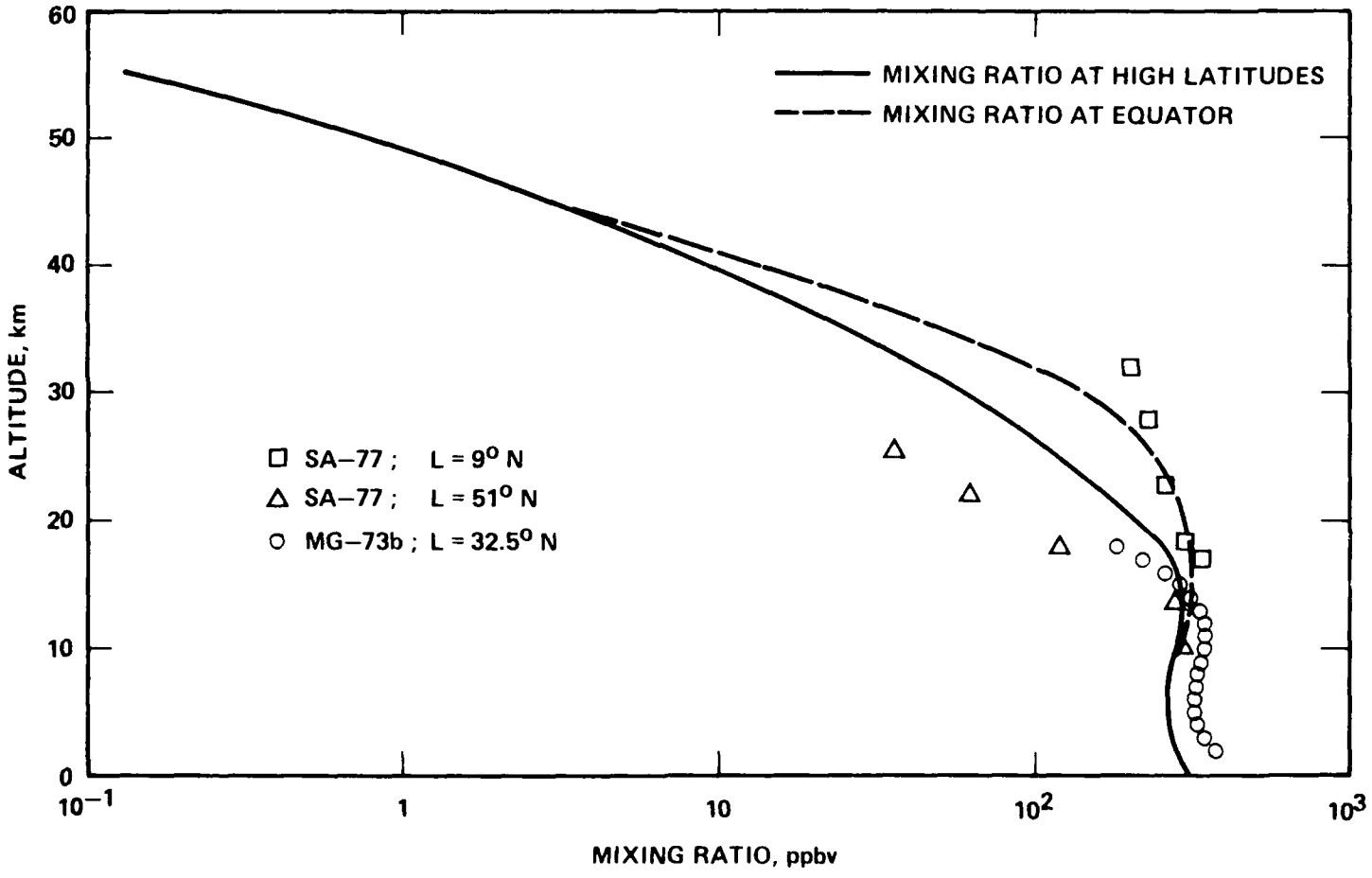

Figure 10-2. Selected data and profiles for N_2O volume-mixing ratio.

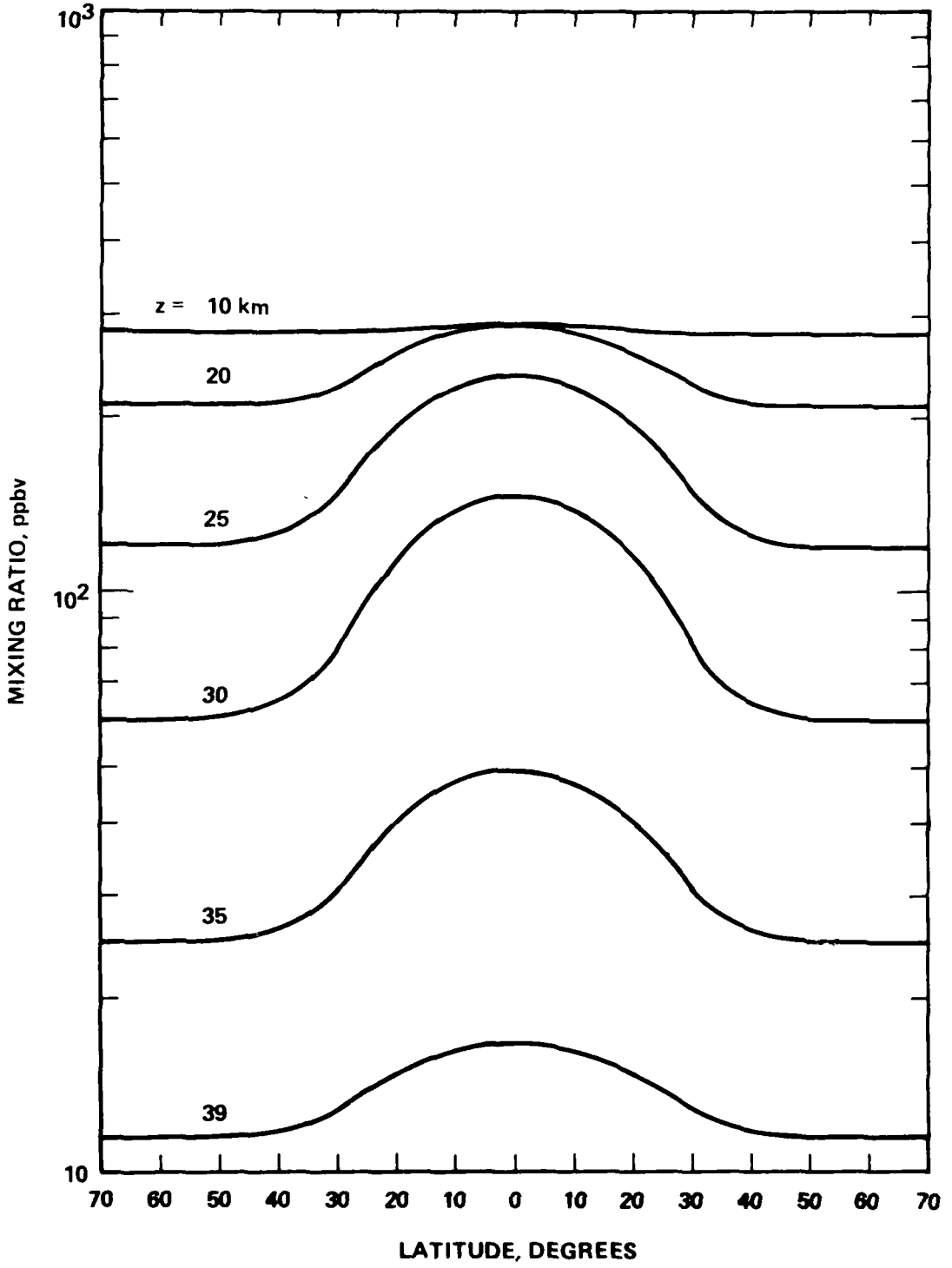

Figure 10-3. Latitude dependence of N_2O volume-mixing ratio for selected altitudes.

A second set of data shown in Figure 10-2, obtained at 51°N, are significantly lower than data in Figure 10-1, an unexpected feature based on the latitude at which the measurements were made. A possible explanation [SA-77] is that there was a mean downward stratospheric motion at the location of the measurements. Other measurements [SJ-70a] near the same latitude but at greatly different longitudes yield higher mixing ratios.

A third set of data [MG-73b] plotted in Figure 10-2 were not included in Figure 10-1 since it was not clear from the original paper [MG-73b] that the reported mixing ratios were volume-mixing ratios. These data are plotted in Figures 10-2 assuming they do represent volume-mixing ratios; Harries et al. [HB-74a] have also treated these data as volume-mixing ratios. The third set of data lies about 20 percent higher on the mixing ratio scale than the selected curve (the solid line of Figure 10-2). In view of the scatter in the data of Figure 10-1, this is probably not significant.

Additional measurements of the N_2O volume-mixing ratios from aircraft have been reported [RK-76]. These measurements lead to volume-mixing ratios of about 333 ppbv (with standard errors of less than 0.2 percent) but only the upper-limit altitude, about 14.2 km, was reported. At 14.2 km, the recommended values from Figure 10-2 lie between 290 and 310 ppbv.

The calculations of the N_2O profile in the stratsophere [Cr-74a, ME-76] are in reasonable agreement with the data. Calculations of Vupputuri [Vu-75], showing both a latitudinal and seasonal dependence for the volume-mixing ratio, are not in agreement with the latitudinal dependence given by the experimental data presented above.

Above 55-km altitude, the volume-mixing ratio is assumed to be constant at 0.13 ppbv. One calculation [SL-70a, SL-72] made to 140 km, shows the mixing ratio increasing between 50 and 140 km by about a factor of six; however, the absolute values of the volume-mixing ratios deduced from these calculations [SL-70a, SL-72] are high also by a factor of about six. Since the experimentally measured volume-mixing ratio is quite small already at 50 km, the densities of N_2O at higher altitudes will be negligible even if the error in magnitude should be as large as a factor of six.

10-3 ADDENDUM

After the selection of the N_2O profile data and formulation of Equation (2) describing the latitude dependence of the N_2O mixing ratio, an additional report on stratospheric measurements of N_2O appeared [KL-77a]. These measurements covered the altitude range between 12 and 20 km and the latitude range between 1° and 75°N. These data [KL-77a] are presented in Table 10-3. Only the mean latitudes and mixing ratios are listed in this table; data on longitude are not given here. Also listed in Table 10-3 are mixing ratios calculated from Equation (2) and the solid-curve profile in Figure 10-2. The correlation coefficient for the measured and calculated mixing ratios of Table 10-3 is about 0.85. Thus, the representation of N_2O mixing ratios presented in Section 10-2 is adequate and is retained without changes.

Table 10-3. Comparison of measured [KL-77a] and adopted stratospheric N_2O mixing ratios.

z km	Mean Latitude °N	Mixing ratio, ppbv Measured [KL-77a]	Mixing ratio, ppbv Adopted Eq. (2)	z km	Mean Latitude °N	Mixing ratio, ppbv Measured [KL-77a]	Mixing ratio, ppbv Adopted Eq. (2)
12.2	73	295	290	19.2	50	235	230
15.2	73	280	290	15.2	60	290	290
16.8	37.5	300	270	15.2	50	295	290
13.7	60	305	290	13.7	37.5	305	290
15.2	25.5	315	305	16.8	25.5	305	290
16.8	3	310	320	15.2	13.5	320	320
18.3	13.5	290	307	18.3	25.5	280	275
19.2	59.5	230	230	19.2	25.5	285	260
18.3	73	220	245	16.8	50	275	270
16.8	73	240	270	19.2	37.5	255	235
16.8	59.5	260	270	15.2	37.5	305	295

SECTION 11

A DENSITY PROFILE FOR NITRIC OXIDE

11-1 INTRODUCTION

The density profile for nitric oxide previously given [My-75] is herein revised, based on additional significant experimental measurements [BN-77, RS-75b, RS-76d, EM-77a, TI-75, DA-77, CS-76, TB-76]. These new data give information on the diurnal variation and on the variations with latitude, longitude, and magnetic activity. The analyses of these and other, unreported data are still in progress so that the revised model given below remains tentative.

Additional model calculations have been reported [SO-76, OK-77; also see OJ-75]. The important relations emphasized in SO-76 are the sensitivity of the nitric oxide concentration to (a) the molecular oxygen concentration above about 150 km and (b) the ratio of atomic- to molecular-oxygen concentrations below 150 km. The profiles provided here are largely empirical and modeling these dependencies becomes difficult.

The dependence of the nitric oxide concentration on the molecular oxygen concentration above 150 km had been included [My-75] by introducing a dependence of the nitric oxide concentration on the solar flux; this relationship is retained in the present model. In this connection, note that the recent measurements [RS-75b, RS-76d, EM-77a] correspond to low solar activity. By contrast, no attempt has been made to include the dependence of the nitric oxide on the ratio of atomic to molecular oxygen; this simplification may lead to significant inaccuracies below 150 km. Note that there are very few measurements of nitric oxide between 100- and 150-km altitude.

The profiles presented below include the diurnal and latitudinal dependence of the nitric oxide concentration.

11-2 NITRIC OXIDE DENSITIES ABOVE 100 KM

The available new measurements [RS-75b, RS-76d, EM-77a, DA-77] were obtained from satellites and cover the range generally between 160- and 250-km altitude. The most extensive measurements are reported by Engebretson et al. [EM-77a]. A diurnal vatiation, based on the data in EM-77a, has been deduced here to be given by the form

$$\ell n[NO]_{z,t,F} = A(z,F) + B(z)\sin(15t-\phi) \qquad (1)$$

where A and B depend on the altitude (z), F is the 10.7-cm solar flux, t is the local apparent time (in decimal hours), and ϕ is the phase angle selected to be 105° which results in a maximum density at t = 13 hr [OJ-75, SO-76]. The previously given procedure [My-75] is used for introducing the dependence on F. At 100 km, the nitric oxide density is fixed (to two significant figures) to be 3.4×10^7 cm^{-3}, independent of F; at 215 km, the dependence of the nitric oxide on F is established on the basis of experimental observations and model calculations. For intermediate altitudes and those above 215 km, nitric oxide densities are determined by interpolation and extrapolation as indicated below.

To obtain the dependence of the nitric oxide density on F, the data previously used and more recent data were adjusted for diurnal variation to t = 19 hr; in this case, the second term on the right-hand side of Equation (1) is zero. These data and the adjusted values are given in Table 11-1 and shown in Figure 11-1. The curve in Figure 11-1 is given by the expression

$$\ell n[NO]_{215,19,F} = A(215,F) = 9.68 + \frac{6.08}{1 + 5 \times 10^5 F^{-3}} \cdot \qquad (2)$$

By combining Equation (2) with the value of A at 100 km and using a linear relation, we prescribe the value of A at any altitude above 100 km to be given by

$$A(z,F) = A_o + [A(215,F) - A_o]\,\frac{z - 100}{115} \qquad (3)$$

Table 11-1. Dependence of the nitric oxide densities at 215-km altitude on local apparent time (t) and decimetric solar flux (F).

Date[a]	t Hours	F[b]	$[NO]_{215,t,F}$, cm^{-3} Measured	Adjusted to t=19 hrs	Reference
1/04/74	18.75	75	<7(5)	<6.5(5)	FT-74
6/--/74	-	142	5(6)	5(6)	
1/31/69	14.17	130	2.9(6)	1.0(6)	Me-71
2/06/69	14.48	142.5			OJ-75
5/26/71	5.93	91	1.5(6)	2.0(6)	Ti-73,OJ-75
2/08/74	∿13.0	81	6.8(5)	2.3(5)	RS-75b,RS-76d
5/16/74	10.92-11.92	79	1.3(6)	4.8(5)	EM-77a
5/28/74	8.97-9.27	85	8.0(5)	4.8(5)	EM-77a
6/10/74	17.9	95	3.9(5)	5.2(5)	EM-77a

[a] Month/day/year.
[b] In units of 10^{-22} W m^{-2} Hz^{-1}.

where

$$A_o \equiv \ell n[NO]_{100,L} \approx \ell n(3.4 \times 10^7) \; ; \qquad (4)$$

A_o will be defined more precisely later.

The diurnal variation of [NO] is small at 100 km and increases with increasing altitude [My-75]. Based on the recent data [EM-77a], the coefficient B(z) in Equation (1), which governs the magnitude of the diurnal variation, is taken to be

$$B(z) = 1.1\{1 - \exp[-0.066(z-100)]\} \quad z \geq 100 \text{ km}. \qquad (5)$$

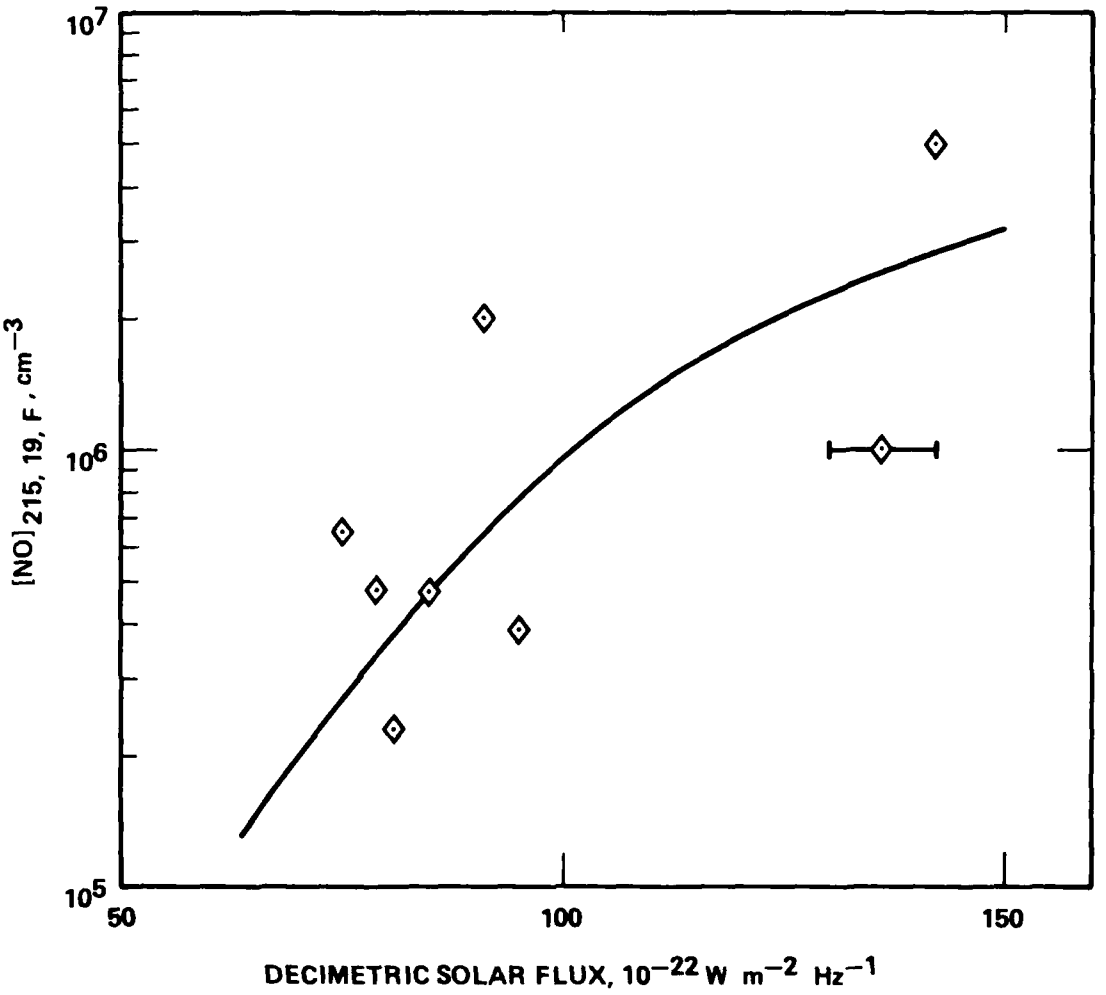

Figure 11-1. Nitric oxide densities at 215-km altitude and 19 hours as a function of F.

A strong latitudinal dependence has been reported [CS-76]; however, no data on this dependence are available at present. Thus, an estimate of the magnitude of the change in nitric oxide density by a factor of four between 0° and 90° latitude has been made. This estimate was guided by the magnitudes of the corresponding changes in the case of nitrogen atoms [TT-76a, EM-77] and on the preliminary report [DA-77] of measurements of nitric oxide in the nighttime equatorial region. The densities of nitric oxide represented by Equations (1) through (5) were assumed to apply to a latitude of 50°; it follows that a more general expression,

$$\boxed{\ell n[NO]_{z,t,L,F} = \ell n[G(L)] + A(z,F) + B(z)\sin(15t-105),} \quad (6)$$

where the latitude-dependent function is

$$G(L) = 0.375 + 0.0125L , \quad (7)$$

gives the nitric oxide density as a function of altitude, diurnal time, latitude, and solar flux, for $z \geq 100$ km.

The nitric oxide densities calculated according to Equations (1) through (7) are compared with the observed nitric oxide densities in Table 11-2. The mean absolute error is 50 percent.

The nitric oxide densities calculated according to Equations (1) through (7) are compared with the model calculations [SO-76] in Table 11-3. The purpose of this comparison is to give an indication of the possible errors involved in using Equations (1) through (7) between 100- and 150-km altitudes where, as noted above, the errors are likely to be high due to the complexity of the natural phenomena. For the conditions of the measurements of FT-74, the absolute errors range from 0 to 280 percent whereas for the conditions of the measurements of RS-75b, the nitric oxide densities computed according to Equations (1) through (7) are factors of 7 to 11 higher than those computed in SO-76.

Improvement in the empirical model of nitric oxide densities presented here will require measurements between 100- and 150-km altitude for a variety of conditions and access to detailed results of code models [e.g., SO-76].

Table 11-2. Comparison of calculated and measured nitric oxide densities above 100-km altitude.

z km	F[a]	L Degrees	t Hours	$[NO]_{z,t,L,F}$, cm^{-3} Eq. (6)	$[NO]_{z,t,L,F}$, cm^{-3} Measured	Ref.
180	79	50.61	11.91	3.9(6)	5.0(6)	EM-77a
	85	42.91	9.26	2.9(6)	2.3(6)	
	94	34.78	6.36	1.9(6)	1.5(6)	
200	79	47.79	11.70	1.7(6)	2.2(6)	
	85	40.01	9.11	1.3(6)	1.3(6)	
	94	31.53	6.24	7.3(5)	7.1(5)	
240	79	43.22	11.43	3.0(5)	4.8(5)	
	85	35.19	8.90	2.5(5)	3.4(5)	
	94	26.34	6.05	1.7(5)	1.3(5)	EM-77a
215	75	∿32	18.75	2.2(5)	<7(5)	FT-74
160.5	81	38.9	12.89	8.0(6)	3.4(6)	RS-75b
178.6	81	32.9	13.15	3.6(6)	2.1(6)	RS-75d
200.4	81	28.8	13.30	1.4(6)	1.1(6)	TT-76a
246.7	81	22.7	13.51	7.6(5)	∿2(5)	TT-76a
120	142	45	NA	2.1(7)	3.0(7)	Kr-70a
160	142	45	↓	8.8(6)	1.3(7)	↓
200	142	45	↓	3.7(6)	7.2(6)	↓
220	142	45	NA	2.4(6)	3.8(6)	Kr-70a

[a] In units of 10^{-22} W m^{-2} Hz^{-1}.

Table 11-3. Comparison[a] of nitric oxide densities calculated from Equation (6) with model calculations.

z km	F[b]	L Degrees	t Hours	$[NO]_{z,t,L,F}$, cm^{-3} Eq. (6)	$[NO]_{z,t,L,F}$, cm^{-3} Model[c]	Ref.
103	75	∿32	24.0	1.9(7)	5.0(6)	FT-74
107	↓	↓	14.0	2.9(7)	1.0(7)	↓
125			12.0	2.2(7)	1.5(7)	
153			18.0	3.7(6)	5.0(6)	
153			4.0	1.3(6)	1.0(6)	
183	↓	↓	8.0	1.0(6)	1.0(6)	FT-74
120	81	33[d]	∿13	2.8(7)	2.5(6)	RS-75b
140	81	33	∿13	1.5(7)	4.4(6)	RS-75b

[a] The comparisons, with arbitrarily selected data of the model calculations, are intended only to give an indication of the magnitude of the errors involved in using Equations (1) through (7) between 100- and 150-km altitude where experimental data are lacking.

[b] In units of 10^{-22} W m^{-2} Hz^{-1}.

[c] The model calculations are reported in SO-76 and the calculations apply to the conditions for the measurements listed in Reference.

[d] This value selected for the model calculations [SO-76].

11-3 NITRIC OXIDE DENSITIES BELOW 100 KM

Since the previous report [My-75] there have been two rocket-borne measurements [BN-77, TI-75] of the nitric oxide distribution between 70- and 115-km altitude. These data, together with those of Meira [Me-71], have been used to revise the selected daytime nitric oxide densities between 65 and 100 km. Below 65 km, we retained the nitric oxide densities previously selected [My-75].

The nighttime densities which were based on model calculations [My-75] were revised to be consistent with the new daytime values. All selected densities are listed in Table 11-4. Note that for altitudes of 100 km and lower, the diurnal variation is treated by using one set of values for the nitric oxide density for daytime and another set of values for nighttime, as done previously [My-75].

The latitude dependence apparently extends below 100-km altitude; in the present model, this dependence is assumed for altitudes down to about 60 km by use of the relation

$$\boxed{\ell n[NO]_{z,i,L} = \ell n[NO]_{z,i} + C(z)\ell n[G(L)]} \qquad (8)$$

where the subscripts z, i, and L denote altitude (km), diurnal condition (noon or midnight), and (the absolute value of) latitude (degrees), respectively. The values of $[NO]_{z,i}$ for i = noon and i = midnight are given in Table 11-4 for z = 0(5)100 km. The latitude-dependent function, G(L), is given by Equation (7). The altitude-dependent coefficient for the latitude term,

$$C(z) = \{1 + \exp[-0.22(z-72)]\}^{-1} , \qquad (9)$$

is designed to make the latitude dependence negligible for $z \lesssim 60$ km and to allow it to grow to a full effect for $z \gtrsim 85$ km.

11-4 PRECISE DEFINITION OF A_o

The quantity A_o in Equation (4) can now be defined precisely. By requiring equality of the two expressions for the nitric oxide density (Equations (6) and (8)) at 100-km altitude, and using the facts that

Table 11-4. Nitric oxide profile for noon and midnight conditions between 0-and 100-km altitude and at 50° latitude.

z km	$[NO]_{z,i,50}$, cm^{-3} Noon	Midnight	z km	$[NO]_{z,i,50}$, cm^{-3} Noon	Midnight
0	1.0(10)	1.0	55	3.0(8)	1.0(4)
5	3.4(9)		60	1.4(8)	1.1(5)
10	1.3(9)		65	6.4(7)	2.3(5)
15	5.8(8)		70	2.7(7)	4.8(5)
20	7.0(8)		75	1.3(7)	1.0(6)
25	1.75(9)		80	6.2(6)	2.0(6)
30	2.1(9)		85	4.3(6)	4.3(6)
35	1.75(9)		90	8.2(6)	8.2(6)
40	1.25(9)		95	1.9(7)	1.9(7)
45	8.5(8)		100	3.4(7)	3.4(7)
50	5.1(8)	1.0			

$$B(100) = 0 \qquad \text{and} \qquad A(100,F) = A_o , \tag{10}$$

we can now find that A_o is given by

$$A_o \equiv \ell n[NO]_{100,L} = \ell n[NO]_{100,i} - [1 - C(100)]\ell n[G(L)]. \tag{11}$$

Note that A_o is essentially independent of latitude, since $[1 - C(100)] \approx 0.002$; this is a reason for not using the notation $A(z,L,F)$.

SECTION 12

A DENSITY PROFILE FOR NITROGEN ATOMS

12-1 INTRODUCTION

The density profile for nitrogen atoms previously given [My-75] is herein revised, based on additional significant experimental measurements, generally above 150-km altitude [DA-77, EM-77a, Ge-75, ME-75, ME-76a, ME-76b, RS-75b, RS-76d, TB-76a, TT-75, TT-76a]. All but one, DA-77, are based on satellite measurements and cover the range from 100-to 500-km altitudes. These measurements demonstrate the effects of diurnal, seasonal, latitudinal, and geomagnetic activity variations on nitrogen atom densities. However, the data are selective in terms of seasonal, geographical, and solar flux variations; with respect to the latter, the recent data apply to the minimum in the solar cycle. The analysis of these data is still in progress and the revised model given below is thus interim in nature.

Two new model calculations have been reported [EM-77, SO-76; also see OJ-75]. One of these [EM-77] applies to an altitude of 375 km and accounts for geomagnetic and solar activity, latitudinal effects, both symmetrical and asymmetrical semiannual and annual variations, and diurnal, semidiurnal, and terdiurnal variations.

The profile presented below includes diurnal, seasonal, latitudinal, and solar flux variations with added structure to account for an altitudinal variation of the diurnal component and a diurnal variation of the latitudinal component.

12-2 NITROGEN ATOM DENSITY PROFILE

The nitrogen atom densities are represented by an empirical formula which is constructed by first considering the diurnal, seasonal, latitudinal, and solar flux variations, in turn, and then by adjusting the model as required after comparing predictions and observations. The objective was to be able to predict nitrogen atom densities within a factor of two of the presently available data. The dependencies

included in the empirical formulation are those which have variations equal to or larger than a factor of two and for which some observational data are available.

The formula deduced for (both ground and excited-state) nitrogen atom densities may be written as follows:

$$[N] \equiv [N(z,t,L,F)]$$

$$= T_1(z)T_2(L,t)\exp[T_3(f) + T_4(t,z,L)]T_5(F) \qquad (1)$$

where

- z = altitude, km
- t = local apparent time, decimal hours
- L = absolute value of the latitude, degrees
- f = fractional season-year, being 0 on 1 January in northern hemisphere and on 1 July in southern hemisphere
- F = solar decimetric (10.7-cm) flux, 10^{-22} W m^{-2} Hz^{-1}.

Latitudinal symmetry has been assumed for simplicity, an assumption which is accurate only during particular seasons [EM-77].

The basic component, $T_1(z)$, obtaining for t = 9.4 hr, L = 50°, f = 0.25 yr, and $F \approx 50$, is specified in Table 12-1 and shown in Figure 12-1.

The latitudinal factor with its diurnal variation, $T_2(L,t)$, is given by

$$T_2(L,t) = \left[0.6 + \left\{0.56 + 0.44 \sin\left[\left(\frac{t}{24} - \frac{141}{360}\right) 2\pi\right]\right\} \frac{2.87}{1+e^{0.07(|L|-24)}}\right]^{\frac{1}{2}} . \qquad (2)$$

The diurnal maximum and minimum extents of T_2, i.e., $T_2(L,15.4)$ and $T_2(L,3.4)$, respectively, are plotted in Figure 12-2. The total latitudinal variations for the diurnal maximum and minimum are

$$T_2(0,15.4)/T_2(90,15.4) = 2.2$$

$$T_2(0,3.4)/T_2(90,3.4) = 1.2 \ .$$

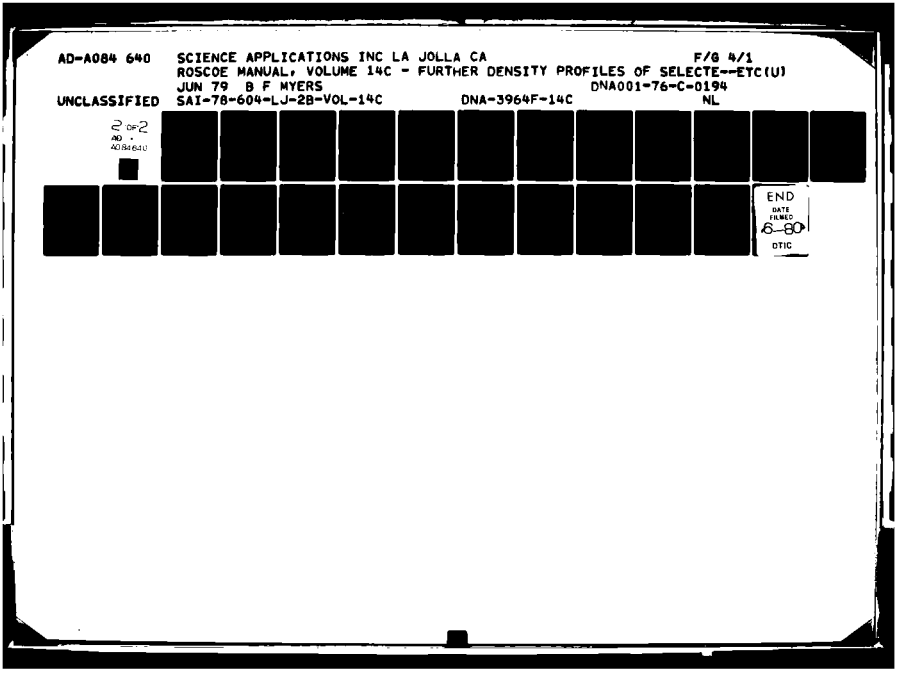
AD-A084 640
SCIENCE APPLICATIONS INC LA JOLLA CA
F/G 4/1
ROSCOE MANUAL, VOLUME 14C - FURTHER DENSITY PROFILES OF SELECTE--ETC(U)
JUN 79 B F MYERS
DNA001-76-C-0194
UNCLASSIFIED
SAI-78-604-LJ-2B-VOL-14C
DNA-3964F-14C
NL
2 OF 2
AD A084640
END
DATE FILMED
6-80
DTIC

Table 12-1. Basic component of nitrogen atom profile.[a]

z km	[NO] cm^{-3}	z km	[NO] cm^{-3}	z km	[NO] cm^{-3}
<100	b	120	1.26(7)	145	3.30(7)
100	1.33(6)	125	1.74(7)	150	3.35(7)
105	2.90(6)	130	2.26(7)	155	3.31(7)
110	5.20(6)	135	2.82(7)	160	3.20(7)
115	8.60(6)	140	3.14(7)	>160	c

[a] Obtains for t=9.4 hr, L=50°, f=0.25 yr, $F \lesssim 50$.

[b] $T_1(z) = [N(100)]\exp[-0.144(100-z)]$, $0 \leq z < 100$.

[c] $T_1(z) = [N(160)]\exp[-0.0178(z-160)]$, $z > 160$.

The seasonal factor is $\exp[T_3(f)]$, with $T_3(f)$ given by

$$T_3(f) = 0.693 \sin[(f-0.25)2\pi] . \quad (3)$$

The seasonal factor is a maximum at f = 0.5 and is smaller by a factor of 4.0 at its minimum. The selection of this factor is based on ME-76b.

The principal diurnal factor, with its altitudinal and latitudinal variations, is $\exp[T_4(t,z,L)]$, with $T_4(t,z,L)$ given by

$$T_4(t,z,L) = \frac{1.42 \sin[(\frac{t}{24} - \frac{141}{360})2\pi]}{\{1 + \exp[0.146(L-75)]\}\{1 + \exp[-0.02(z-220)]\}} . \quad (4)$$

The adequacy of the functional form $A \exp[(B/CD)\sin x]$ to represent the diurnal variation according to (selected) experimental data is illustrated in Figure 12-3 where this functional form is plotted with the parameters having the following values:

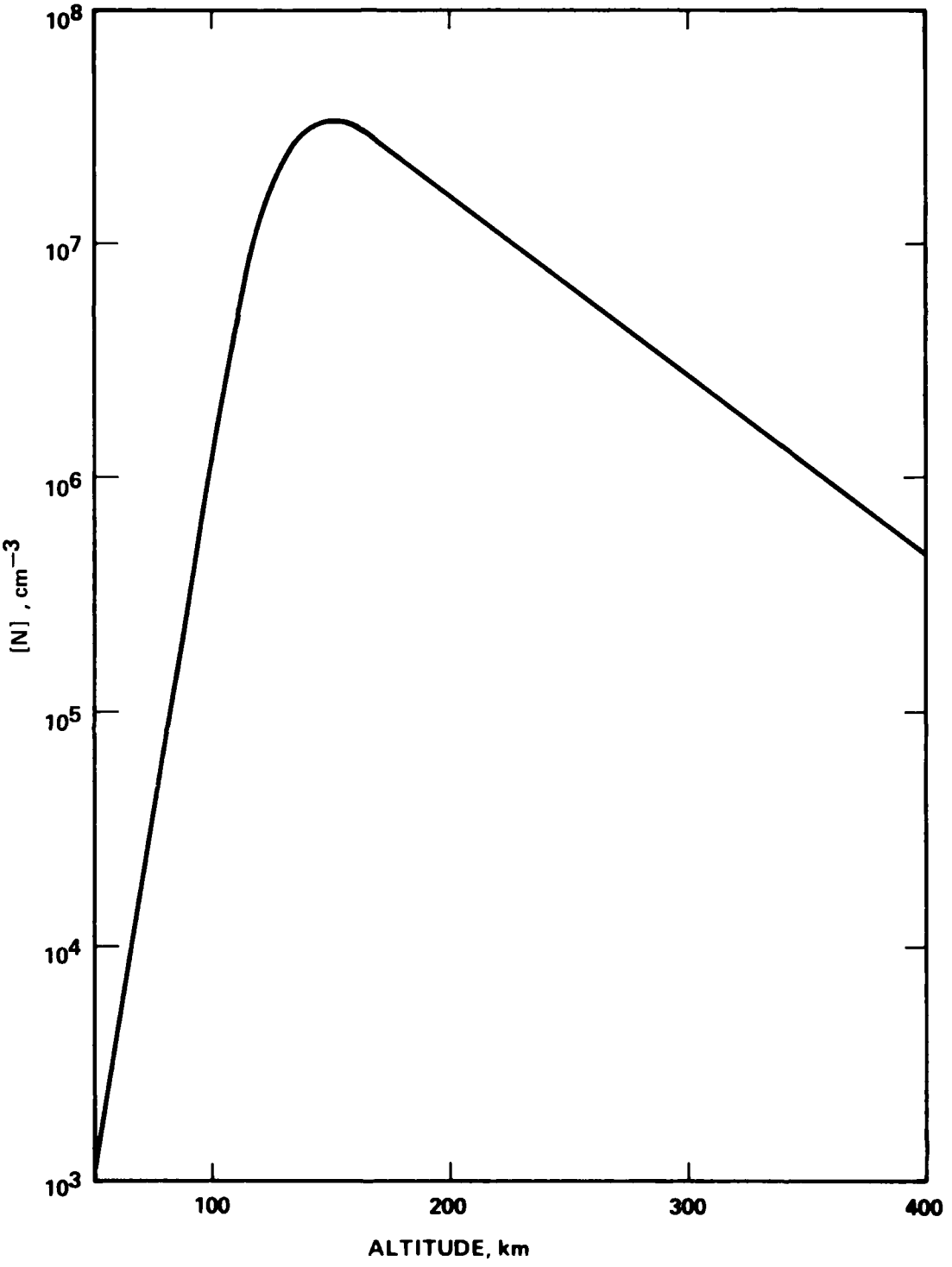

Figure 12-1. Basic component of nitrogen atom profile (for t=9.4 hr, L=50°, f=0.25 yr, $F \lesssim 50\times10^{-22}$ W m^{-2} Hz^{-1}).

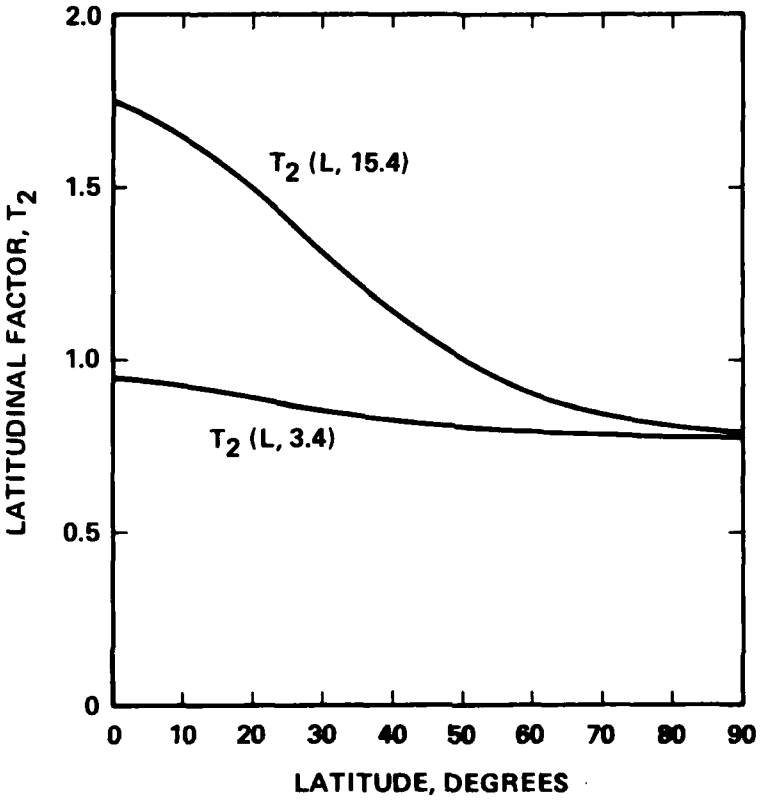

Figure 12-2. The diurnal maximum (at t=15.4 hr) and minimum (at t=3.4 hr) variations in the latitudinal factor for the nitrogen atom density.

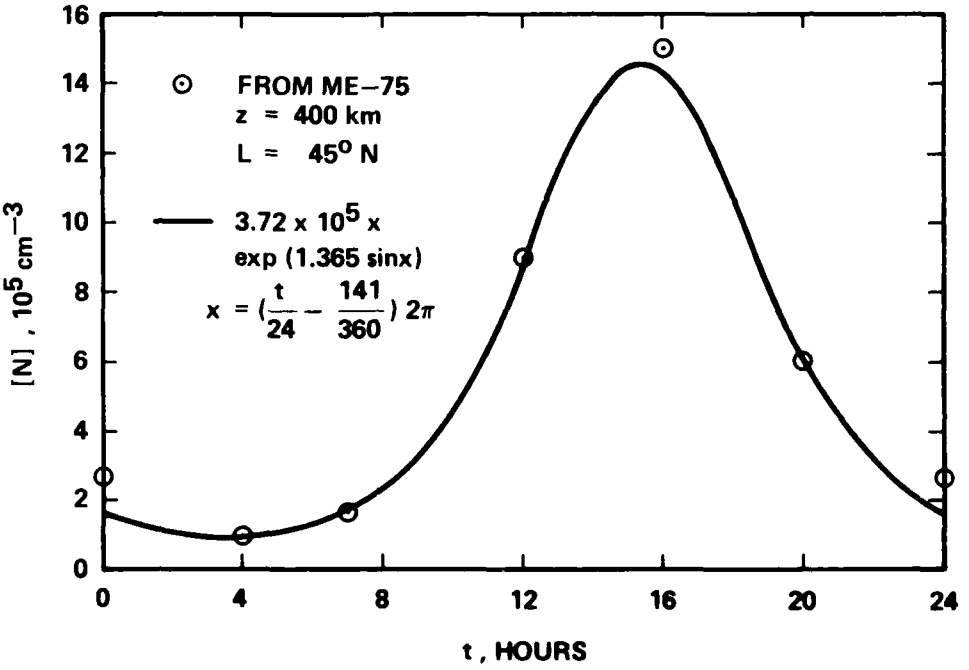

Figure 12-3. Comparison of the model (principal) diurnal variation with experimental data.

$$B = 1.42$$

$$C = 1.013 \text{ (corresponding to } L = 45°)$$

$$D = 1.027 \text{ (corresponding to } z = 400 \text{ km)}$$

$$B/(CD) = 1.365$$

$$A = 3.72 \times 10^5 \text{ (selected to optimize fit)} .$$

The diurnal variation depends on the altitude and latitude. The altitude variation of the total diurnal variation is shown in Figure 12-4 where the ordinate is the ratio of diurnal factors for diurnal maximum and diurnal minimum,

$$\frac{\exp[T_4(15.4,z,50)]}{\exp[T_4(3.4,z,40)]} ,$$

i.e., L = 50° latitude, t is 15.4 and 3.4 for diurnal maximum and minimum. The altitude dependence of the diurnal variation shown in Figure 12-4 is based on an analysis of the data presented in EM-77a with consideration of the variations and differences in variations in ME-76a and OJ-75.

The diurnal variation decreases poleward [EM-77] and the latitude-dependent factor in Equation (4) takes this into account. Thus the variation at L = 90° is 0.1 of that at L = 50°.

The solar-flux factor, $T_5(F)$, is given by

$$T_5(F) = 1 + \frac{3}{1 + \exp[-0.1(F-132)]} . \qquad (5)$$

$T_5(F)$, representing the effect of the solar flux on the nitrogen atom density, is a very crude estimate. The nitrogen atom density is expected [EM-77] to increase with increasing solar flux. However, data on the effect are lacking. The recent measurements [DA-77, EM-77a, Ge-75, ME-75, RS-75b, RS-76d, TT-75, TT-76a] were obtained under solar cycle minimum conditions for which the flux $F(10^{-22}$ W m^{-2} Hz^{-1}) ranges between 80 and 100. Only two data sets considered below [GH-68a, OP-72] are for significantly larger solar fluxes. It was on the

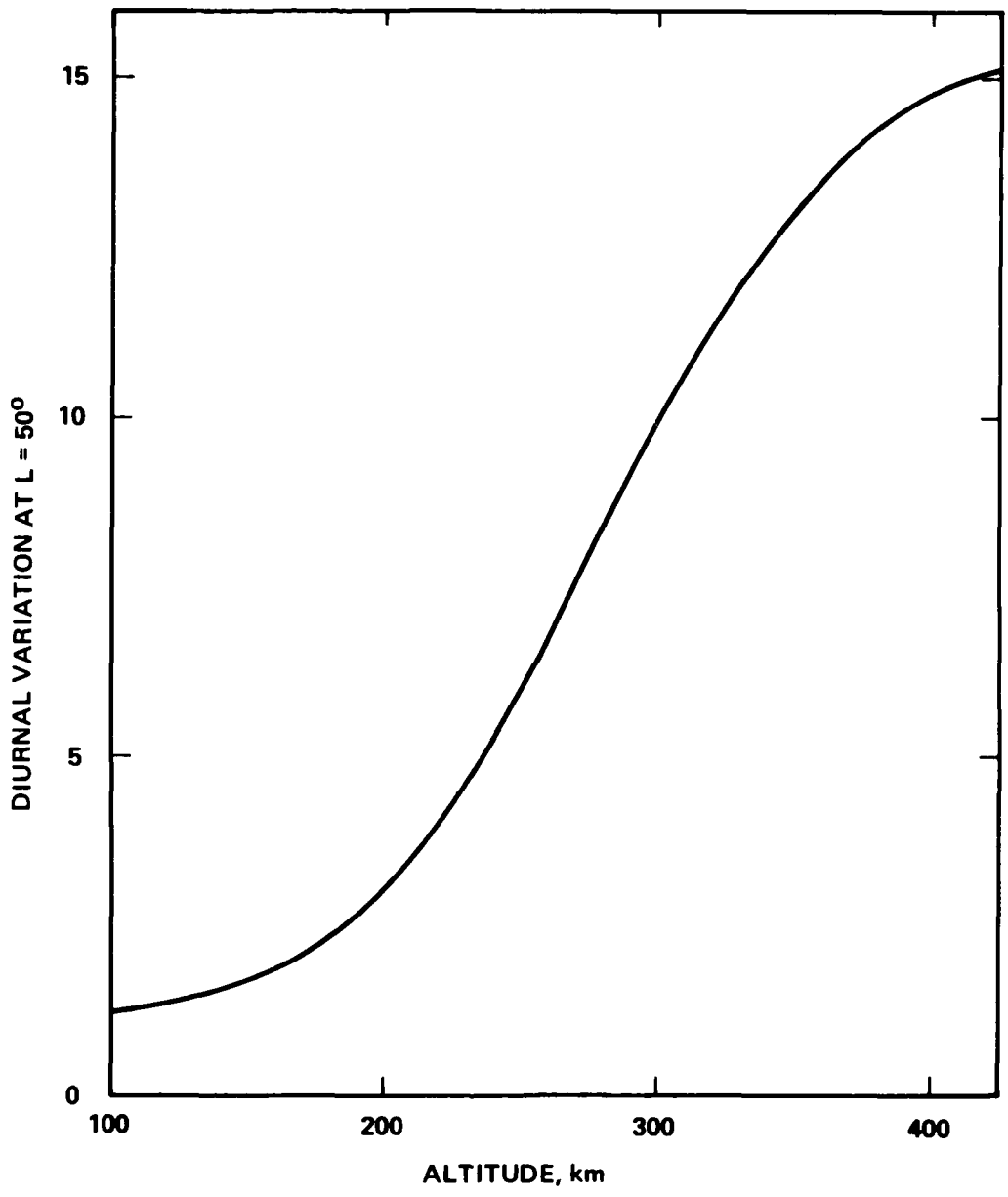

Figure 12-4. Altitude dependence of the diurnal variation at L=50°.

basis of these measurements that the magnitude of the factor T_5 in Equation (5) was based. Note should be taken of the possibility of experimental error [OP-72, ME-75] in these two measurements [GH-68a, OP-72].

12-3 COMPARISON OF MODEL PROFILE DENSITIES AND OBSERVATIONS

The predictions of Equation (1) are compared with the observed nitrogen atom densities in Table 12-2 and in Figure 12-5. The errors given in Table 12-2 are generally within a factor of two of the observed data. The principal exception occurs in comparison of calculations with the data of Ge-75. These data are not in agreement with the datum given in TT-76a for 160 km and L $\tilde{\sim}$ 40° (this datum is also that in RS-76d and is the correction of the value given previously in RS-75b). For the two reports [TT-76a, Ge-75], the f-values are similar but the observation time is about 13 hr in TT-76a (RS-76d) and about 18 hr in Ge-75; yet, the reported nitrogen atom density is the same. It is quite certain that the density for conditions of Ge-75 (i.e., $\sim$18 hr) should be lower than that for conditions of TT-76a (RS-76d) (i.e., $\sim$13 hr). Also note that the altitude dependence of the nitrogen atom density is essentially the same for the calculations and measurements [Ge-75] above 190 km.

Table 12-2. Comparison of calculated and observed nitrogen atom densities.

z km	L Degrees	t Hours	f[a]	F[b]	[N], cm^{-3} Calc.	[N], cm^{-3} Observed	Error Percent	Ref.
200	47.0	11.73	0.372	79	3.53(7)	3.21(7)	10.0	EM-77a
200	40.0	9.13	0.405	85	2.71(7)	3.09(7)	-12.3	
200	31.5	6.25	0.441	94	1.94(7)	1.51(7)	28.5	
240	42.5	11.44	0.372	79	2.02(7)	2.21(7)	- 8.6	
240	35.2	8.56	0.405	85	1.18(7)	1.37(7)	-13.9	
240	26.3	6.05	0.441	94	7.70(6)	6.72(6)	14.6	
300	36.9	11.16	0.372	79	8.12(6)	8.58(6)	- 5.4	
300	29.2	8.69	0.405	85	4.18(6)	4.58(6)	- 8.7	
300	20.1	5.87	0.441	94	2.04(6)	1.61(6)	26.7	
400	29.8	10.86	0.372	79	1.47(6)	1.85(6)	-20.5	
400	21.6	8.44	0.405	85	6.58(5)	7.00(5)	- 6.0	
400	12.0	5.62	0.441	94	2.83(5)	2.59(5)	9.3	EM-77a
140	32	18.75	0.0876	75	2.48(7)	1.90(7)	30.5	FT-74
225	≈13	≈0.0	0.548	79	1.33(7)	0.56(7) to 1.1(7)	137 to 20.9	DA-77
160.5	38.9	12.89	0.1068	81	2.77(7)	4.60(7)	-39.8	TT-76a
200.4	28.8	13.3	0.1068	81	1.97(7)	2.75(7)	-28.4	
246.7	22.7	13.51	0.1068	81	1.26(7)	1.30(7)	- 3.1	
308.9	16.6	13.69	0.1068	81	6.09(6)	5.20(6)	17.1	
333.1	14.6	13.75	0.1068	81	4.35(6)	3.50(6)	24.3	
386.1	10.6	13.86	0.1068	81	1.92(6)	1.60(6)	20.0	
414.9	8.6	13.92	0.1068	81	1.20(6)	9.8 (5)	22.4	TT-76a
150	39	4.75	0.104	137	3.59(7)	2.80(7)	28.2	OP-72[c]
100	40	≈18.3	0.959	82	8.35(5)	2.72(5)	207	Ge-75
150	40	≈18.3	0.959	82	2.37(7)	2.32(7)	2.2	
200	40	≈18.3	0.959	82	1.37(7)	8.76(7)	-84.4	
300	40	≈18.3	0.959	82	3.58(6)	2.03(7)	-76.4	Ge-75
165	32	5.95	0.6023	140	1.08(8)	1.82(8)[d]	-40.6	GH-68a
184	32	5.95	0.6023	140	7.04(7)	1.24(8)	-43.2	GH-68a
213	32	5.95	0.6023	140	3.60(7)	4.40(7)	-18.2	GH-68a
137	32	14.0	0.0876	75	2.59(7)	2.0 (7)	29.5	SO-76[e]
177	32	14.0	0.0876	75	2.49(7)	2.0 (7)	24.5	SO-76[e]
199	32	14.0	0.0876	75	1.92(7)	1.5 (7)	28.0	SO-76[e]

[a] Fractional season-year.

[b] The solar flux values, in units of 10^{-22} W m^{-2} Hz^{-1}, were obtained from among (a) the cited references, (b) the Geomagnetic and Solar Data sheet appearing at the end of issues of J. Geophys. Res., and (c) "Solar Geomagnetic Data," IER-FB-277, 5, Sept. 1967 (for the case of GH-68a).

[c] The measurements are regarded as quite uncertain.

[d] Average of measurements at 164 and 166 km.

[e] Calculations included conditions appropriate to experiment of FT-74; these data used to help establish the basic component, $T_1(z)$ of [N] for $100 \leq z(km) \leq 160$ as given in Table 12-1.

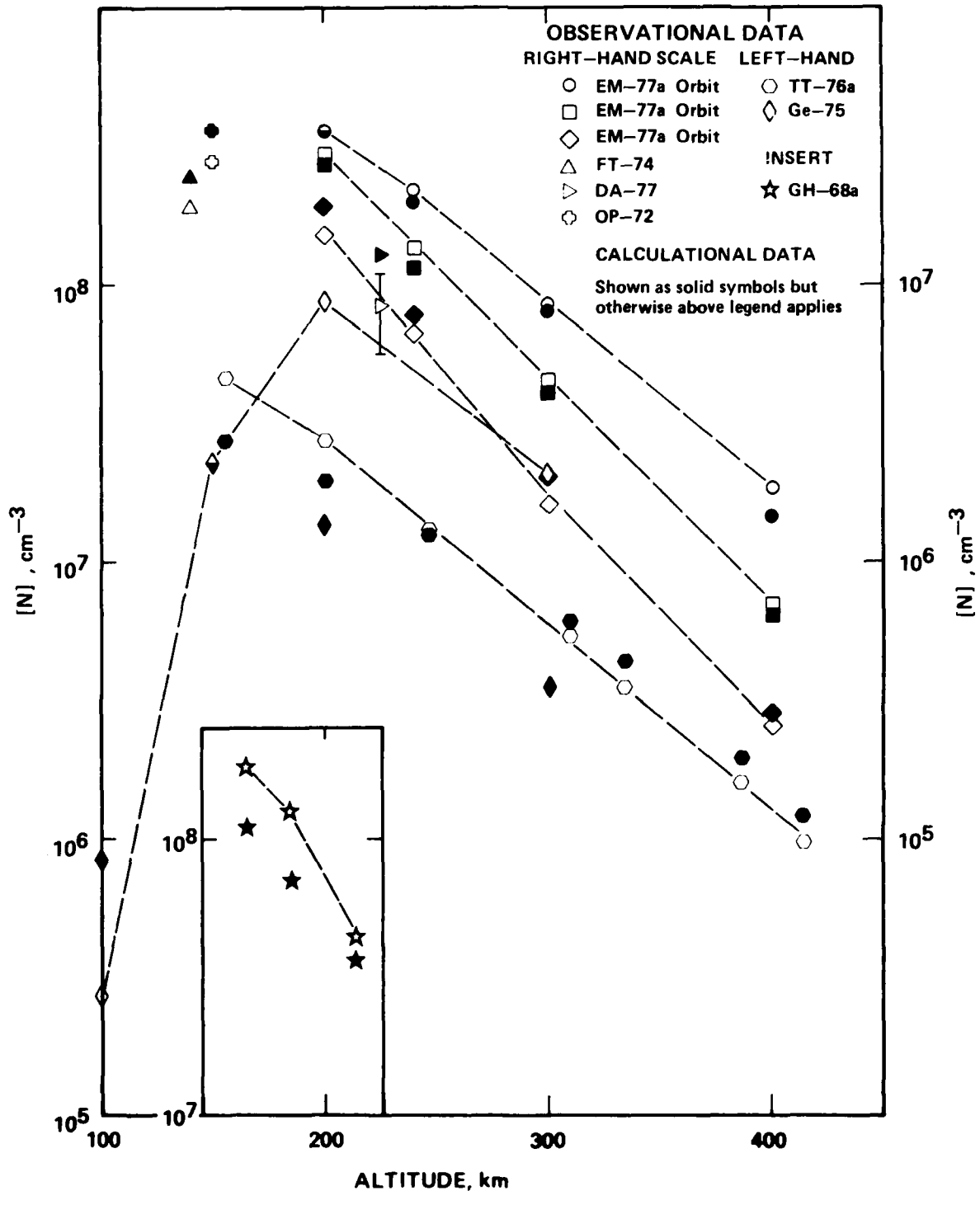

Figure 12-5. Comparison of calculated and observed nitrogen atom densities.

SECTION 13

A DENSITY PROFILE FOR N(^{2}D) ATOMS

13-1 INTRODUCTION

There are no direct measurements of the N(^{2}D) atom density in the atmosphere. However, there are recent values derived from measurements of the 5200 Å dayglow [RS-75b, RS-76d]. These values are used as a basis for determining the N(^{2}D) profile between 160- and 290-km altitude. At other altitudes the profile is extrapolated by using, as a guide, the profile for nitrogen atoms in Figure 12-1.

The effects of seasonal, latitudinal, and solar- and geomagnetic-activity variations on the density of N(^{2}D) have not been observed. In the present model, these effects are treated as in the nitrogen atom model of Section 12 except for the diurnal variation. Since the N(^{2}D) density decreases to very low values during nighttime, the model of Section 12 is augmented by a diurnal variation factor.

13-2 N(^{2}D) PROFILE

The N(^{2}D) densities are calculated from the expression

$$[N(^2D)] \equiv [N_{2D}(z,t,L,f,F)]$$

$$= \frac{[N(z,t,L,f,F)]}{T_1(z)} T_7(z)T_8(t) \qquad (1)$$

where [N(z,t,L,f,F)] is the total nitrogen atom density given by Equation (1) of Section 12 and $T_1(z)$ is specified in Table 12-1. All the arguments are defined in Section 12.

The basic component for N(^{2}D), $T_7(z)$, obtaining for t = 9.4 hr, L = 50°, f = 0.25 yr, and $F \lesssim 50$, is specified in Table 13-1 and shown in Figure 13-1.

The diurnal factor for N(^{2}D) is given by

$$T_8(t) = \{1 + \exp[-2.197(t-6)]\}^{-1} \{1 + \exp[2.197(t-18)]\}^{-1} \quad (2)$$

and is shown in Figure 13-2.

Table 13-1. Basic component of $N(^2D)$ profile.[a]

z km	$[N(^2D)]$ cm^{-3}	z km	$[N(^2D)]$ cm^{-3}	z km	$[N(^2D)]$ cm^{-3}
<125	b	150	3.1(5)	180	6.5(5)
125	1.3(4)	155	4.6(5)	185	6.4(5)
130	3.0(4)	160	5.5(5)	190	6.3(5)
135	6.3(4)	165	6.0(5)	195	6.1(5)
140	1.2(5)	170	6.4(5)	200	5.7(5)
145	2.0(5)	175	6.5(5)	>200	c

[a] Obtains for t=9.4 hr, L=50°, f=0.25 yr, $F \lesssim 50$.

[b] $T_7(z) = [N_{2D}(125)]\exp[-0.184(125-z)]$, $0 \leq z < 125$.

[c] $T_7(z) = [N_{2D}(200)]\exp[-0.0282(z-200)]$, $z > 200$.

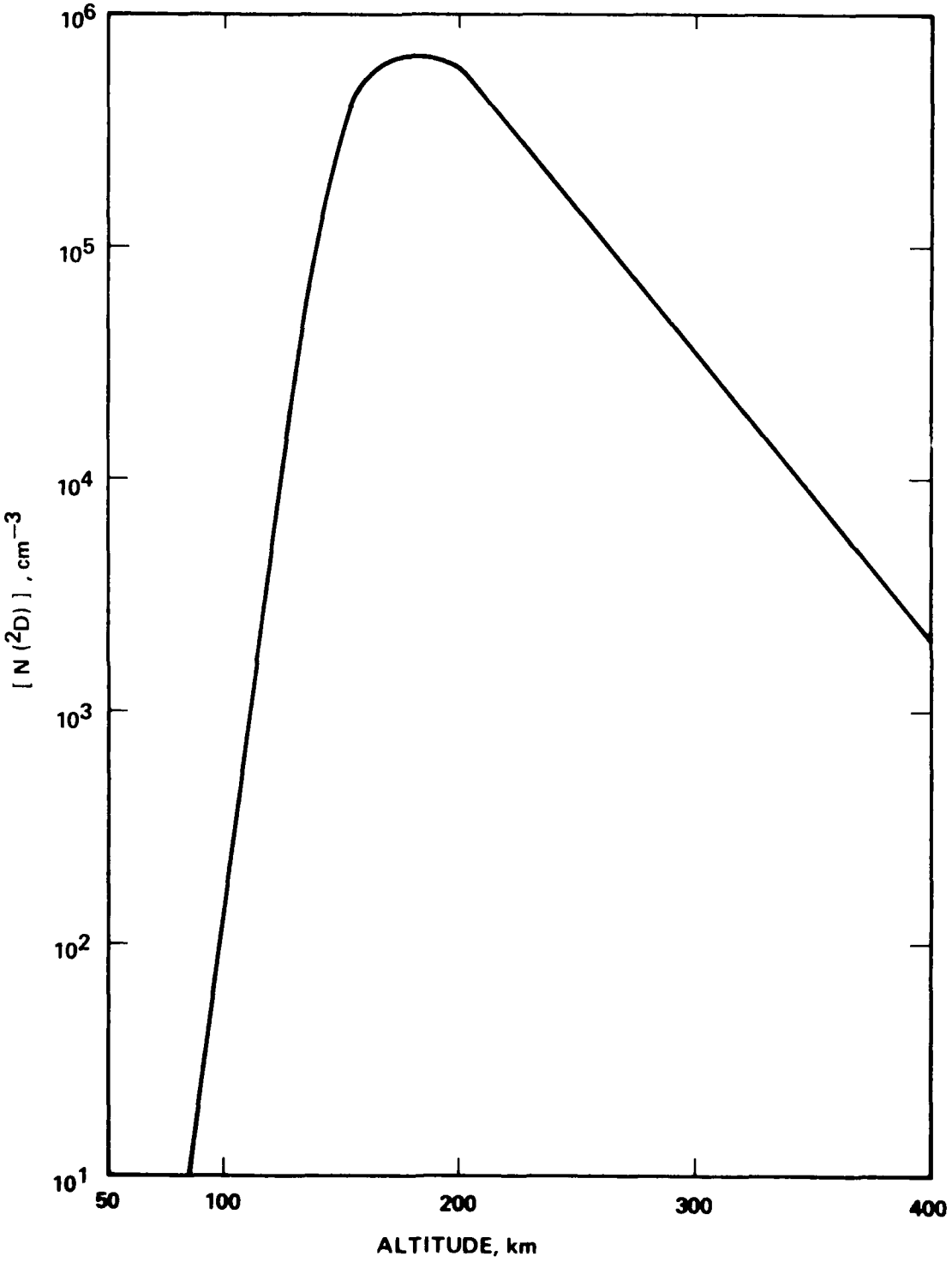

Figure 13-1. Basic component of N(^{2}D) profile (for t=9.4 hr, L=50°, f=0.25 yr, F $\lesssim$ 50×10^{-22} W m^{-2} Hz^{-1}).

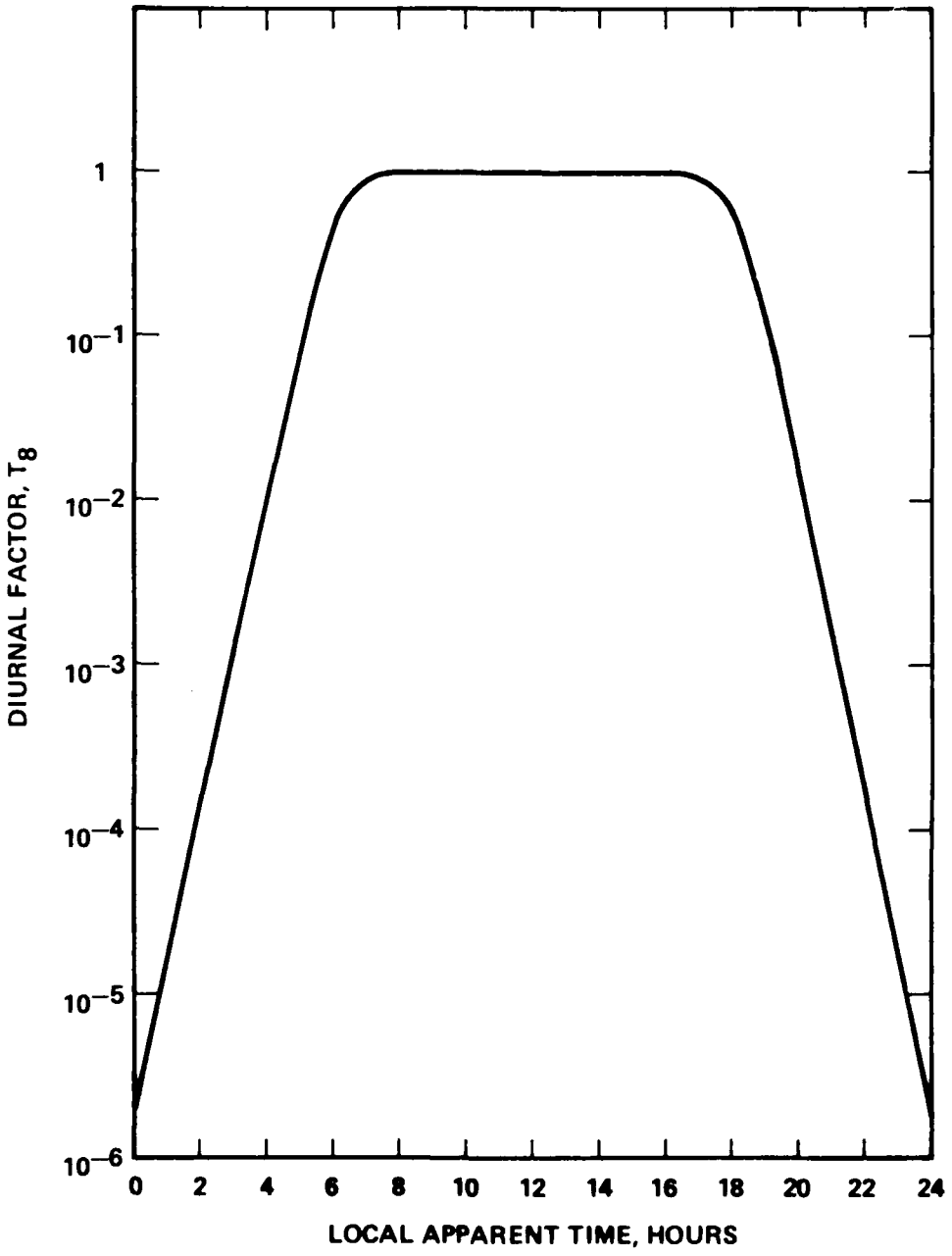

Figure 13-2. Diurnal variation factor for $N(^2D)$ atoms.

SECTION 14

REFERENCES

An-71d J.G. Anderson, "Rocket Measurements of OH in the Mesosphere," J. Geophys. Res. 76, 7820 (1971).

An-76 J.G. Anderson, "The Absolute Concentration of OH ($X^2\pi$) in the Earth's Stratosphere," Geophys. Res. Letters 3, 165 (1976).

BN-77 K.D. Baker, A.F. Nagy, R.O. Olsen, E.S. Oran, J. Randhawa, D.F. Strobel, and T. Tohmatsu, "Measurement of the Nitric Oxide Altitude Distribution in the Midlatitude Mesosphere," J. Geophys. Res. 82, 3281 (1977).

BT-73a M.R. Bowman and L. Thomas, "Sunrise Changes in Concentrations of Minor Neutral Constituents in the Mesosphere," J. Atmos. Terr. Phys. 35, 347 (1973).

Bu-76 C.R. Burnett, "Terrestrial OH Abundance Measurement by Spectroscopic Observation of Resonance Absorption of Sunlight," Geophys. Res. Letters 3, 319 (1976).

Ca-74 R.D. Cadle, Convener, "Report of Task Group V, U.S. Committee on Extension to the Standard Atmosphere Trace Constituents," May 1974 (draft copy).

CH-66a J.H. Carver, B.H. Horton, and F.G. Burger, "Natural Ozone Distribution in the Upper Atmosphere," J. Geophys. Res. 71, 4189 (1966).

CH-72 J.H. Carver, B.H. Horton, R.S. O'Brien, and B. Rofe, "Ozone Determinations by Lunar Rocket Photometry," Planet. Space Sci. 20, 217 (1972).

CI-65 CIRA 1965, COSPAR International Reference Atmosphere 1965, North-Holland Publishing Co., Amsterdam, (1965).

Cr-74a P. Crutzen, "A Review of Upper Atmospheric Photochemistry," Can. J. Chem. 52, 1569 (1974).

CS-76 T.E. Cravens and A.I. Stewart, "The Global Morphology of Nitric Oxide at 105 km," Trans. Amer. Geophys. Union 57, 295 (1976).

DA-77 T.M. Donahue, J.G. Anderson, W.T. Rawlins, F. Kaufman, and R.D. Hudson, "Apollo-Soyuz O(^{3}P) and N(^{4}S) Density Measurement by UV Spectroscopy," Geophys. Res. Letters 4, 79 (1977).

DH-76 D.D. Davis, W. Heaps, and T. McGee, "Direct Measurements of Natural Tropospheric Levels of OH Via an Aircraft-Borne Tunable Dye Laser," Geophys. Res. Letters 3, 331 (1976).

DT-73 Proceedings of the Second Conference on the Climatic Impact Assessment Program, 14-17 November 1972, Rep. No. DOT-TSC-OST-73-4, April 1973; U.S. Department of Commerce, National Technical Information Service, Rep. No. PB-221 166.

DT-74 Proceedings of the Third Conference on the Climatic Impact Assessment Program, 26 February - 1 March 1974, Rep. No. DOT-TSC-OST-74-15, November 1974; U.S. Department of Commerce, National Technical Information Service, Rep. No. AD/A-003 846.

DT-75 The Natural Stratosphere of 1974, CIAP Monograph 1, Rep. No. DOT-TST-75-51, September 1975; U.S. Department of Commerce, National Technical Information Service, Report No. PB-246 318.

Du-70a H.U. Dütsch, "Atmospheric Ozone - A Brief Review," J. Geophys. Res. 75, 1707 (1970).

Du-71 H.U. Dütsch, "Photochemistry of Atmospheric Ozone," pp. 219-322 in Advances of Geophysics, 15, edited by H.E. Landsberg and J. Van Mieghem, Academic Press (1971).

Du-74 H.U. Dütsch, "The Ozone Distribution in the Atmosphere," Can. J. Chem. 52, 1491 (1974).

EH-74 D.H. Ehhalt, L.E. Heidt, R.H. Leub, and N. Roper, "Vertical Profiles of CH_4, H_2, CO, N_2O, and CO_2 in the Stratosphere," p. 153 in DT-74.

EH-75 D.H. Ehhalt, L.E. Heidt, R.H. Leub, and E.A. Martell, "Concentrations of CH_4, CO, CO_2, H_2, H_2O, and N_2O in the Upper Stratosphere," J. Atmos. Sci. 32, 163 (1975).

EL-73 W.F.J. Evans and E.J. Llewellyn, "Atomic Hydrogen Concentrations in the Mesosphere and the Hydroxyl Emissions," J. Geophys. Res. 78, 323 (1973).

EM-77 M.J. Engebretson, K. Mauersberger, D.C. Kayser, W.E. Potter, and A.O. Nier, "Empirical Model of Atomic Nitrogen in the Upper Thermosphere," J. Geophys. Res. 82, 461 (1977).

EM-77a M.J. Engebretson, K. Mauersberger, and W.E. Potter, "Extension of Atomic Nitrogen Measurements into the Lower Thermosphere," J. Geophys. Res. 82, 3291 (1977).

FR-74 C.B. Farmer, O.F. Raper, R.A. Toth, and R.A. Schindler, "Recent Results of Aircraft Infrared Observations of the Stratosphere," p. 234 in DT-74.

FT-74 P.D. Feldman and P.Z. Takacs, "Nitric Oxide Gamma and Delta Band Emission at Twilight," Geophys. Res. Letters 1, 169 (1974).

Ge-75 J.-C. Gerard, "Satellite Observations of the Nitric Oxide Nightglow," Geophys. Res. Letters 2, 179 (1975).

GH-68a S.N. Ghosh, B.B. Hinton, L.M. Jones, R.J. Leite, C.J. Mason, E.J. Schaefer, and M. Walters, "Atomic Nitrogen in the Upper Atmosphere Measured by Mass Spectrometers," J. Geophys. Res. 73, 4425 (1968).

Go-69c R.M. Goody, "Time Variations in Atmospheric N_2O in Eastern Massachusetts," Planet. Space Sci. 17, 1319 (1969).

GZ-72a J.D. George, S.P. Zimmerman, and T.J. Keneshea, "The Latitudinal Variation of Major and Minor Neutral Species in the Upper Atmosphere," Space Research XII, 696, Akademie-Verlag, Berlin (1972).

Ha-76e J.E. Harries, "The Distribution of Water Vapor in the Stratosphere," Rev. Geophys. Space Phys. 14, 565 (1976).

HB-74a J.E. Harries, J.R. Birch, J.W. Fleming, N.W.B. Stone, D.G. Moss, N.R.W. Swann, and G.F. Neill, "Studies of Stratospheric H_2O, O_3, HNO_3, N_2O, and NO_2 from Aircraft," p. 197 in DT-74.

Hi-71a E. Hilsenrath, "Ozone Measurements in the Mesosphere and Stratosphere During Two Significant Geophysical Events," J. Atmos. Sci. 28, 295 (1971).

HO-70 P.B. Hays and J.J. Olivero, "Carbon Dioxide and Monoxide Above the Troposphere," Planet. Space Sci. 18, 1729 (1970).

HS-74a D.M. Hunten and D.F. Strobel, "Production and Escape of Terrestrial Hydrogen," J. Atmos. Sci. 31, 305 (1974).

HS-75 D.A. Hamlin and M.R. Schoonover, "The ROSCOE Manual Volume 14a - Ambient Atmosphere (Major and Minor Neutral Species and Ionosphere)," DNA 3964F-14a [SAI-75-609-LJ-2A], 13 June 1975.

HS-78 D.A. Hamlin and M.R. Schoonover, "The ROSCOE Manual Volume 14a-1 - Ambient Atmosphere (Major and Minor Neutral Species and Ionosphere)," DNA 3964F-14a-1 [SAI-78-604-LJ-2A], 12 July 1979.

Hu-73a B.G. Hunt, "A Generalized Aeronomic Model of the Mesosphere and Lower Thermosphere Including Ionospheric Processes," J. Atmos. Terr. Phys. 35, 1755 (1973).

Jo-75c D. Johnson, Aerospace Environment Division, Space Science Laboratory, NASA Marshall Space Flight Center, Huntsville, Alabama, privately communicated atmosphere data tape 4DREGB to D. Stevenson of SAI/Palo Alto on 21 January 1975. For original development of Four-D model including moisture data, see SG-71 and SF-72b. For subsequent description of Four-D model without moisture, see JW-74a.

JW-74a C.G. Justus, A.W. Woodrum, R.G. Roper, and O.E. Smith, "Four-D Global Reference Atmosphere, Technical Description Part I," NASA TM X-64871; "Users Manual and Programmers Manual, Part II," NASA TM X-64872, September 1974.

KL-77a P.W. Krey, R.J. Lagomarsino, and M. Schonberg, "Stratospheric Concentrations of N_2O in July 1975," Geophys. Res. Letters 4, 271 (1977).

KM-76a A.J. Krueger and R.A. Minzner, "A Midlatitude Ozone Model for the 1976 U.S. Standard Atmosphere," J. Geophys. Res. 81, 4477 (1976).

Kr-70a V.A. Krasnopoly'skiy, "Nitrogen Oxide at Heights of 100-220 km, According to Cosmos-224 Data," Geomag. & Aeron. 10, 660 (1970).

LD-74 S.C. Liu and T.M. Donahue, "The Aeronomy of Hydrogen in the Atmosphere of the Earth," J. Atmos. Sci. 31, 1118 (1974).

LD-74a S.C. Liu and T.M. Donahue, "Mesospheric Hydrogen Related to Exospheric Escape Mechanisms," J. Atmos. Sci. 31, 1466 (1974).

LD-74b S.C. Liu and T.M. Donahue, "Realistic Model of Hydrogen Constituents in the Lower Atmosphere and Escape Flux from the Upper Atmosphere," J. Atmos. Sci. 31, 2238 (1974).

LM-76 A.C. Levasseur, R.R. Meir, and B.A. Tinsley, "Resolution of the Discrepancy Between Balmer α Emission Rates, the Solar Lyman β Flux, and Models of Geocoronal Hydrogen Concentration," J. Geophys. Res. 81, 5587 (1976).

Ma-71c H.J. Mastenbrook, "The Variability of Water Vapor in the Stratosphere," J. Atmos. Sci. 28, 1495 (1971).

Me-69a R.R. Meier, "Balmer Alpha and Lyman Beta in the Hydrogen Geocorona," J. Geophys. Res. 74, 3561 (1969).

Me-70a R.R. Meier, "Observations of Lyman-α and the Atomic Hydrogen Distribution in the Thermosphere and Exosphere," Space Research X, 572 (1970).

Me-71 L.G. Meira, Jr., "Rocket Measurements of Upper Atmospheric Nitric Oxide and Their Consequences to the Lower Ionosphere," J. Geophys. Res. 76, 202 (1971).

ME-75 K. Mauersberger, M.J. Engebretson, W.E. Potter, D.C. Kayser, and A.O. Nier, "Atomic Nitrogen Measurements in the Upper Atmosphere," Geophys. Res. Letters 2, 337 (1975).

ME-76 M.B. McElroy, J.W. Elkins, S.C. Wofsy, and Y.L. Yung, "Sources and Sinks for Atmospheric N_2O," Rev. Geophys. Space Phys. 14, 143 (1976).

ME-76a K. Mauersberger, M.J. Engebretson, D.C. Kayser, and W.E. Potter, "Diurnal Variation of Atomic Nitrogen," J. Geophys. Res. 81, 2413 (1976).

ME-76b K. Mauersberger, M.J. Engebretson, and A.O. Nier, "Seasonal Variation of Atomic Nitrogen," AGU Trans. 57, 295 (1976).

MG-73b D.G. Murcray, A. Goldman, F.H. Murcray, W.J. Williams, J.N. Brooks, and D.B. Barker, "Vertical Distribution of Minor Atmospheric Constituents as Derived from Airborne Measurements of Atmospheric Emission and Absorption Infrared Spectra," p. 86 in DT-73.

MM-70c R.R. Meier and P. Mange, "Geocoronal Hydrogen: An Analysis of the Lyman-Alpha Airglow Observed from OGO-4," Planet. Space Sci. 18, 803 (1970).

MM-73 R.R. Meier and P. Mange, "Spatial and Temporal Variations of the Lyman-Alpha Airglow and Related Atomic Hydrogen Distributions," Planet. Space Sci. 21, 309 (1973).

MW-70b R.R. Meier, D.M. Weiss, and P. Mange, "High-Altitude Measurement of the Lyman-Alpha Nightglow at Solar Minimum," J. Geophys. Res. 75, 4224 (1970).

My-75 B.F. Myers, "The ROSCOE Manual Volume 14b - Midlatitude Density Profiles of Selected Atmospheric Species," DNA 3964F-14b [SAI-75-609-LJ-2B], 13 June 1975.

Ne-77 R.E. Newell, "One-Dimensional Models: A Critical Comment, and Their Application to Carbon Monoxide," J. Geophys. Res. 82, 1449 (1977).

Ni-74 M. Nicolet, "An Overview of Aeronomic Processes in the Stratosphere and Mesosphere," Can. J. Chem. 52, 1381 (1974).

OJ-75 E.S. Oran, P.S. Julienne, and D.F. Strobel, "The Aeronomy of Odd Nitrogen in the Thermosphere," J. Geophys. Res. 80, 3068 (1975).

OK-77 T. Ogawa and Y. Kindo, "Diurnal Variability of Thermospheric N and NO," Planet. Space Sci. 25, 735 (1977).

OP-72 D. Offermann, K. Pelka, and U. Von Zahn, "Mass Spectrometric Measurements of Minor Constituents in the Lower Thermosphere," Int. J. Mass Spectrom. Ion Phys. 8, 391 (1972).

PD-74 C. Prabhakara, G. Dalu, and V.G. Kunde, "A Search for Global and Seasonal Variation of Methane from Nimbus 4 Iris Measurements," J. Geophys. Res. 79, 1744 (1974).

PE-76 D. Perner, D.H. Ehhalt, H.W. Pätz, U. Platt, E.P. Röth, and A. Volz, "OH-Radicals in the Lower Troposphere," Geophys. Res. Letters 3, 466 (1976).

RC-75b M.A. Ruderman and J.W. Chamberlain, "Origin of the Sunspot Modulation of Ozone: Its Implications for Stratospheric NO Injection," Planet. Space Sci. 23, 247 (1975).

Re-68c E.I. Reed, "A Night Measurement of Mesospheric Ozone by Observations of Ultraviolet Airglow," J. Geophys. Res. 73, 2951 (1968).

RF-76 M.A. Ruderman, H.M. Foley, and J.W. Chamberlain, "Eleven-Year Variation in Polar Ozone and Stratospheric-Ion Chemistry," Science 192, 555 (1976).

RK-76 R.A. Rasmussen, J. Krasnec, and D. Pierotti, "N_2O Analysis in the Atmosphere via Electron Capture - Gas Chromatography," Geophys. Res. Letters 3, 615 (1976).

RL-77 H.E. Radford, M.M. Litvak, C.A. Gottlieb, E.W. Gottlieb, S.K. Rosenthal, and A.E. Lilley, "Mesospheric Water Vapor Measured from Ground-Based Microwave Observations," J. Geophys. Res. 82, 472 (1977).

RS-75b D.W. Rusch, A.I. Stewart, P.B. Hays, and J.H. Hoffman, "The NI (5200 Å) Dayglow," J. Geophys. Res. 80, 2300 (1975).

RS-76d D.W. Rusch, A.I. Stewart, P.B. Hays, and J.H. Hoffman, "The NI (5200 Å) Dayglow," Correction, J. Geophys. Res. 81, 295 (1976).

RS-77 J.W. Rogers, A.T. Stair, Jr., T.C. Degges, C.L. Wyatt, and D.J. Baker, "Rocketborne Measurement of Mesospheric H_2O in the Auroral Zone," Geophys. Res. Letters 4, 366 (1977).

SA-77 A.L. Schmeltekopf, D.L. Albritton, et al., "Stratospheric Nitrous Oxide Altitude Profiles at Various Latitudes," J. Atmos. Sci. 34, 729 (1977).

SF-72b D.B. Spiegler and M.G. Fowler, "Four-Dimensional World-Wide Atmospheric Models (Surface to 25-km Altitude)," NASA CR-2082 (Allied Research Associates, Inc. 9G-88F), July 1972.

SG-71 D.B. Spiegler and J.R. Greaves, "Development of Four-Dimensional Atmospheric Models (World-Wide)," NASA CR61362 (Allied Research Associates, Inc.), August 1971.

Si-77 H.B. Singh, "Atmospheric Halocarbons: Evidence in Favor of Reduced Average Hydroxyl Radical Concentration in the Troposphere," Geophys. Res. Letters 4, 101 (1977).

SJ-70 W. Seiler and C. Junge, "Carbon Monoxide in the Atmosphere," J. Geophys. Res. 75, 2217 (1970).

SJ-70a K. Schutz, C. Junge, R. Beck, and B. Albrecht, "Studies of Atmospheric N_2O," J. Geophys. Res. 75, 2230 (1970).

SL-70a T. Shimazaki and A.R. Laird, "A Model Calculation of the Diurnal Variation in Minor Neutral Constituents in the Mesosphere and Lower Thermosphere Including Transport Effects," J. Geophys. Res. 75, 3221 (1970).

SL-72 T. Shimazaki and A.R. Laird, "Correction to 'A Model Calculation Variation in Minor Neutral Constituents in the Mesosphere and Lower Thermosphere Including Transport Effects," J. Geophys. Res. 77, 276 (1972).

SO-76 D.F. Strobel, E.S. Oran, and P.D. Feldman, "The Aeronomy of Odd Nitrogen in the Thermosphere.2. Twilight Emissions," J. Geophys. Res. 81, 3745 (1976).

SW-76 T. Shimazaki and R.C. Whitten, "A Comparison of One-Dimensional Theoretical Models of Stratospheric Minor Constituents," Rev. Geophys. Space Phys. 14, 1 (1976).

TB-72 L. Thomas and M.R. Bowman, "The Diurnal Variations of Hydrogen and Oxygen Constituents in the Mesosphere and Lower Thermosphere," J. Atmos. Terr. Phys. 34, 1843 (1972).

TB-76 H. Trinks, C.A. Barth, K. Kelly, and U. von Zahn, "A Joint Nitric Oxide Measurement by Rocket-Borne Ultraviolet Photometer and Mass Spectrometer in the Lower Thermosphere," Trans. Am. Geophys. Union 57, 295 (1976).

TB-76a M.R. Torr, R.G. Burnside, P.B. Hays, A.I. Stewart, D.G. Torr, and J.C.G. Walker, "Metastable ^2D Atomic Nitrogen in the Mid-Latitude Nocturnal Ionosphere," J. Geophys. Res. 18, 531 (1976).

Ti-73 G.C. Tisone, "Measurements of NO Densities during Sunrise at Kauai," J. Geophys. Res. 78, 746 (1973).

TI-75 T. Tohmatsu and N. Iwagami, "Measurement of Nitric Oxide Distribution in the Upper Atmosphere," Space Res. XV, 241 (1975).

TT-75 M.R. Torr, D.G. Torr, J.C.G. Walker, P.B. Hays, W.B. Hansen, J.H. Hoffman, and D.C. Kayser, "Effects of Atomic Nitrogen on the Nocturnal Ionosphere," Geophys. Res. Letters. 2, 385 (1975).

TT-76a D.G. Torr, M.R. Torr, D.W. Rusch, P.B. Hays, K. Mauersberger, J.C.G. Walker, N.W. Spencer, A.E. Hedin, H.C. Brinton, and R.F. Theis, "Atomic Nitrogen Densities in the Thermosphere," Geophys. Res. Letters 3, 1 (1976).

US-66 U.S. Standard Atmosphere Supplements, 1966, Available from the U.S. Government Printing Office, Washington, D.C. 20402.

US-76 U.S. Standard Atmosphere, 1976, Available from the U.S. Government Printing Office, Washington, D.C. 20402.

VB-73 A. Vidal-Madjar, J.E. Blamont, and B. Phissamay, "Solar Lyman Alpha Changes and Related Hydrogen Density Distribution at the Earth's Exobase (1969-1970)," J. Geophys. Res. 78, 1115 (1973).

Vu-75 R.K.R. Vupputuri, "Seasonal and Latitudinal Variations of N_2O and NO_x in the Stratosphere," J. Geophys. Res. 80, 1125 (1975).

WA-74 P. Warneck, "On the Role of OH and HO_2 Radicals in the Troposphere," Tellus XXVI, 39 (1974).

WD-75 C. Wang, L.I. Davis, Jr., C.H. Wu, S. Japer, H. Niki, and B. Weinstock, "Hydroxyl Radical Concentrations Measured in Ambient Air," Science 189, 797 (1975).

WM-72 S.C. Wofsy, J.C. McConnell, and M.B. McElroy, "Atmospheric CH_4, CO, and CO_2," J. Geophys. Res. 77, 4477 (1972).

WT-74 R.C. Whitten and R.P. Turco, "Diurnal Variations of HO_x and NO_x in the Stratosphere," J. Geophys. Res. 79, 1302 (1974).

WW-76 J.W. Waters, W.J. Wilson, F.I. Shimabukuro, "Microwave Measurement of Mesospheric Carbon Monoxide," Science 191, 1174 (1976).

DISTRIBUTION LIST

DEPARTMENT OF DEFENSE

Assistant to the Secretary of Defense
Atomic Energy
ATTN: Executive Assistant

Defense Advanced Rsch. Proj. Agency
ATTN: TIO
ATTN: STO, S. Zakanycz

Defense Communications Engineer Center
ATTN: Code R410, J. McLean

Defense Nuclear Agency
ATTN: DDST
ATTN: RAAE
4 cy ATTN: TITL

Defense Technical Information Center
12 cy ATTN: DD

Field Command
Defense Nuclear Agency
ATTN: FCPR

Field Command
Defense Nuclear Agency
Livermore Division
ATTN: FCPRL

Interservice Nuclear Weapons School
ATTN: TTV

National Security Agency
ATTN: R-52, J. Skillman

Undersecretary of Defense for Rsch. & Engrg.
ATTN: Strategic & Space Systems (OS)

WWMCCS System Engineering Org.
ATTN: R. Crawford

DEPARTMENT OF THE ARMY

Atmospheric Sciences Laboratory
U.S. Army Electronics R&D Command
ATTN: DELAS-EO, F. Niles

BMD Advanced Technology Center
Department of the Army
ATTN: ATC-T, M. Capps
ATTN: ATC-O, W. Davies

BMD Systems Command
Department of the Army
ATTN: BMDSC-HW, R. DeKalb

Harry Diamond Laboratories
Department of the Army
ATTN: DELHD-N-P, F. Wimenitz
ATTN: DELHD-I-TL

U.S. Army Foreign Science & Tech. Ctr.
ATTN: DRXST-SD

U.S. Army Missile Command
ATTN: DRDMI-XS
ATTN: RSIC

DEPARTMENT OF THE ARMY (Continued)

U.S. Army Missile Intelligence Agency
ATTN: J. Gamble

U.S. Army Nuclear & Chemical Agency
ATTN: Library

U.S. Army Satellite Comm. Agency
ATTN: Document Control

U.S. Army TRADOC Systems Analysis Activity
ATTN: ATAA-PL

DEPARTMENT OF THE NAVY

Naval Electronic Systems Command
ATTN: Code 501A
ATTN: PME 117-20

Naval Intelligence Support Ctr.
ATTN: Document Control

Naval Ocean Systems Center
ATTN: Code 532

Naval Postgraduate School
ATTN: Code 1424

Naval Research Laboratory
ATTN: Code 6701, J. Brown
ATTN: Code 2627
ATTN: Code 6780, P. Palmadesso
ATTN: Code 6700, T. Coffey
ATTN: Code 6709, W. Ali
ATTN: Code 6780, S. Ossakow

Naval Surface Weapons Center
ATTN: Code X211
ATTN: Code F31

Naval Surface Weapons Center
ATTN: Code F-14, R. Butler

Strategic Systems Project Office
Department of the Navy
ATTN: NSP-2722, F. Wimberly
ATTN: NSSP-2722, M. Meserole

DEPARTMENT OF THE AIR FORCE

Air Force Geophysics Laboratory
ATTN: SULL
ATTN: LKB, K. Champion
ATTN: OPR, A. Stair
ATTN: OPR, H. Gardiner

Air Force Systems Command
ATTN: Technical Library

Air Force Technical Applications Center
ATTN: Technical Library
ATTN: TFR, C. Meneely

Air Force Weapons Laboratory
Air Force Systems Command
ATTN: SUL
ATTN: DYC

DEPARTMENT OF THE AIR FORCE (Continued)

Ballistic Missile Office
Air Force Systems Command
ATTN: MNX

Deputy Chief of Staff
Research, Development, & Acq.
Department of the Air Force
ATTN: AFRDQ

Headquarters Space Division
Air Force Systems Command
ATTN: DYS Space Defense Systems

Headquarters Space Division
Air Force Systems Command
ATTN: RSP

Headquarters Space Division
Air Force Systems Command
ATTN: SKA, M. Clavin
ATTN: SKX

Headquarters Space Division
Air Force Systems Command
ATTN: SZJ, P. Kelley

Rome Air Development Center
Air Force Systems Command
ATTN: TSLD
ATTN: OCSA, J. Simons
ATTN: OCS, V. Coyne

Strategic Air Command
Department of the Air Force
ATTN: XPFS, B. Stephan
ATTN: NRT

DEPARTMENT OF ENERGY

Department of Energy
ATTN: Document Control for OMA

OTHER GOVERNMENT AGENCIES

Department of Commerce
National Oceanic & Atmospheric Admin.
ATTN: F. Fehsenfeld

Institute for Telecommunications Sciences
National Telecommunications & Info. Admin.
ATTN: W. Utlaut
ATTN: G. Falcon

DEPARTMENT OF DEFENSE CONTRACTORS

Aerojet Electro-Systems Co.
ATTN: J. Graham

Aerospace Corp.
ATTN: V. Josephson
ATTN: J. Reinheimer
ATTN: N. Stockwell
ATTN: I. Garfunkel
ATTN: R. Rawcliffe
ATTN: N. Cohen

Berkeley Research Associates, Inc.
ATTN: J. Workman

DEPARTMENT OF DEFENSE CONTRACTORS (Continued)

ESL, Inc.
ATTN: J. Marshall

General Electric Co.
ATTN: T. Baurer
ATTN: M. Bortner

General Electric Company—TEMPO
ATTN: T. Stevens
ATTN: W. Knapp
ATTN: J. Jordano
ATTN: DASIAC
ATTN: M. Stanton

General Research Corp.
ATTN: J. Garbarino
ATTN: J. Ise, Jr.

Jamieson Science & Engineering
ATTN: J. Jamieson

Kaman Sciences Corp.
ATTN: P. Tracy
ATTN: D. Perio
ATTN: N. Beauchamp

Lockheed Missiles & Space Co., Inc.
ATTN: M. Walt

M.I.T. Lincoln Lab.
ATTN: D. Towle

McDonnell Douglas Corp.
ATTN: R. Halprin

Mission Research Corp.
ATTN: F. Fajen
ATTN: D. Sappenfield
ATTN: M. Scheibe
ATTN: D. Archer
ATTN: R. Kilb
ATTN: R. Hendrick
ATTN: R. Bogusch

Photometrics, Inc.
ATTN: I. Kofsky

University of Pittsburgh
ATTN: F. Kaufman

R & D Associates
ATTN: R. Lelevier
ATTN: R. Turco
ATTN: F. Gilmore
ATTN: C. MacDonald
ATTN: B. Gabbard

R & D Associates
ATTN: H. Mitchell

Rand Corp.
ATTN: C. Crain

Science Applications, Inc.
ATTN: D. Hamlin
ATTN: B. Myers

Science Applications, Inc.
ATTN: W. Mendes

DEPARTMENT OF DEFENSE CONTRACTORS (Continued)

SRI International
ATTN: W. Chesnut
ATTN: W. Jaye

Visidyne, Inc.
ATTN: C. Humphrey
ATTN: J. Carpenter

DEPARTMENT OF DEFENSE CONTRACTORS (Continued)

Teledyne Brown Engineering
ATTN: J. Cato
ATTN: J. Beaupre
ATTN: G. Harney